

2017-01-01

Characterization and Comparison of Metallic and Ceramic Parts Fabricated Using Powder Bed-Based Additive Manufacturing Technologies

Jose Angel Gonzalez

University of Texas at El Paso, jagonzalez24@miners.utep.edu

Follow this and additional works at: https://digitalcommons.utep.edu/open_etd



Part of the [Engineering Commons](#)

Recommended Citation

Gonzalez, Jose Angel, "Characterization and Comparison of Metallic and Ceramic Parts Fabricated Using Powder Bed-Based Additive Manufacturing Technologies" (2017). *Open Access Theses & Dissertations*. 460.

https://digitalcommons.utep.edu/open_etd/460

This is brought to you for free and open access by DigitalCommons@UTEP. It has been accepted for inclusion in Open Access Theses & Dissertations by an authorized administrator of DigitalCommons@UTEP. For more information, please contact lweber@utep.edu.

CHARACTERIZATION AND COMPARISON OF METALLIC AND CERAMIC
PARTS FABRICATED USING POWDER BED-BASED ADDITIVE
MANUFACTURING TECHNOLOGIES

JOSE ANGEL GONZALEZ, B.S.M.M.E.

Doctoral Program in Materials Science and Engineering

APPROVED:

Ryan B. Wicker, Ph.D., Chair

Yirong Lin, Ph.D.

Stephen W. Stafford, Ph.D.

Jorge A. Lopez, Ph.D.

Charles Ambler, Ph.D.
Dean of the Graduate School

Copyright ©

by

Jose A. Gonzalez

2017

This Dissertation is dedicated to my loving parents, Jose A. and L. Yolanda Gonzalez. I am internally grateful for your endless support.

CHARACTERIZATION AND COMPARISON OF METALLIC AND CERAMIC
PARTS FABRICATED USING POWDER BED-BASED ADDITIVE
MANUFACTURING TECHNOLOGIES

by

Jose Angel Gonzalez, B.S. M.M.E.

Dissertation

Presented to the Faculty of the Graduate School of
The University of Texas at El Paso
in Partial Fulfillment
of the Requirements
for the Degree of

DOCTOR OF PHILOSOPHY

Department of Metallurgical, Materials and Biomedical Engineering

THE UNIVERSITY OF TEXAS AT EL PASO

August 2017

Acknowledgements

First, I would like to thank Dr. Ryan B. Wicker, director of the W.M. Keck Center for 3D Innovation (Keck Center), for presenting me with the opportunity to perform this research under his guidance. Dr. Wicker has been my mentor for over 3 years and has taught me the importance of self-direction in the pursuit of once ultimate goal. Dr. Wicker has provided me with wisdom that cannot be taught in any other form. I would like to thank Dr. Yirong Lin, for also mentoring me and helping with day-to-day operations throughout. A special gratitude to Jorge Mireles, who pushed me to be self-reliant and expressed an incomparable work-ethic, making him a one of my role models. Dr. Cesar Terrazas, another important person involved in my success, who provided advice in writing and research that was un-parallel to others, I am extremely thankful.

The research was supported, in part, by the U.S. Department of Energy (DOE) through award # DE-FE0012321. A special thank you to the Department of Energy for their advice, providing multiple forms of support throughout the time period of this research.

Several other researchers deserve recognition for their countless contributions. I would like to thank my co-workers (The Metals Team) at the Keck Center: Dr. Sara Gaytan, Mohammad S. Hossain, Diego Mejorado, Israel Segura, Jasmine Roldan, Victor Elicerio, Zia Uddin, Diego Bermudez, David Saenz, and Ricardo Martinez who have assisted in this journey of higher education

I would like to express my deepest gratitude to my parents, Jose and Yolanda, for their continuous support and compassion when I needed them the most. My accomplishments were possible thanks to them. I want to thank my two sisters, Nallely and Yazmin, to whom have created a blueprint for success that will guide me for the rest of my life, for which I consider them my real-life mentors. Also to my friends for their moral support and encouragement.

This journey would have seemed much more difficult without this people in my life.

Abstract

Additive manufacturing (AM), or layer-by-layer part fabrication, is enabling the materialization of ideas that were near to impossible to achieve in the past, while providing advantages that include reduced material footprint, increased complexity, reduced lead times, etc. AM has been integrated to highly specialized markets that include aerospace, military, automotive, biomedical, and prototyping.

Although an apparent growth is being witnessed across nearly all AM platforms, technologies with capabilities of producing metallic parts have arguably received the most widespread interest, with powder bed fusion (i.e. electron beam melting and selective laser melting). This class of AM technology produces parts by judiciously melting precursor powder, represents 90% of the metal market [1]. Binder jetting, although not categorized under powder bed fusion, is also a powder bed-based technique that can be used for direct metal fabrication, and that is seeing an increased adoption in low-cost applications, such as metal prototypes. As these technologies continue to evolve, more industries are implementing to production.

A limited amount of comparative studies exists between powder bed-based AM technologies for the fabrication of metallic components that include initial fabrication steps and continue to final end-user production. This research includes an extensive characterization and comparison between commonly used powder bed-based AM technologies including (1) electron beam melting (EBM), (2) selective laser melting (SLM), and (3) binder jetting. The aim of this research is to have a thorough examination of the AM techniques by evaluating advantages and constraints faced by each technology by the fabrication of metallic components. The study contains an evaluation on system cost, fabrication time for parts, energy consumption during fabrication, mechanical properties, as well as fractography. By creating a comparative study that provides insight into the fabrication process and characterizes each technology's product, possible applications and capabilities of each technology for meeting the demands of the application is

gained. This study can be used to determine distinct characteristics between the three listed technologies and followed for other technologies and materials using similar approaches.

First, an analysis considering the fabrication time and energy consumption of producing parts for all three platforms was conducted. Results determined that SLM technology required the least amount of fabrication time and energy for the fabrication of single part fabrication. However, for production of multiple parts, or large volume builds, binder jetting technology becomes an efficient form of fabrication method.

Subsequently, the study continued with characterization of Inconel 625 fabricated by the three powder bed-based technologies in the X and Z build orientations. Metallography revealed directional microstructure dependence for EBM fabricated specimens that remained after a hot-isostatic pressing (HIPing) process. However, the melt pools found in the microstructure of SLM fabricated specimens were removed once HIPed, leaving a more homogenous microstructure. Observations made for binder jetting microstructure were larger grains in comparison to EBM and SLM. SLM outperformed both technologies in the mechanical properties tested (i.e. ultimate tensile stress, % elongation, yield stress, and modulus of elasticity) with nearly all technologies able to surpass the minimum requirements based by ASTM-F3056-15 a standard for AM fabrication parts similar to wrought Inconel 625. Both EBM and binder jetting were unsuccessful in achieving the minimum standard in % elongation (at break). All specimens demonstrated a ductile fracture mode, exposed in the form of dimple formation on fracture surfaces, after performance of failure analysis.

The final aspect of this research investigated the fabrication of “smart parts” employing an interrupted process that allowed embedding sensors in AM produced parts during the build process. It was demonstrated that the layer-by-layer part fabrication of AM, enables the opportunity of fabricating “smart” complex components by allowing the insertion of a piezoceramic sensor during a multi-step “stop-and-go” process that can only be achieved by an additive manufacturing method.

Table of Contents

Acknowledgements.....	v
Abstract.....	vi
Table of Contents.....	viii
List of Tables	xii
List of Figures.....	xiv
Chapter 1: Introduction.....	1
1.1 Research Motivation.....	1
1.2 Project Overview	2
Chapter 2: Objectives.....	4
Chapter 3: Literature Review.....	6
3.1 Additive Manufacturing.....	6
3.1.1 AM Technologies for Metallic Applications	8
3.2 Electron Beam Melting (EBM).....	10
3.3 Selective Laser Melting (SLM)	12
3.4 Binder Jetting.....	15
3.5 INCONEL Alloys	17
3.5.1 INCONEL 718.....	17
3.5.2 INCONEL 625	18
3.6 Powder Bed-Based Systems Comparisons	18
3.7 Advance Application Demonstration of Future AM Fabricated Components	21

Chapter 4: Fabrication and Energy Consumption Model Comparison between Powder Bed-Based AM Technologies.....	24
4.1 Capital Cost.....	26
4.2 Single Part Case Studies	27
4.3 Multi-Part Case Studies	29
4.4 Chapter Conclusion.....	32
Chapter 5: Characterization of Inconel Alloy 625 Fabrication using Powder Bed-based AM Technologies	33
5.1 Powder Analysis	35
5.2 Built Components Density Measurements	38
5.3 Microstructure.....	40
5.3.1 As-Fabricated Microstructure	40
5.3.2 HIPed Microstructure	43
5.4 Mechanical Properties.....	45
5.4.1 Ultimate Tensile Strength	49
5.4.2 % Elongation (at Break).....	51
5.4.3 Yield Stress	53
5.4.4 Modulus of Elasticity	55
5.4.5 Hardness Results.....	57
5.5 Chapter Conclusion.....	59
Chapter 6: Fractography of Inconel 625 Fabricated Samples Fabricated by Powder Bed-Based Additive Manufacturing Technologies	60

6.1 Macro-Scale Evaluation.....	60
6.2 Fractography of As-Fabricated Specimens.....	61
6.3 Fractography of HIPed Specimens	65
6.4 Chemical Analysis	68
6.5 Chapter Conclusion.....	73
Chapter 7: Stop-and-Go Interruption Fabrication Process Using Powder Bed-Based	
AM Technologies for Smart Sensing applications	74
7.1 “Smart Part” Fabrication using Stop –and-Go Process	76
7.1.1 EBM Stop-and-Go Fabrication Method.....	76
7.1.2 SLM Stop-and-Go Fabrication Method	76
7.1.3 Binder Jetting Fabrication Method	79
7.2 Sensor Protection by Housing Design	79
7.2.1 Fabrication of Ceramic Sensor Housing Using Binder Jetting Technology	81
7.3 Interface bonding	85
7.3.1 Microstructure Evaluation of Stop-and Go Process.....	85
7.3.2 Chemical Composition Evaluation of Stop-and Go Process	89
7.3.3 Identified Defects on Interface.....	91
7.4 “Smart Part” Sensing Capabilities	93
7.5 Applications of “Smart Parts”	94
7.6 Chapter Conclusion.....	101
Chapter 8: Conclusions and Recommendations	
8.1 Conclusions.....	102

8.2 Recommendations.....	104
Appendix.....	114
Curriculum Vita	123

List of Tables

Table 1. Energy consumption for case study 1&2 based on the individual steps for each technology.....	29
Table 2. Energy consumption for case study 3&4 based on the individual steps for each technology.....	30
Table 3. Powder analysis of as-received powders for each technology, including average particle size, flow rate and apparent density	36
Table 4. Chemical Composition of as-received powder for each technology	38
Table 5. Average UTS values for as-fabricated and HIPed fabricated Inconel 625 by the powder bed-based technologies comparing both X and Z built orientation	50
Table 6. Average % Elongation (at break) values for as-fabricated and HIPed fabricated Inconel 625 by the powder bed-based technologies comparing both X and Z built orientation. Red values indicate failure to meet ASTM F3056-14 minimum requirements.	52
Table 7. Average YS values for as-fabricated and HIPed fabricated Inconel 625 by the powder bed-based technologies comparing both X and Z built orientation.	54
Table 8. Average <i>E</i> values for as-fabricated and HIPed fabricated Inconel 625 by the powder bed-based technologies comparing both X and Z built orientation.	56
Table 9. Rockwell hardness results for the three powder bed-based AM technologies using the B-scale.....	58
Table 10. Chemical composition of binder jetting fracture surface, oxygen content is highlighted since it has increased from the stock powder material.	71
Table 11. Characterization of alumina fabricated parts using binder jetting AM technology.....	84
Table 12. Chemical analysis of the three individual areas for the stop-and-go EBM fabricated sample	90

Table 13. Chemical analysis of the three individual areas for the stop-and-go SLM fabricated sample.....	91
---	----

List of Figures

Figure 1. Generic AM fabrication Process flow diagram	7
Figure 2. Powder bed fusion parts for (A) LEAP engine fuel nozzle (B) Hip implant (C) Truss structure implants. [11] [15] [3]	9
Figure 3. Schematic diagram of EBM machine and components.....	11
Figure 4. Flow diagram of the fabricating process for EBM with each individual step detailed.....	12
Figure 5. Flow diagram of the fabricating process for SLM with each individual step detailed.....	14
Figure 6. Schematic diagram of SLM machine and components	14
Figure 7. Schematic diagram of binder jetting machine [23]	16
Figure 8. Flow diagram of the fabricating process for binder jetting with each individual step detailed.....	16
Figure 9. Unit cost model versus capacity utilization [36]	20
Figure 10. Multi-material fabrication process using EBM [43]	23
Figure 11. Generic representation of the 4 case studies used for the cosst model simulation	25
Figure 12. Cost comparison of equipment required to achieve part fabrication using each powder bed-based system. A breakdown list indicates the cost of required equipment.	26
Figure 13. Fabrication time (hours) and energy comparison (kilowatt hour for single- part case study 1&2	28
Figure 14. Fabrication time (hours) and energy comparison (kilowatt hour for multi- part case study 3&4	31
Figure 15. Isometric view of build setup used for fabrication using the powder bed- based AM technologies.....	34

Figure 16. SEM Images of precursor powder used for the fabrication using (A) binder jetting, (B) EBM, and (C) SLM.....	37
Figure 17. Measurement kit used to obtain apparent densities of samples.....	39
Figure 18. Microstructure cubes of as-fabricated Inconel alloy 625 manufactured by (a) binder jetting, (B) EBM, and (C) SLM. Build direction indicated by arrow	42
Figure 19. Microstructure cubes of HIPed treated Inconel alloy 625 manufactured by (a) binder jetting, (B) EBM, and (C) SLM. Build direction indicated by arrow	44
Figure 20. High magnification of Inconel 625 fabricated by EBM technology showing directional pattern of precipitates	45
Figure 21. Process of tension specimens' preparation. Dimensions of design are in mm.	47
Figure 22. Tensile testing setup with specimen set to test.....	48
Figure 23. Average UTS for Inconel alloy 625 fabricated by powder bed-based AM technologies. (A) Results of as-fabricated samples and (B) HIPed samples. Dotted line indicates the minimum value required by ASTM standard F3056-14.	51
Figure 24. Average %Elongation (at break) for Inconel alloy 625 fabricated by powder bed-based AM technologies. (A) Results of as-fabricated samples and (B) HIPed samples. Dotted line indicates the minimum value required by ASTM standard F3056-14.....	53
Figure 25. Average YS for Inconel alloy 625 fabricated by powder bed-based AM technologies. (A) Results of as-fabricated samples and (B) HIPed samples. Dotted line indicates the minimum value required by ASTM standard F3056-14.	55
Figure 26. Average E for Inconel alloy 625 fabricated by powder bed-based AM technologies. (A) Results of as-fabricated samples and (B) HIPed samples.....	57

Figure 27. Macro-scale inspection of the three powder bed-based AM technologies fracture where double cup fractures are visible; (left) as-fabricated and (right) HIPed.	60
Figure 28. SEM images of fracture surfaces of failed binder jetting as-fabricated specimens. (A) Shows the fracture surface of EBM X orientation and (B) of Z orientation	62
Figure 29. SEM images of fracture surfaces of failed EBM as-fabricated specimens. (A) Shows the fracture surface of SLM X orientation and (B) of Z orientation	63
Figure 30. Example of a fracture surface of pre-mature as-fabricated EBM sample	64
Figure 31. SEM images of fracture surfaces of failed SLM as-fabricated specimens. (A) Shows the fracture surface of binder jetting X orientation and (B) of Z orientation	65
Figure 32. SEM images of fracture surfaces of failed binder jetting HIPed specimens. (A) Shows the fracture surface of binder jetting X orientation and (B) of Z orientation	66
Figure 33. SEM images of fracture surfaces of failed EBM HIPed specimens. (A) Shows the fracture surface of EBM X orientation and (B) of Z orientation	66
Figure 34. SEM images of fracture surfaces of failed SLM HIPed specimens. (A) Shows the fracture surface of SLM X orientation and (B) of Z orientation	67
Figure 35. High magnification SEM image of SLM fracture surface with an example of an inclusion (precipitate) within the micro-voids.	68
Figure 36. Layered elemental mapping image of fracture surface for binder jetting Z-orientation build combining all elements present.	69
Figure 37. Individual element maps of binder jetting fracture surface based on EDS, oxygen element (blue) is existent within the captured powder particles in high concentration.....	70

Figure 38. SEM image of binder jetting fracture surface accompanied by EDS analysis on individual particles found on micro-voids as well as the matrix metal.	72
Figure 39. (A) “Smart cylinder” and (B) “smart turbine engine” design where arrows indicate the placement of the embedded sensor.	75
Figure 40. EBM fabrication process integrating a stop-and-go method for the insertion of a sensor for pressure and temperature sensing reading capabilities [68].	77
Figure 41. SLM fabrication process integrating a stop-and-go method for the insertion of a sensor providing pressure and temperature reading capabilities.	78
Figure 42. Binder jetting fabrication process steps to produce “smart parts”, where a sensor is embedded providing pressure and temperature reading capabilities	7.2
Sensor Protection by Housing Design	79
Figure 43. Exploded views of the two different designs used for the “smart cylinders”. Design 1 (left) uses two simple ceramic plates to isolate the sensor from the metallic body, where design 2 (right) contains a ceramic sensor housing for protection of sensor in harsh fabrication environments [68].	80
Figure 44. CAD design of the two parts of the sensor housing, followed by the assembled housing	81
Figure 45. Sensor housing fabricated from machined alumina [68].	82
Figure 46. Alumina fabricated sensor housing using binder jetting AM technology.	84
Figure 47. Optical images of microstructure for EBM fabricated smart part, (A) entire microstructure view showing the evolution of the microstructure is paused, then continued; with a magnified view of (B) Second fabrication, (C) interface bonded section, and (D) first fabrication [68].	87
Figure 48. Optical images of microstructure for SLM fabricated smart part, (A) entire microstructure view showing the evolution of the microstructure is paused, then continued; with a magnified view of (B) Second fabrication, (C) interface bonded section, and (D) first fabrication.	88

Figure 49. SEM image of the EBM interface indicating the three individual areas where EDS analysis was performed.	89
Figure 50. SEM image of the SLM interface indicating the three individual areas where EDS analysis was performed.	90
Figure 51. Optical image detecting a defect from the stop-and-go EBM fabrication process, where certain powder particles were not melted during second fabrication.	92
Figure 52. Optical image detecting a defect from the stop-and-go SLM fabrication process, where pores can reduce the bonding of the two different builds	93
Figure 53. Voltage response based on compressive applied force obtained from “smart part”. The voltage response was obtained at frequencies of (A) 10Hz, (B) 15Hz, (C) 20 Hz, and (D) 25 Hz [68].	94
Figure 54. SLM fabricated “Smart fuel injector”	95
Figure 55. “Smart fuel injector” with embedded sensor fabricated using traditional.	96
Figure 56. Testing setup of SLM fabricated “smart fuel injector” detailing the fuel injectors componets.	98
Figure 57. Top view of SLM fabricated “smart fuel injector” spray tip with produced flame after combustion.	99
Figure 58. Temperature vs. time experienced by SLM fabricated “smart fuel injector”. Blue line represents values obtained by embedded sensor, where orange values are thermocouple readings.	100

Chapter 1: Introduction

1.1 Research Motivation

Additive manufacturing (AM) technologies are experiencing increased rates of adoption in industry. This form of manufacturing can in effect provide low volume production of customized products with added economic value. *Petrick et al.* stated that the rise of 3D printing and additive manufacturing in certain industries will soon replace the competitive dynamics of traditional economies of scale production with a production model based on an economy of one [2]. Additive processes already captured a large portion of the worldwide manufacturing market, with an industry value of \$5.2 billion in 2015, and is expected to grow five times to \$26.5 billion by 2021 [3]. The United States leads in the use of AM with an estimated 64% of total system installed worldwide [4]. Fabrication of metallic parts has also experienced increased interest along the growth of the AM market in general. The leading industries generating revenue from metal AM include: automotive (19.5%), medical (15.1%), and aerospace (12.1%) [4]. Certain powder bed-based systems have shown promising future in metallic component fabrication.

Per the Energy Information Administration (EIA), a total of 13% of the U.S. energy usage is destined to the fabrication of metal products. With the potential growth of AM metallic fabrication and the total energy that is designated for metallic fabrication, a comparative analysis is required to evaluate the suitability of each technology for a specific application. This research provides a thorough evaluation of three AM technologies used for producing metal components: binder jetting, electron-beam melting, and selective laser melting. The analysis is designed to serve as a decision tool for consideration of the use of AM for given applications by capturing metrics (i.e. capital cost, fabrication time, energy consumption, mechanical properties, and metallurgical characteristics) of parts fabricated by powder bed-based technologies. Though major advances have been accomplished, it is important to understand that AM technologies are still considered to relatively young, since processes have not gone through rigorous evaluations as compared to

traditional manufacturing. As such, there is limited information on the capabilities and properties of components produced using AM techniques when producing components directly from precursor powder.

1.2 Project Overview

This research focuses on the comparison between powder bed-based AM technologies and how they compare to traditional manufacturing of metallic components. The three powder bed-based AM technologies that were used for the comparison are binder jetting, electron beam melting (EBM), and selective laser melting (SLM). The comparison includes a look at the required capital cost for each technology, fabrication time from start to finish, and the amount of energy that each technology consumes during the fabrication process, as well as applicable post-fabrication processes. Several coupons fabricated by each of the three technologies were used to produce specimens for metallography evaluation. Mechanical properties were evaluated and compared for the three technologies in both as-fabricated and post-processed states. The mechanical properties were calculated based on ASTM standards and compared to wrought material's mechanical properties. One fractured tensile specimen was selected for analysis under a scanning electron microscope (SEM) to better understand the fracture mechanics characteristics of each technology. The fracture surface provided adequate information on the type of fracture mode that caused the sample's complete separation.

The final portion of this research included the fabrication of energy system components with embedded sensors, or "smart parts", using the three powder bed-based AM technologies. Smart parts are created by momentarily pausing the AM process, inserting the sensor, and then resuming the fabrication process. The layer-by-layer nature of AM technologies makes "smart parts" fabrication a reality. This research evaluates the interruption of the AM fabrication process,

accessing an incomplete component to embed a sensor, and conclude the full fabrication process to create a “smart part”. The interface created will be characterized to ensure proper bonding between the separate fabrication stages, by identifying possible differences in microstructure and chemical composition, affected by variation in cooling rates produced by system disturbance. “Smart parts” can be used for *in situ* monitoring for improved functionality and efficiency of energy systems. Both powder bed fusion technologies (EBM and SLM) were used for the fabrication of “smart parts” by means of a stop-and-go process, achieving the embedding of a piezoceramic materials within a metallic component that can tolerate harsh environments, such as high temperature and high pressure.

Chapter 2: Objectives

The expected growth of AM, and the increased use of these technologies for production of functional components, justifies a characterization study to evaluate each technology. This research identifies fabrication differences that may exist between EBM, SLM and binder jetting. The W.M. Keck Center for 3D Innovation is home to multiple powder bed-based technologies with capabilities of fabricating a large range of materials, and with tools available to reach these objectives.

The main objectives of this research are the following:

1. Perform an economical comparison between powder bed-based (EBM, SLM, and binder jetting) AM technologies. This includes the comparison of initial capital cost, fabrication time, and energy consumption.
2. To fabricate and characterize Inconel alloy 625 components built using the three powder bed-based AM technologies for microstructural and density evaluation.
3. To determine the effect of build orientation and a post-fabrication treatment (HIPed) on the tensile properties of powder bed-based fabricated Inconel 625.
4. To compare the mechanical properties of powder bed-based fabricated samples to ASTM standard F3056-14 specification for additive manufacturing nickel alloy with powder bed fusion.
5. To perform failure analysis evaluation of fractured samples that were built using the three powder bed-based AM technologies.
6. To evaluate the fabrication of “smart parts” using the three powder bed-based AM technologies as well as microstructure analysis to evaluate the metallurgical soundness of the interface created by the stop and go process.
7. To assess the functionality of sensors embedded into smart parts, by testing of components such as smart tube and smart injector in a combustor environment.

The basis of the first objective serves to define the bare minimum requirements to fabricate components with each technology. The analysis also compares the estimated amount of time and energy that each technology required in a number of case studies that try to emulate industry use. This first objective is covered in Chapter 4. Chapter 5 discusses objectives 2 through 4, focusing on the characterization of Inconel 625 fabricated using the three powder bed-based AM technologies. Initial characterization began with powder analysis, including powder morphology, flowability, average particle size, and chemical composition. Then, microstructure characterization (metallography) and mechanical properties (via tensile testing) were evaluated to determine the differences amongst the three unique fabrication processes. Chapter 6, which focuses on objective 5, includes failure analysis of previous tested samples produced by EBM, SLM, and binder jetting both as-fabricated and HIPed to determine the fracture mechanics of the samples (whether ductile or brittle fractures). Chapter 7 covers the final three objectives (objectives 6 through 8), which are focused on the design and fabrication of “smart parts” as a proof of concept using the three powder bed-based AM technologies. This chapter also describes the method of fabrication as well as the characterization of the interface created during the stop and go process to identify possible weakness and changes in microstructure, and concluded with an assessment of a “smart” fuel injector simulating substantial application performance.

Chapter 3: Literature Review

3.1 Additive Manufacturing

Additive manufacturing, commonly recognized as 3D printing, is a set of technologies where the fabrication of a complex geometric object is achievable directly from a CAD file in a layer by layer fashion. The most popular categories of AM processes include: binder jetting, directed energy deposition (e.g., laser-engineered net shaping) using metal alloys, material jetting, material extrusion (e.g., fused deposition modeling), powder bed fusion (e.g. EBM, SLM, direct metal laser sintering, selective laser sintering), sheet lamination (e.g. ultrasonic additive manufacturing and laminated object manufacturing) [5]. The ASTM standards group AM technologies into the following seven categories along with a brief description:

1. Binder jetting - Powders joined together with the use of an adhesive set by a print head
2. Directed energy deposition –Multi-axis mechanism feeds wire or powder onto a substrate by a high-energy source
3. Material extrusion – Material is drawn through a nozzle set on platform
4. Material jetting – Print heads jets melted material onto a build platform
5. Powder bed fusion – Energy source is used to melt/ fuse powder particles together
6. Sheet lamination – Sheets of material are bonded together by a welding source
7. Vat photopolymerization – A photopolymer resin is hardened by an ultraviolet light

All AM technologies must undergo analogous steps to reach a final product. Gibson *et al.* divides the general fabrication process of AM into the following main steps: creation of computer aided design (CAD) followed by the conversion of CAD model to STL (stereolithography) file format for system use. The AM machine then uses STL file manipulation for layering slicing, and the machine is then setup and fabrication proceeds. Upon completion, the built part is removed and post-processing is done depending on the intended application [6]. Figure 1 illustrates a generic AM process of a metallic mesh structure.

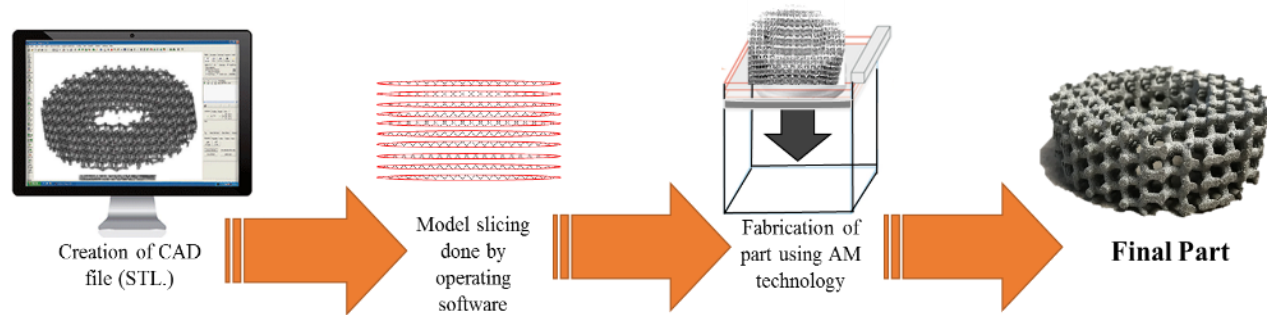


Figure 1. Generic AM fabrication Process flow diagram

Depending on the type of AM technology and the stock material being fabricated, the machine's software will select certain parameters specific to the material. Variables that can dictate fabrication time can include: part orientation, machine's layer fabrication speed, and processing parameters (for example, decreasing layer thickness can increase the build time significantly). Certain overhangs and/or design features (e.g. internal cavities) being fabricated may require fabricated support structures that can be created using the same build (parent) material or a secondary material, and is removed upon completion of final product.

The main difference between AM and conventional manufacturing processes is that the latter operates in a layer-wise fashion, achieving addition of material, as opposed to subtractive processes such as turning, facing, drilling, milling that consists of the removal of material. Due to this characteristic, the ASTM international committee F42 defines AM techniques as any "process of joining materials to make objects from 3D model data, usually layer upon layer, as opposed to subtractive manufacturing methods" [7]. Advantages that exist when utilizing AM over traditional manufacturing methods include reductions in the time-to-market due to high speed of process (product lead times), product customization with complete flexibility in design and construction of a product, increase in component complexity, material savings and reduction in material footprint, material recycle capacities, to know a fraction [8].

3.1.1 AM Technologies for Metallic Applications

Powder bed fusion, such as EBM and SLM, are successfully used to manufacture 3D structures with a variety of metallic materials such as stainless steel, maraging steel, cobalt, copper, chromium, titanium alloys, niobium etc. The process takes powder metal as the base material and uses an energy source (electron beam, laser, arc, etc.) to create dense parts [9]. Ti-6Al-4V parts gained a wide interest for aerospace, biomedical, and industrial applications because of its fracture resistance, fatigue behavior, corrosion resistance and biocompatibility [10]. Organizations such as NASA, the European Space Agency, and SpaceX, are all exploring the use of AM to fabricate igniters, injectors, and combustion chambers for rocket engines [3]. GE Aviation has one of the first additive jet engine component, a fuel nozzle with complex interior features fabricated by SLM technology and used in the LEAP engine (Figure 2A) [11]. Compared to its traditional counterpart, the SLM fabricated fuel nozzle is 25% lighter and five times stronger than traditionally manufactured nozzles [12]. These LEAP engines contain more than 20 fuel nozzles and are being used in aircraft such as the Airbus A320neo, the Boeing 737 MAX, and the Boeing 777X. Commercial and military aircrafts are also using AM parts as well. AM fabricated implants have become very attractive to medical industries because of the high levels of customization that can be attained with such technologies, thus enabling the production of patient-specific products cost-effectively [3]. A gained advantage over traditional manufacturing in this field is the ability to fabricate implantable devices with tailored porosity provides better bone cell attachment and fixation of the implant thus reducing premature failure and the need for revision surgery. Biomedical applications, such as pre-operative biomedical models and prostheses are already being integrated in the medical field [13]. A company based in Texas, 4WEB, announced in early 2015 that more than 3,000 of its Ti-6Al-4V titanium alloy orthopedic truss structures (Figure 2C) had been implanted in patients [3]. More than 20 different AM medical implant products have already achieved clearance from the U.S. Food and Drug Administration (FDA), where they range from cranial implants to hip, knee, and spinal implants [3]. Hip implants fabricated by EBM have

shown a reduction of the stress shielding effect and are more compatible with the human bone (Figure 2B) [14].

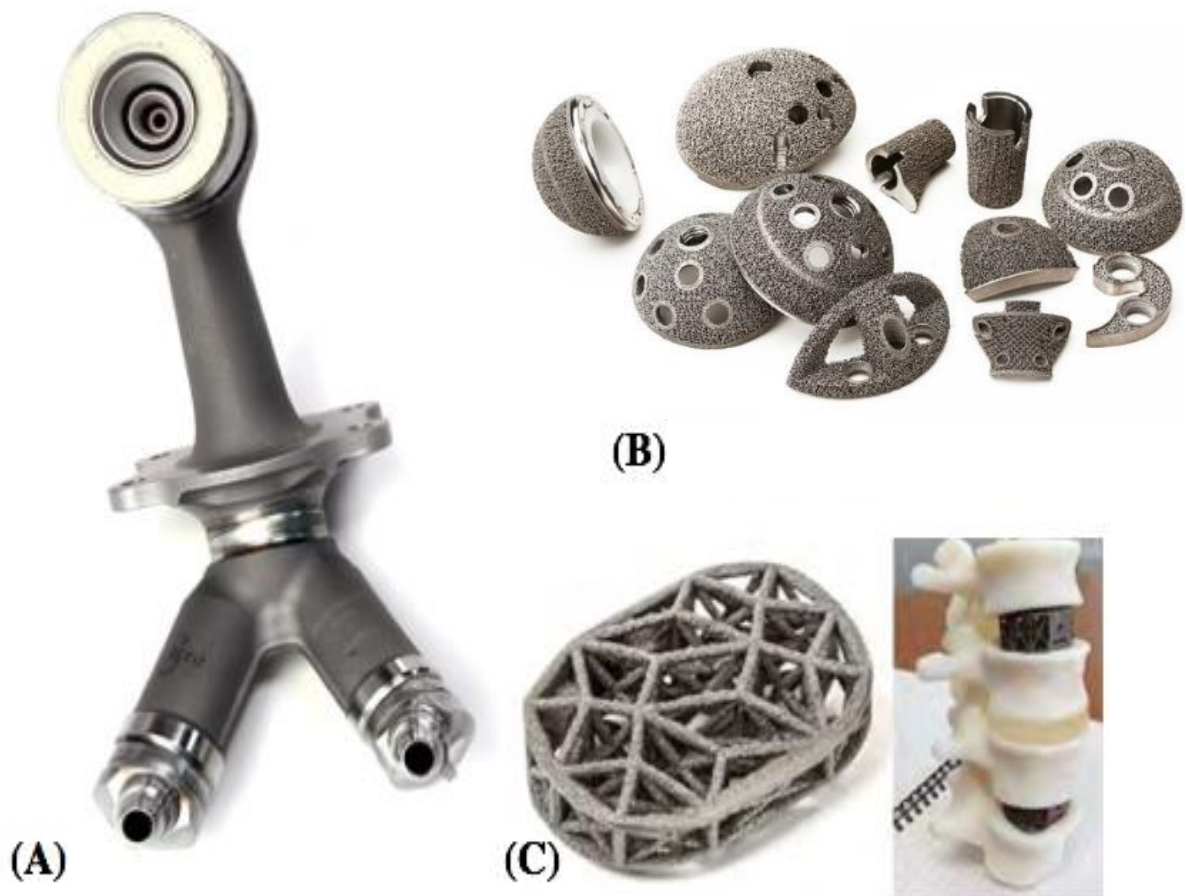


Figure 2. Powder bed fusion parts for (A) LEAP engine fuel nozzle (B) Hip implant (C) Truss structure implants. [11] [15] [3]

3.2 Electron Beam Melting (EBM)

The EBM process is a powder bed fusion AM fabrication technique that was developed and commercialized by Swedish company Arcam AB [16]. The basis of the process is the conversion of the kinetic energy of an electron beam into thermal energy that is used for melting particles of metal precursor powder [17]. An electron beam is generated from a filament, typically tungsten, heated over 2500 °C and generated using a 60kV potential. Magnetic coils are used to focus and direct the electron beam into select regions of a powder bed. A current flow is used to control the electron beam [17]. Figure 3 provides a schematic diagram of the major components of an EBM system, followed by a flow diagram defining the individual steps of fabrication. The electron beam column contains the filament used for the production of the electron, which is intensified by the lens. Powder hoppers store precursor powder and feed powder onto the build platform, where fabrication takes place on a start plate (stainless steel). EBM operates with metallic powder that ranges in particle size from 45-106µm in diameter that is spread as layers of a finite thicknesses using a raking mechanism. The fabrication process takes place under a high vacuum environment ($\sim 10^{-2}$ - 10^{-4} Torr), which helps avoid collision between the generated electrons and gas atoms for increased energy delivery efficiency. The vacuum also helps process highly reactive metals such as titanium and aluminum. EBM fabrication takes place in three steps. First, a preheating step that lightly sinters the powder (~ 0.4 to 0.6 material's melting temperature, T_M) using a low current high-speed electron beam to reduce residual stresses by maintaining a low thermal gradient during fabrication [18]. In the second step, the lightly sintered powder is melted with an increased current and reduced scan speed to reach the material's T_M . In the third step, the build platform is lowered by the height equivalent to a layer thickness, and a fresh layer of powder raked in. The process is repeated until part fabrication is completed. The fabrication process is

summarized in Figure 4. The pre-heat and melt scan steps, necessary to melt the powder particles, is where the majority amount of energy is demanded. After fabrication, a block of sintered material that contains the solid metal component in it, is removed from the system and the sintered powder removed using a powder removal system (PRS) that uses compressed air.

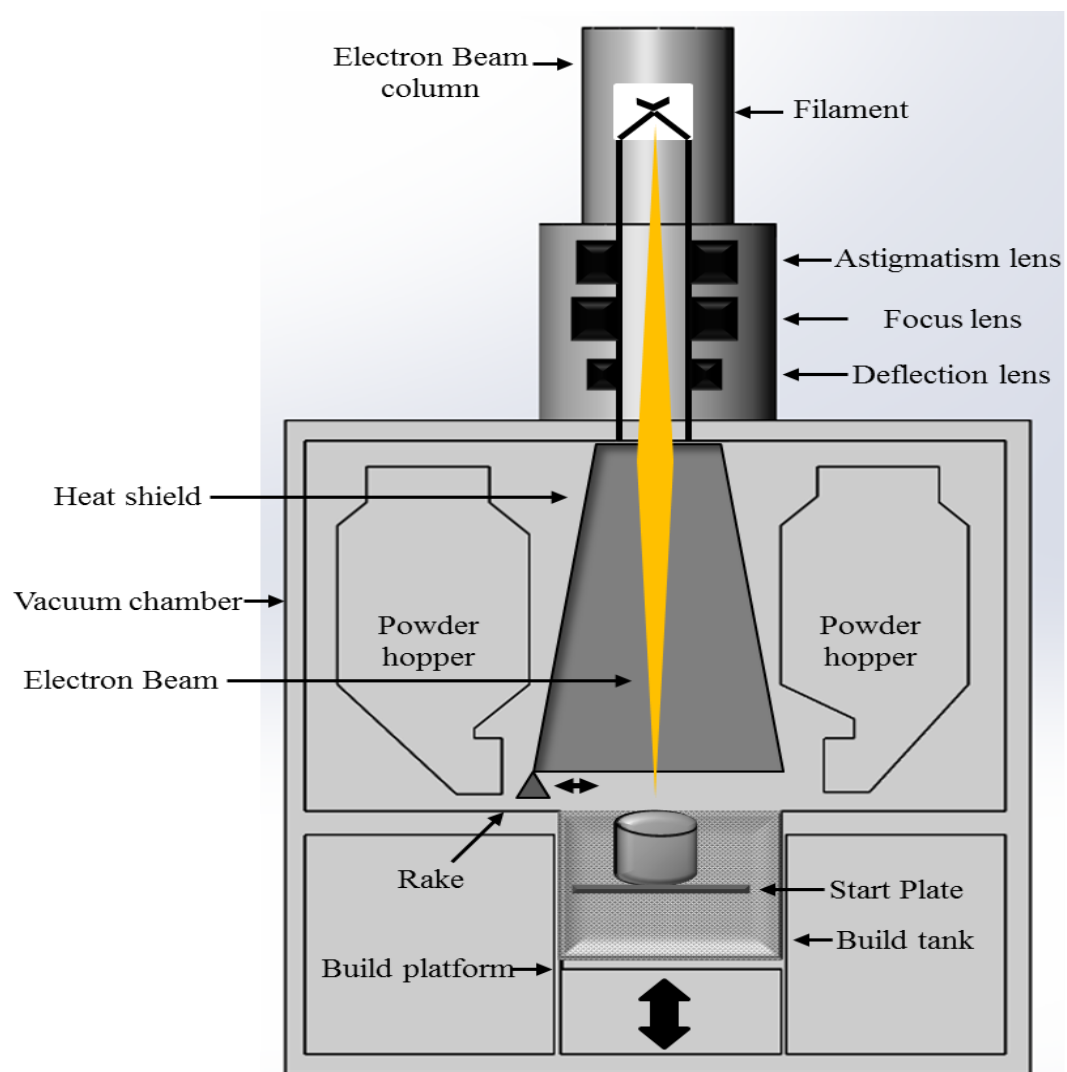


Figure 3. Schematic diagram of EBM machine and components

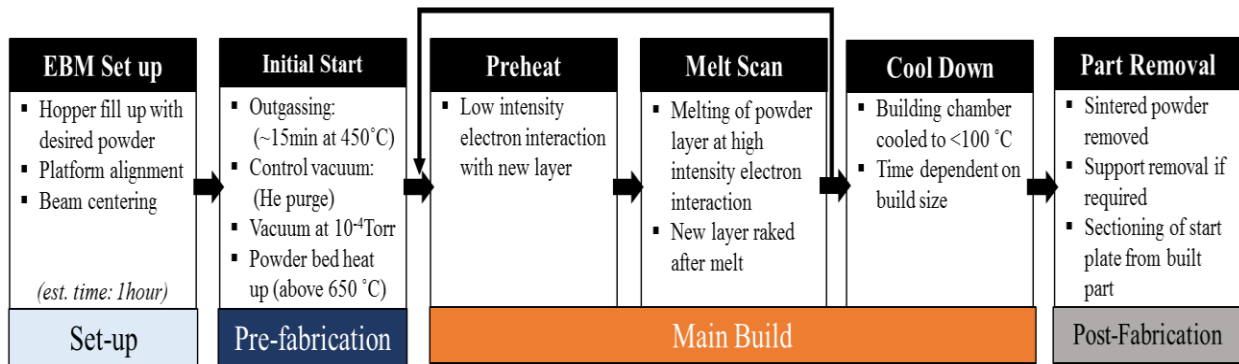


Figure 4. Flow diagram of the fabricating process for EBM with each individual step detailed.

Support structures are built for parts with large overhanging features (or with surfaces at angles of <45° from horizontal), and removed after fabrication using hand tools. In comparison to other powder bed fusion processes such as SLM, EBM-fabricated parts contain less residual stresses post-fabrication (mainly due to the pre-heat process) and the part's mechanical properties are more comparable to wrought or cast material. One of the promising aspects of EBM allowing for an increase in production rates is the high scanning speeds that can be achieved by the electron beam (8,000m/s for EBM [17] compared to 7m/s for SLM [19]) due to the use of magnetic coil for focusing as well as for deflecting the beam, while SLM is limited by the speed of galvanometric mirrors for optical focusing [6].

3.3 Selective Laser Melting (SLM)

Selective laser melting (SLM) is also categorized as a powder bed fusion technology that selectively processes precursor powder in a layer-wise fashion using a high-energy source [20]. The main difference is the energy source employed in SLM. In contrast to EBM, SLM uses the

energy of a laser beam, typically having a power in the range of 200-1000W, to melt powder particles and fuse them together (typically to 10-45 μ m in size). Some machines are implementing multiple lasers to reduce fabrication times [3]. Finer powder that is utilized for fabrication of SLM parts results in parts with improved surface quality that might be preferred for certain applications [21]. Successful fabricated materials by SLM include Ti-6Al-4V, Co-Cr-Mo, and Inconel grade alloys [22]. The process is done in an inert gas environment, with either argon or nitrogen gas, with fabrication done at slightly elevated temperatures of approximately $\sim 200^{\circ}\text{C}$ in the build chamber. For some materials, the process usually results in the buildup of high residual stresses requiring a post-fabrication heat treatment. In SLM fabrication, a laser is directed by galvanometric mirrors (found within the scanning mirrors component of system) to print design onto a start plate (typically stainless steel) located within the powder bed by either a contour or hatch scan. The contour step creates the CAD's specified shell, where the laser at low speed and energy melts the powder. Then, the process executes a hatching step, where the inner design of the geometry is melted. During the hatching step, the system reduces the scanning length by creating an alternating pattern, such as a check board pattern, to reduce residual stresses buildup. Flow diagram of the fabrication process is detailed in Figure 5. The heat-treatment selected is contingent on the fabricated material and desired for part application. The laser only comes in contact with powder specified by the CAD design, melting the contour and interior shape, resulting in a fully dense layer. Unused powder is not affected during the fabrication process and is considered to be reusable for other builds. Figure 6 is a schematic view of the SLM system and the essential components within it, which most importance are the laser source and the scanning mirrors. Fabrication takes place on the start plate, located within the powder bed arranged by the hopper and recoater. The flow diagram details the steps of the fabrication process that are required to fabricate by SLM technologies. A feature for SLM fabricated components are melt pool scans in the part's microstructure SLM fabricated metals (Ti-6Al-4V and Inconel 718) due to the melt scans that are done by the laser [22].

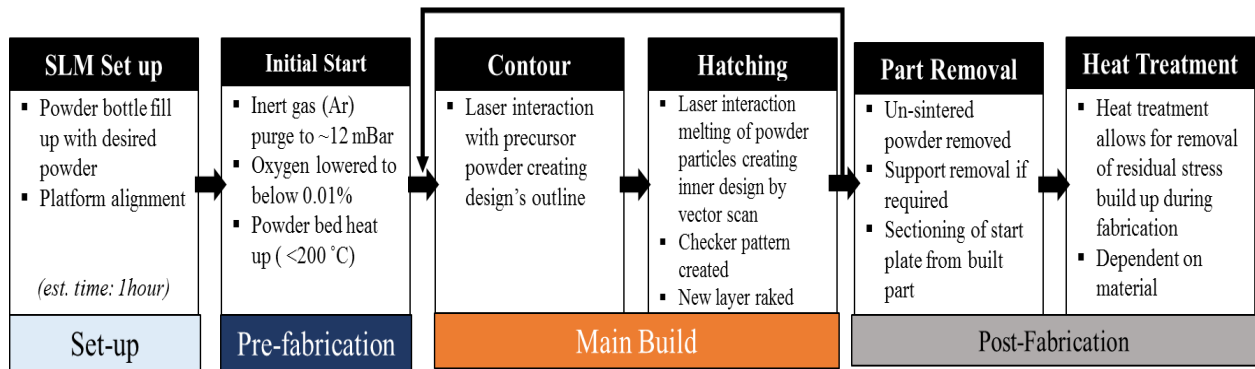


Figure 5. Flow diagram of the fabricating process for SLM with each individual step detailed.

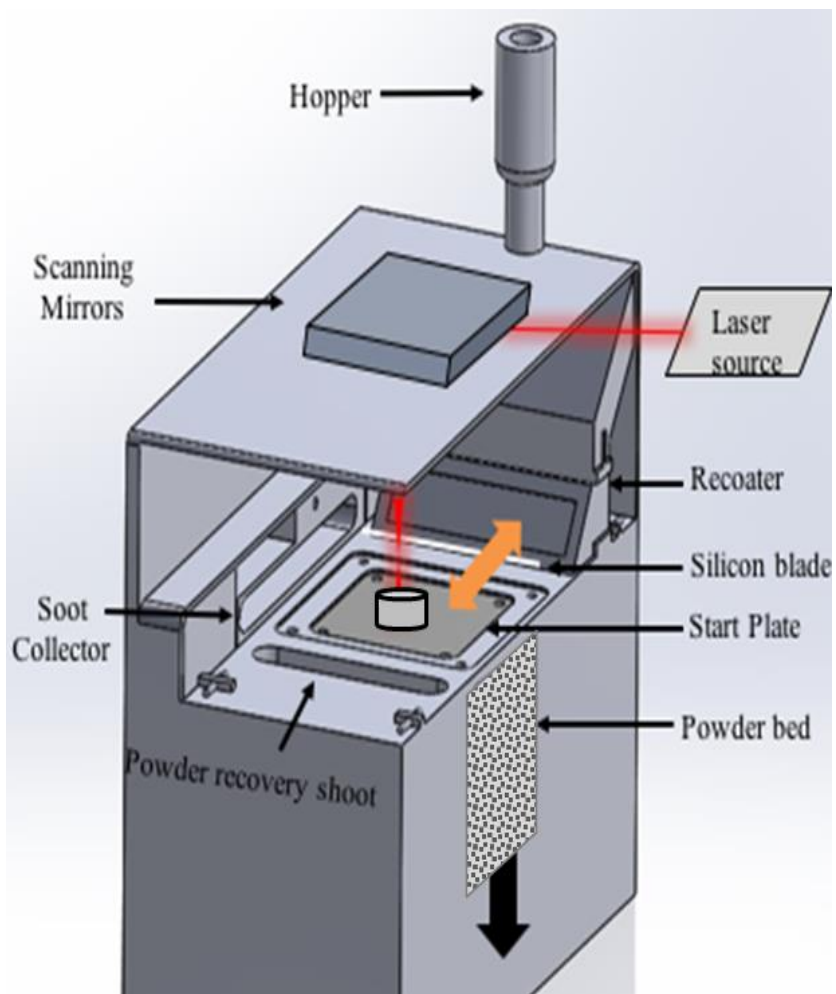


Figure 6. Schematic diagram of SLM machine and components

3.4 Binder Jetting

Binder jetting technology joins powder particles together in a layer-by-layer fashion with the use of a liquid binding agent dispensed using a piezo-electric based print head. The binder can be either a water-based liquid or a polymer-based liquid [3]. The binder is selectively set onto the powder bed subsequently joining powder particles together to hold the desired shape. Certain systems use a two piston driven tanks; the first tank provides the powder supply and the second tank is where fabrication is accomplished, while others have used a hopper/ recoater mechanism for powder layout. The powder layers are spread with the use of a roller leaving behind a uniform spread layer. A print head deposits binder droplets onto the powder bed [23], and a heater raises the build bed temperature to $\sim 55^{\circ}\text{C}$, drying the binder. This printing process is repeated until part fabrication is complete [24]. After fabrication, a binder curing step is required, taking place in an oven, where the parts are heated to 195°C for 8 hours (standard for all materials) resulting in harden parts able to withstand excess powder removal. The result of this step is also referred to as creating a green body part. Powder extracted from green body can be sieved out and reused for future fabrications. After the green body is formed, post-fabrication sintering is required to obtain a final part. Using this method, sands, metals, glasses, and ceramics have successfully been fabricated at high densities [3]. High temperature ceramics materials, like alumina and barium titanate, have had favorable fabrication results, giving binder jetting an advantage when compared to EBM and SLM [24] [23]. SLM limitation for the fabrication of high temperature ceramics is that the energy created by the laser is not capable of melting such materials. EBM on the other hand, requires a conductive material for the electron to transfer its high intensity energy. The fabrication process is done with minor energy use, in comparison to EBM and SLM that require high power lasers or electron beam, but a timely post-fabrication process may not be ideal for single part fabrication in regards to the sintering profile. Figure 7 shows the schematic diagram of the fabrication of a part using binder jetting technology along with the flow diagram (Figure 8) detailing the steps followed during this process.

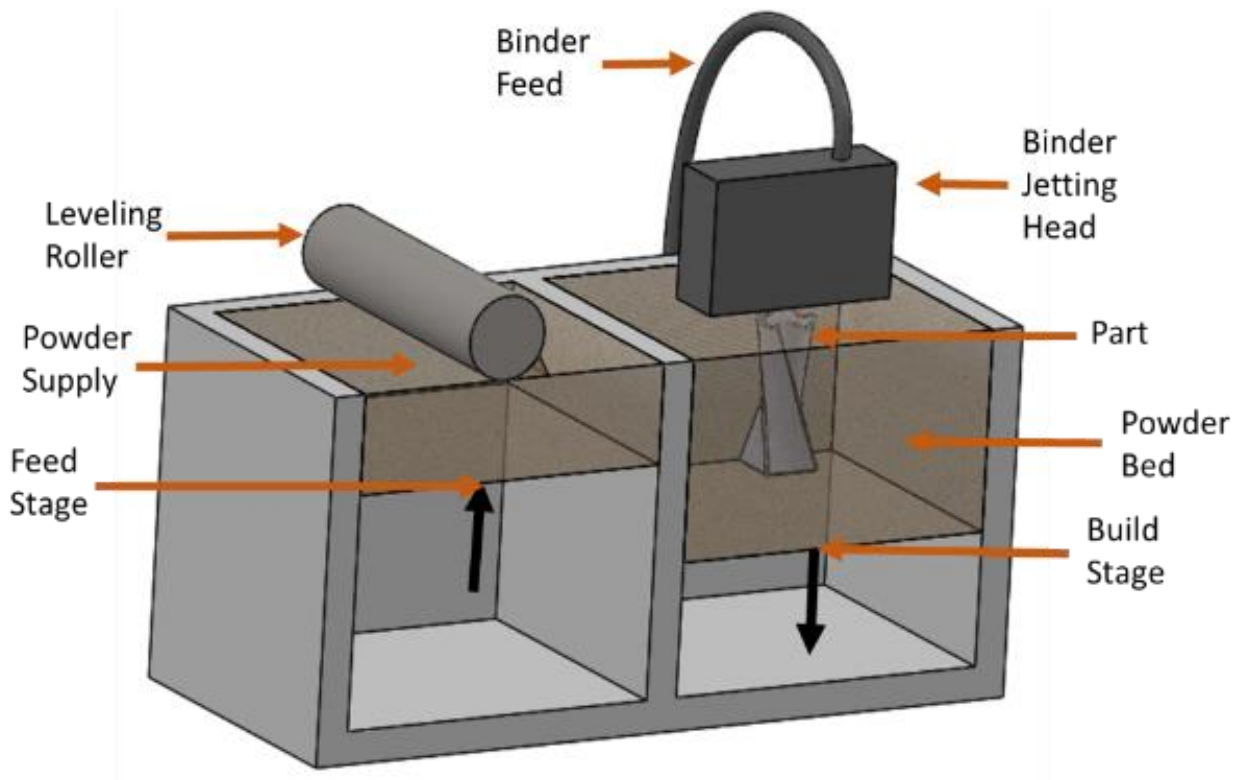


Figure 7. Schematic diagram of binder jetting machine [23]

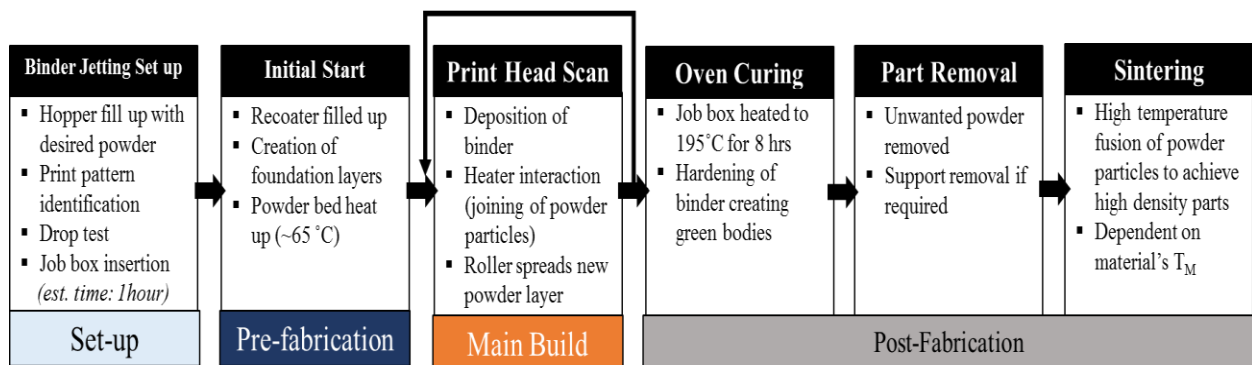


Figure 8. Flow diagram of the fabricating process for binder jetting with each individual step detailed.

3.5 INCONEL Alloys

One class of materials that can be processed using all three technologies previously described are nickel based superalloys. Nickel based superalloys are responsible for over 50% of the weight of advanced aircraft engines [25]. Typically these alloys are able to withstand the highest temperatures present in turbine engines ($>850^{\circ}\text{C}$), due to precipitation hardenability [25]. The main alloying elements including nickel, titanium and aluminum, form intermetallic precipitates (or γ'), providing resistance under elevated temperature conditions. [25]. However, the formation of γ' precipitates reduces the workability of these nickel superalloys, and hence processing has to be done through methods such as casting or powder metallurgy [25].

In this work, two alloying forms of Inconel (625 and 718) metals were used for the benchmark study of binder jetting, SLM and EBM. Lead times and design costs can be significantly reduced by fabrication of these alloys using powder bed-based AM technologies in comparison to by conventional machining, by reducing excessive tool wear and low material removal rates [26] [27]. Build parameters for Inconel 718 are established for all three technologies, whereas those for Inconel 625 are only established for SLM and BJ. Although not commercially available, EBM processing parameters previously developed at the Keck Center at UTEP were used.

3.5.1 INCONEL 718

Inconel 718 is a widely used superalloy that is strengthened primarily by the metastable phase γ'' (Ni_3Nb), but becomes unstable at temperature ranges of 650 to 815°C [25]. Inconel 718 has been used in gas turbine engine parts and liquid fuel rocket motor components, as well as marine applications because of the material's high toughness when exposed to cryogenic temperature characteristics [28]. Inconel 718 is known to have excellent welding characteristics, resistance to post weld edge cracks, and oxidation resistance at high temperatures [29]. These characteristics made Inconel 718 an excellent candidate for additive manufacturing. In this research, this material was used for the economical comparison studies for EBM, SLM, and binder jetting.

3.5.2 INCONEL 625

Inconel 625 is a nickel-chromium alloy with molybdenum and niobium alloying elements [25]. Inconel 625 is used because of its high strength, similar to Inconel 718. The addition of molybdenum and niobium creates a stiffening effect with the nickel-chromium matrix, eliminating the need for precipitation hardening treatment [30]. Inconel 625 has diverse industry applications such as aerospace, marine, and petrochemical [31]. In the aerospace industry, it has been applied to gas turbine engine exhaust systems, spray bars, thrust reverser systems, turbine shroud rings, fuel/hydraulic line tubing and bellows are a few examples of how Inconel 625 is used in the manufacturing process [32]. The alloy is usually found in aerospace applications due to its excellent combination of strength at both ambient and elevated temperatures, corrosion resistance and ease of fabrication, [31]. Inconel 625 is widely used in marine and nuclear industries due to its high corrosion-fatigue strength and resistance to harsh environments [33]. Given the alloy's multipurpose capabilities and range in applications, Inconel 625 has been implemented in several manufacturing processes such as casting, powder metallurgy, spray forming, weld overlaying and co-extrusion of piping components [34]. Currently, the material is experiencing significant interest for fabrication of dense components through additive manufacturing techniques. This material was also used in this research to make the comparative analysis of the three powder bed-based AM technologies.

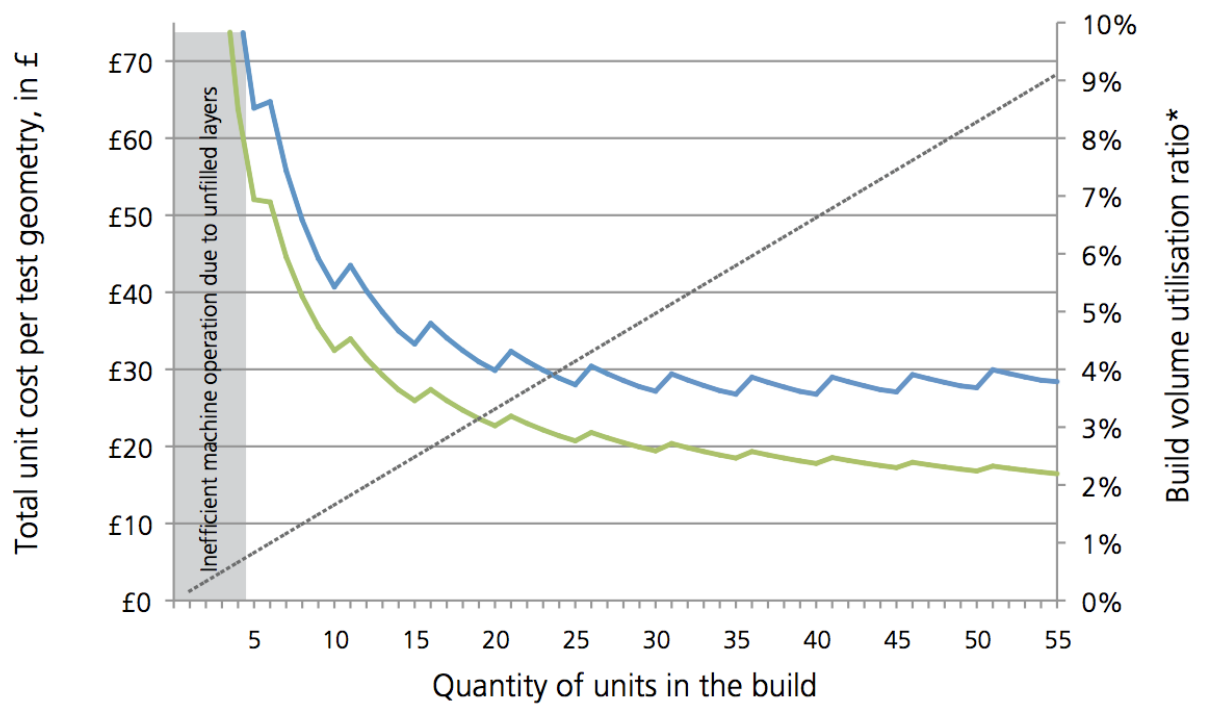
3.6 Powder Bed-Based Systems Comparisons

Due to the expansion of powder bed-based technologies in industry demands, these powder-bed based techniques need further research in areas of materials' fabrication, applications, system resources, and part performance. There have been reviews conducted, such as a recently done by *Murr, et al.*, where fabricated metal components by additive manufacturing were compared to each other [18]. The review provided a brief but comparative overview of components fabricated using EBM and SLM processes, however, only hardness properties were tested [18]. The study identified microstructural characterization of the two technologies and how

the formation of grains differs due to each technology's solidification process. The review attempts to provide a brief overview of metallic components fabricated by EBM and SLM technologies. Its main focus is a characterization in metallic components with the use of transmission electron microscopy (TEM) and microstructure, and x-ray diffraction (XRD). However, with a limited study on mechanical properties, a continuation was deemed necessary.

Other studies, evaluating cost of fabrication per parts by AM technologies have been investigated on modern AM platforms. *Baumers et al.* conducted a study that fabricates complex geometric parts using power monitoring (for energy consumption readings), where experiments were performed on a MTT SLM250 SLM system and an Arcam A1 EBM machine. A multi-purpose power meter was used to determine the total amount of energy consumed for two build scenarios: (1) full build volume fabrication and (2) single part fabrication in the middle of the build chamber [35]. Conclusions from this study suggested that in terms of energy consumption per fabricated part, SLM processes consume around 7.34 kWh while the EBM processes use around 2.21 kWh [35]. Numerous variables that limit the findings of the case study conducted include: no system's capital cost in the analysis of production cost for parts, as well does not include any required post-fabrication processes (cutting of start plate, heat treatments) for each technology. Also, *Baumers et al.*, states that the build envelopes for the comparison are not similar, in size, and may have affected the results. The final variable that is different in the study is that EBM and SLM systems fabricate different materials (EBM: Ti-6Al-4V and SLM: SAE 316L). In a follow-on study, *Baumers et al.* analyze the economic cost for the fabrication of a SLS system [36]. A total of 14 experiments were performed, where only 10% of the build volume with test parts was constructed. Results were then multiplied by a utilization factor, determining the build cost of the run. Factors that were accounted for in the study included: probability of failure rate after the deposition of N layers, indirection (e.g. machine cost depreciation period, maintenance, and consumables). It was concluded that cost decrease rapidly initially but then cost began to rise slightly as capacity utilization near max. A graph plotted the cost estimate against the quantity of

the volume (Figure 9) showed that a unit cost behavior of high inefficient is seen for small volume builds.



— Total unit cost estimate (with failure and rejection) — Total unit cost estimate (without failure and rejection)
 Build volume utilisation ratio

* in the used model, a ratio of 9.11% corresponds to full capacity utilisation, as shown in Figure 1

Figure 9. Unit cost model versus capacity utilization [36]

The research goal of this project was to compare the total capital cost required to fabricate using EBM, SLM, and binder jetting processes. The analysis included cost of the AM system and any ancillary equipment necessary for the fabrication process. The fabrication time included the set-up time for each system, printing time, and any post-fabrication process required by each technology. For the fabrication time and estimation of energy consumption, the amount was determined for a single fabricated layer and results were multiplied according to build size to generalize a complete fabrication build, similar to *Baumers et al.* Multiple case studies were evaluated simulating industry usage of each technology to understand how each technology differs from one another during the fabrication process. A final comparison of mechanically tested specimens that were fully fabricated the three technologies was achieved to continue previous findings.

3.7 Advance Application Demonstration of Future AM Fabricated Components

A current topic of interest for powder-bed based AM techniques, is the ability to create “smart” components with added functionality through the incorporation of sensors within their structure. Sensors used in the energy systems (i.e. pressure tubes, air fuels, and combustion engines) endure harsh environments including high temperatures and pressures, and aggressive chemicals. For instance, the recorded temperature and pressure of a combustor inlet during operation of an advanced aircrafts’ gas turbine resulted in 810K and 2,760kPa respectively [37]. These exposure conditions impose limitations on the available sensors for such applications. Aside from the reduced survivability of the sensor, other factors complicate their use in this conditions that include the need for cable interconnects, reduced aerodynamics and performance of the system where the sensor is installed [38]. By embedding a sensor within the component, real-time feedback can provide readings such as temperature, pressure, and structural health in a non-invasive way. When accurate in-situ monitoring is gained, performance metrics are identified providing room for improvements of the process.

For a simple sensor demonstration, a piezoelectric ceramic material can be used as the sensing mechanism due to the piezoelectric and pyroelectric effects. Piezoelectric effect is the ability of a material to generate an electric charge when a dynamic force or pressure is applied onto the material. This allows the piezoelectric material to sense strain, pressures, and forces [39]. Similarly, the pyroelectric effect occurs when an electric charge is produced on the material by a change in temperature, thus allowing temperature sensing [40].

In this research, “smart parts” are referred to components created, using the three AM powder-bed techniques previously mentioned, with embedded piezoceramic sensors to provide high temperature and pressure feedback from exhaust tubes, gas turbine fuel/air premixers, etc. By using AM, parts were fabricated at a lower cost with a more efficient process. The technique employed consisted of pausing the regular build process to introduce a sensor, and then resuming the process to achieve a monolithic structure with the embedded sensing functionality. In this research, the “smart parts” were built and tested to characterize their properties and sensing capability. Several embedding techniques have been proven. For instance, *Li et al.* fabricated nickel composites with some metal structures with Fiber Bragg Grating (FBG) fiber optics embedding for sensing capabilities [41]. The process was achieved by magnetron sputtering and electroplating, and the component was able to read temperatures in the range from 20 to 260°C [41]. *Aguilera et al.* used fuse deposition modeling (FDM), using a paused fabrication method, was capable to embed a 3-phase performance motor onto thermoplastic substrate creating a 3D printed motor [42]. The process was achieved by embedding nine electromagnets, six magnets, two ball bearings, and electronic speed controller onto an ABS substrate with multiple process pauses (total of 5) to accomplish a final working motor [42]. The fabrication process was carried out by creating internal slots, within the design for insertion of the embedded components. Interconnection of components were also created by soldering components during process stops.

By adapting the paused process and the use of powder bed-based technologies to substrate fabrication, the embedding of a piezoceramic capture within a metallic component is achievable. This selection of material for “Smart parts” allows potential to withstand the high temperature and

pressures that may be present in the energy system. *Terrazas et al.* demonstrated the concept of ‘stop and go’ in EBM (powder bed fusion AM technology) by producing a multi-material part (Ti-6Al-4V and copper part) [43]. The process was done in multiple steps where the EBM process was stopped once half of the part was done (Ti-6Al-4V). Then a second fabrication step was performed using copper resulting in a multi-material final product. Misalignment was identified in the research and it was found to be caused by the initial beam centering, due to the human error and variability during setup.

Using the findings from the literature review as a starting point, this research implemented a similar methodology to stop and resume the AM processes to enable the insertion of sensors and produce “smart parts”. This was done for the technologies of interest; EBM and SLM. A key achievement of this research was the replication of the methodology that had previously been demonstrated for EBM and SLM techniques. The research goals of this project were to fabricate “smart parts” using the powder bed fusion AM technologies, to evaluate sensor functionality, and to characterize the metallurgical soundness of the interface created during the stop and go process.

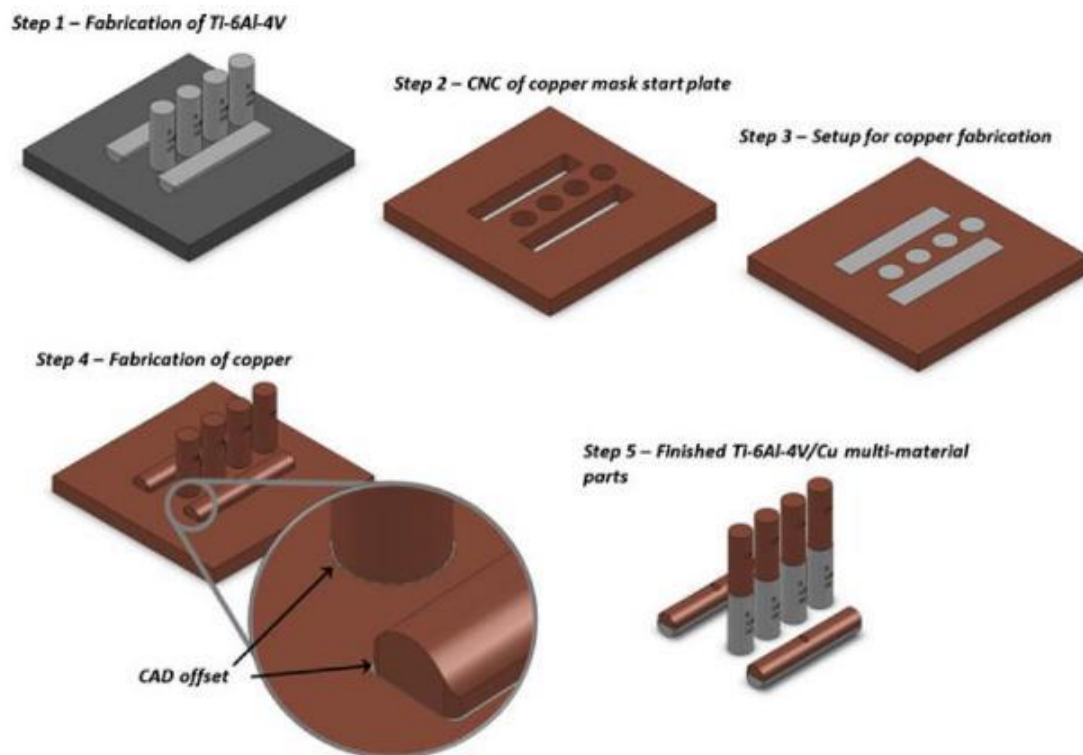


Figure 10. Multi-material fabrication process using EBM [43]

Chapter 4: Fabrication and Energy Consumption Model Comparison between Powder Bed-Based AM Technologies

As previously mentioned, certain companies are moving to the implementation of AM technologies for fabrication of metallic components. The United States is the leader as far as total number of AM systems purchased, amounting to 64% of the total sales worldwide [44]. By having an economic evaluation, a better understanding of the required resources and costs associated with implementation of powder bed-based technology for part fabrication.

This chapter presents that analysis, to compare the initial cost of equipment, fabrication time, and an estimation of amount of energy consumed during the full process of fabrication of an Inconel 718 component using each powder-bed based technology. Two designs were used for this analysis to draw similarities to actual industry usage. The first part fabricated was a cylinder, 10 mm in radius by 10 mm in height (undersized part), and the second was a 10 mm radius by 200 mm height (tall part). For all experiments performed, the layer thickness was selected at 50 microns for all technologies. The parts were then used in four unique case studies to evaluate machine use under different bed packing and height conditions. For example, the studies performed included the fabrication of a single part for both undersized (case study 1) and tall (case study 2); as well as multiple parts, totally filling up the available build envelope in each machine, also for undersized (case study 3) and tall (case study 4) components. A generic representation of the 4 case studies is shown in Figure 11. These four case studies emulate a range of situations that may occur as the AM systems are used for production. For this study, energy consumption was calculated as power rating of the machine over the time lapsed for the completion of one single layer where results were then extrapolated to estimate energy consumption of the full build. The fabrication time for all proposed scenarios was estimated using available simulators for each technology, which consider the scanning speed and total surface area to be scanned. The three machines that were used for comparison were an Arcam EBM Q20 Plus machine, an ExOne M-Flex, and the SLM Solutions 280HL, due to similar build envelopes. Systems for EBM and SLM technologies are not located at the University of Texas at El Paso (UTEP).

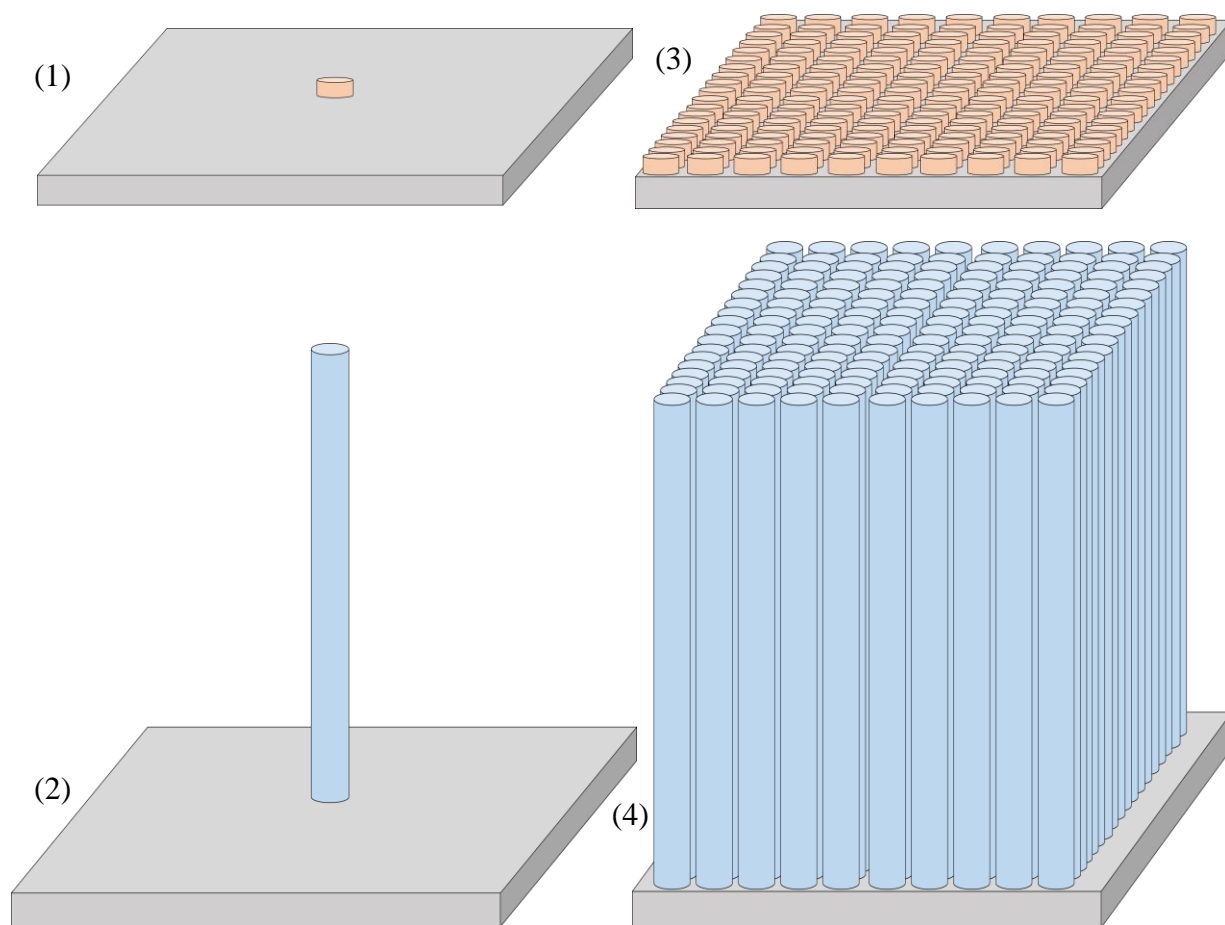


Figure 11. Generic representation of the 4 case studies used for the cosst model simulation

4.1 Capital Cost

The capital cost for each machine accounts for the largest expense overall. The most affordable system is the ExOne M-Flex (binder jetting) system which will cost about \$0.45 million. Binder jetting technology does require a secondary curing step, an oven costing \$20,250 USD, requiring an oven as ancillary equipment. By comparison, capital costs for powder bed fusion systems are \$1.09 million for the Arcam Q20plus, and \$0.73 million for the SLM Solutions 280HL. These prices are based on retail cost provided by each system manufacturer. Both EBM and SLM also require ancillary equipment in the form of a chiller and transformer, included in the cost of the fabrication system. The total cost per capital equipment is evaluated in USD, which include the prices of any ancillary equipment that may be required in post fabrication and essential component to run each system. The equipment includes the furnace for the sintering step required by binder jetting and heat treatment required for SLM components. Both EBM and SLM required a band saw to remove the fabricated components from the start plate. Figure 12 illustrates the comprehensive equipment cost necessary to fabricate functional parts accompanied by a table for the individual cost of any equipment.

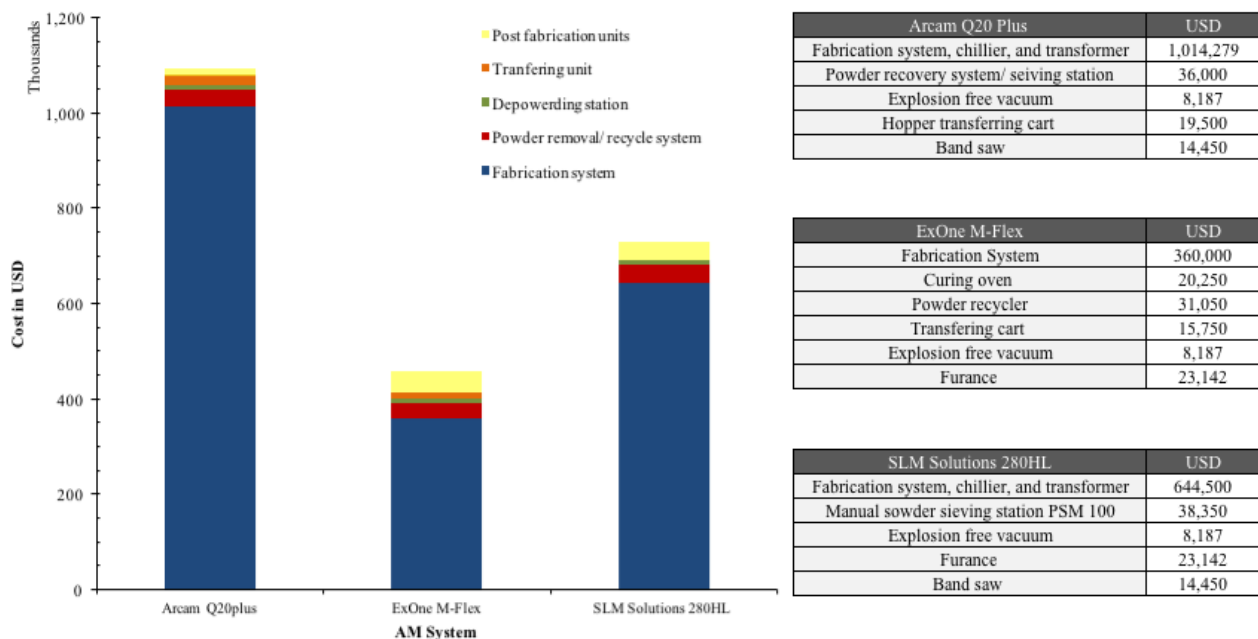


Figure 12. Cost comparison of equipment required to achieve part fabrication using each powder bed-based system. A breakdown list indicates the cost of required equipment.

4.2 Single Part Case Studies

Case studies 1 and 2 compare the fabrication of a single component with intent to model a more personalized consumer based component. For all studies performed, the three technologies were assigned a fixed 1 hr. setup time. AM systems are considered more flexible for the fabrication of customizable components such as patient specific implants however as other case studies have shown AM technologies run at high inefficient with full volumes fabrication. For case study 1, SLM provides the most efficient fabrication time yielding about 9.8 hr. followed by EBM at 13.3 hr., and finally binder jetting at 25.6 hr. For case study 2 the fabrication times are SLM 17.1 hr., EBM 55.4 hr., and binder jetting 72.1 hr. Figure 13 shows the results of the two single part scenarios studied.

The results obtained for the amount of energy consumed during part fabrication are summarized in Table 1: EBM fabrication consumed 87 kWh for case study 1 and 1,115 kWh for case study 2, binder jetting consumed 230 kWh for case study 1 build and 328 kWh for case study 2, SLM fabrications process consumed 107 kWh for case study 1 and 203 for case study 2. The majority of the energy consumed by the binder jetting process occurs during the post-fabrication steps (i.e. curing for 8 hr. and 13.5 hr. for sintering). These results suggest that binder jetting is not practical technology for production of single component. For EBM, an approximate 96% of the energy expenditure occurs during the main build process (refer to flow chart in Figure 4) that includes raking, pre-heating, and sintering. For the two case studies fabricating a single part, a large energy consumption of the EBM process occurs during the printing process, where the pre-heat and cool down of the system is constant. For the case of SLM, this technology performed with efficient results under the two single-part scenarios. This is in part due to the low time required for preconditioning of the fabrication chamber that includes a heat-up to $\sim 200^{\circ}\text{C}$, and also due to the small area needed to be scanned by the laser. Nevertheless, SLM parts must undergo stress relief heat treatment process amounting to $\sim 98\%$ for case study 1 and 58% for case study 2 of energy consumption.

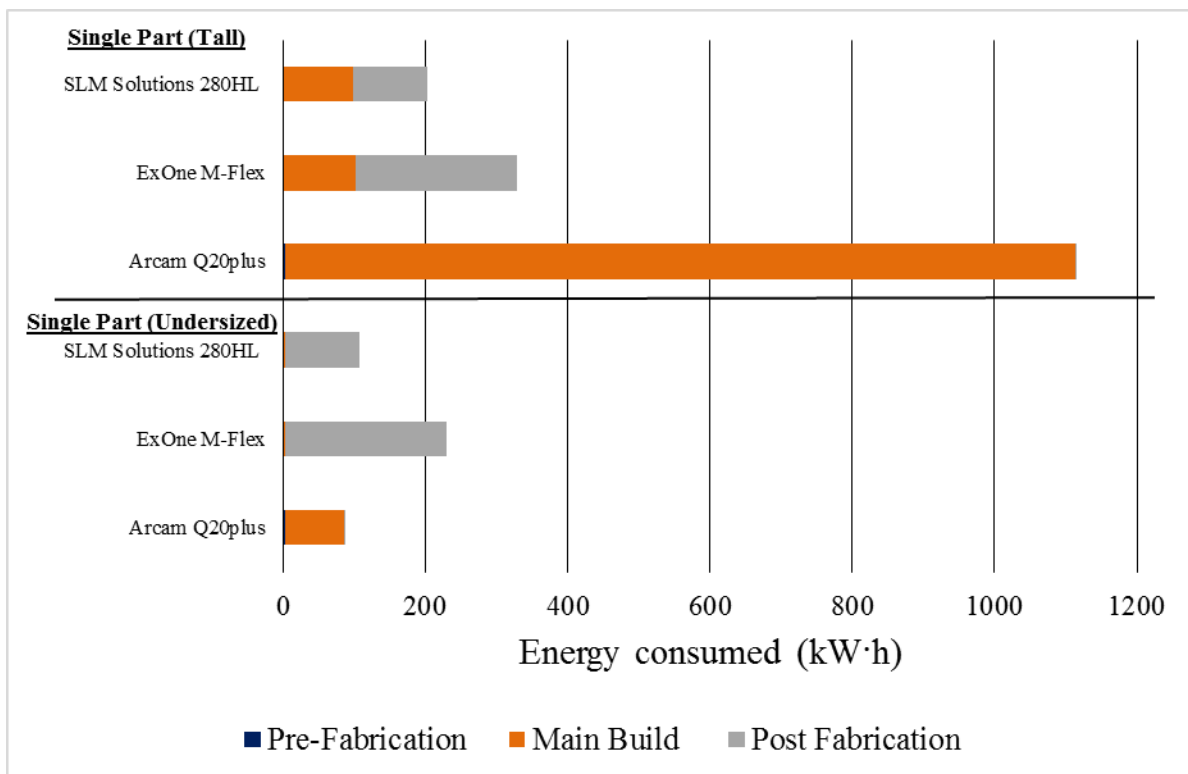
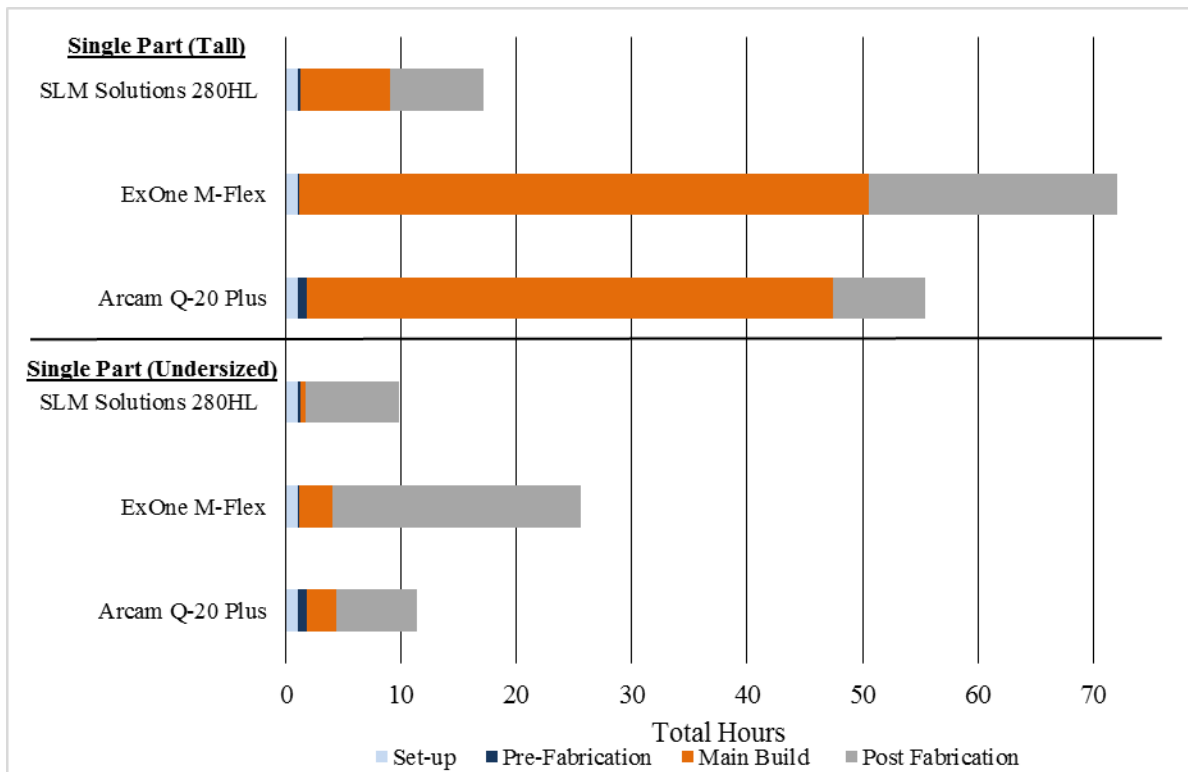


Figure 13. Fabrication time (hours) and energy comparison (kilowatt hour for single-part case study 1&2

Table 1. Energy consumption for case study 1&2 based on the individual steps for each technology

Undersized				Tall		
	Arcam Q20plus	ExOne M-Flex	SLM Solutions 280HL	Arcam Q20plus	ExOne M-Flex	SLM Solutions 280HL
Pre-Fabrication	2.02	0.01	0.6	2.02	0.01	0.6
Main Build	83.9	3.04	1.8	1111.9	101.2	97.4
Post Fabrication	1.1	226.8	104.6	1.1	226.8	104.6
Total (kWh)	87.1	229.9	107.1	1115.01	327.9	202.7

4.3 Multi-Part Case Studies

The multiple part fabrication studies were performed to gain insight on system performance during production of multiple components or large layer area. Case study 3 was based on the fabrication of 160 undersized cylinders (10mm Z-direction) occupying the maximum XY envelope available. Similarly, case study 4 was based on the fabrication of 160 tall cylinders that in this case occupy the maximum build volume (XYZ) envelope. As was the case for the previous case studies, a 1 hr. setup time was assigned for all AM systems.

Full results for energy consumption can be found on Table 2, with graphical representation on Figure 14. The results from case study 3 indicate that EBM fabrication lasted about ~13 hr., followed by binder jetting (~26 hr.), then SLM at ~83 hr. Correspondingly, these fabrication times translate to energy expenditures of 213 kWh for EBM, 230 kWh for binder jetting, and 1,018 kWh for SLM.

The results for case study 4 were as follows: 106.8 hr. for EBM, 80.4 hr. for binder jetting, and 1,475 hr. for SLM (due to the scanning speed of the laser). The corresponding energy consumption results were ~1,891 kWh for EBM, 357 kWh for binder jetting, and 18,005 kWh for SLM. These results suggest that binder jetting was the more efficient technique for fabrication under the two multiple part scenarios studied when compared to SLM and EBM. Part of the gains in efficiency for binder jetting in multiple part case studies, stem from the ability to post-process (cure and sinter) a greater number of parts simultaneously rather than doing these steps in a per part basis. EBM is also able to perform somewhat efficiently for fabrication of multiple parts due to the high hatching speeds that can be attained by the electron beam. In the case of SLM, however, mechanical actuation of mirrors to direct the laser, substantially reduces the scanning capabilities thus increasing fabrication time.

Table 2. Energy consumption for case study 3&4 based on the individual steps for each technology

	Multi-undersized			Multi-tall		
	Arcam Q20plus	ExOne M-Flex	SLM Solutions 280HL	Arcam Q20plus	ExOne M-Flex	SLM Solutions 280HL
Pre-Fabrication	2.02	0	0.6	2.02	0	0.6
Main Build	209.8	3.8	913.5	1888.1	130.2	17,900
Post Fabrication	1.1	226.8	104.6	1.1	226.8	104.6
Total kWh	212.9	230.6	1018.7	1891.2	357.1	18,005

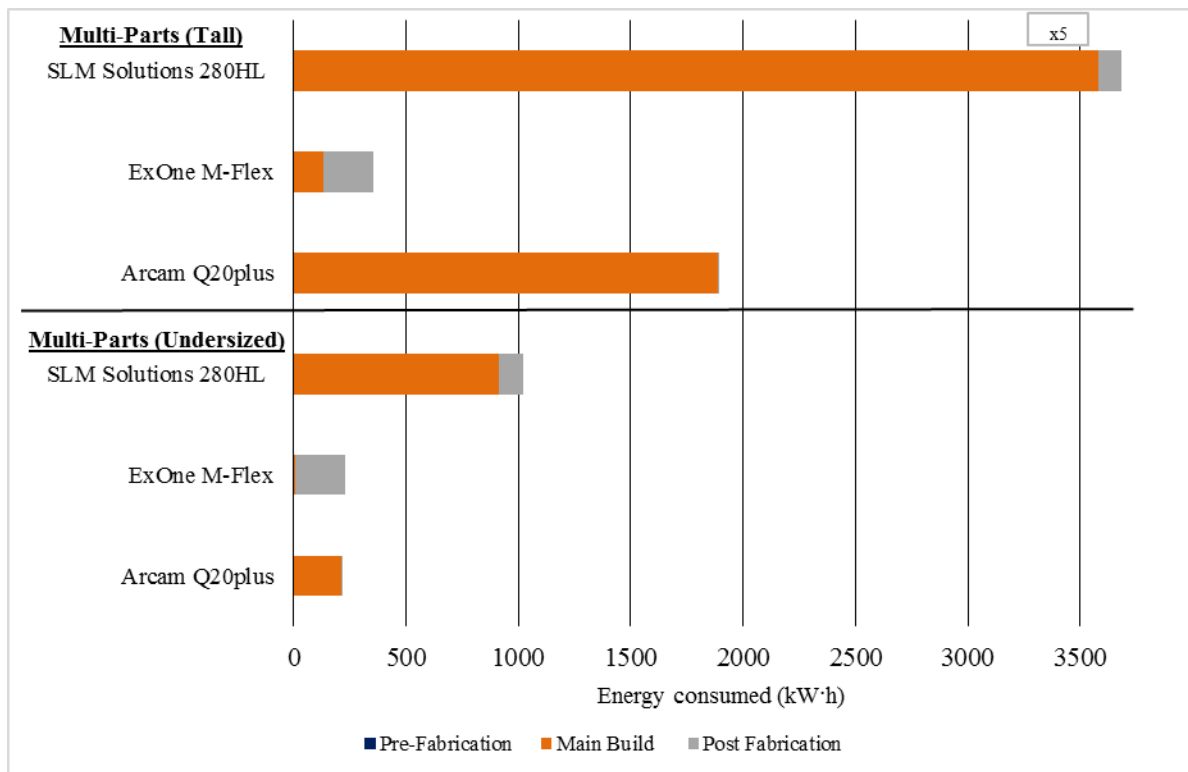
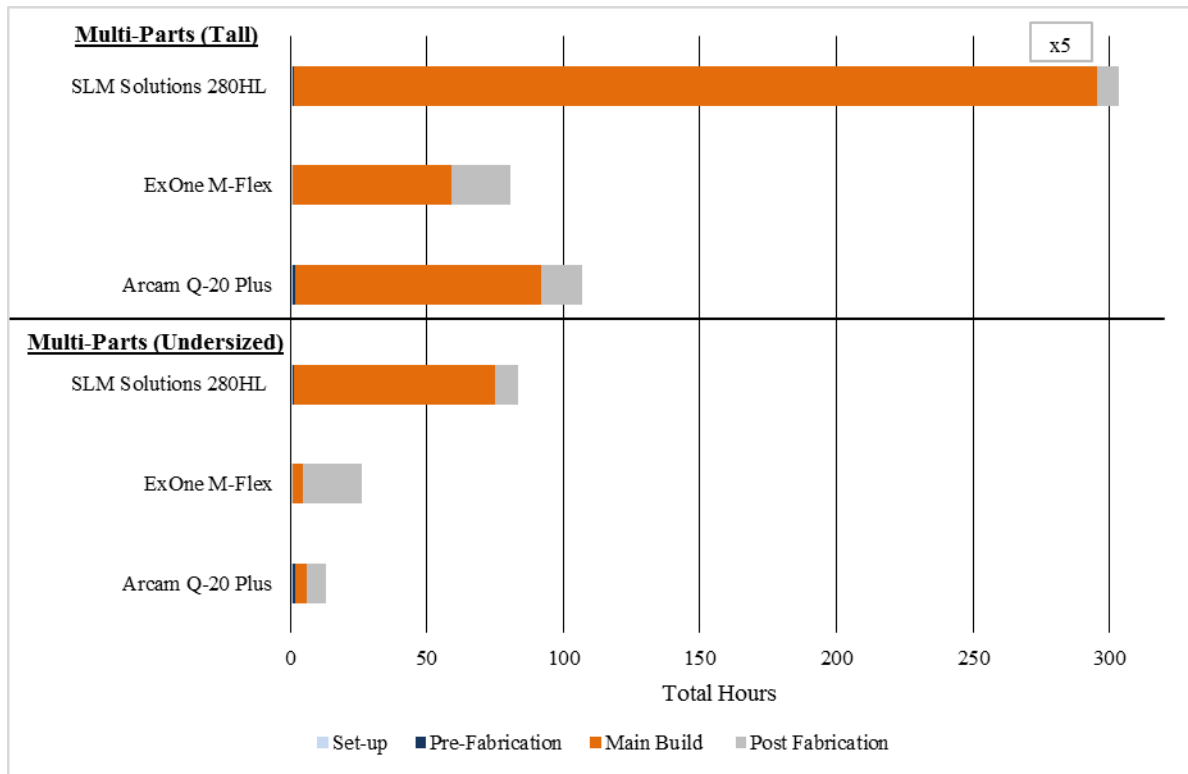


Figure 14. Fabrication time (hours) and energy comparison (kilowatt hour for multi-part case study 3&4

4.4 Chapter Conclusion

To consider the implantation of an AM system in a production environment, the previous cost and time variables mentioned must be accounted into a model. A full cost model may include system value, required consumables, maintenance/ service contracts cost, software license. However, an actual USD value for the energy consumption based on a definite system run should be performed. Based on the fabrication time/ energy consumption research in this chapter each system had certain beneficial scenarios. For example, an SLM system may be the ideal choice in an environment targeting production of customized components. Binder jetting may be considered as the more viable technology when fabricating large quantities of components. Recalling the discussion of section 4.3, EBM is an efficient technology for the undersized part but binder jetting consumed the least amount of energy in large volume builds. Again, many variables can dictate the most adequate technology to be used for the ideal setting, such and the first initial investment.

The following chapters will detail the methodology and results obtained to test the mechanical properties as well and fracture mechanics of components fabricated using all three technologies in an attempt to further support the decision-making process when acquiring AM capacity, based on what technology best fits consumer given application. Each technology can be represented to have their own advantages; however, this research is conducted to define as many variables that may be presented by each technology to categorize each technology's attributes.

Chapter 5: Characterization of Inconel Alloy 625 Fabrication using Powder Bed-based AM Technologies

This chapter presents the characterization results of Inconel 625 components produced using each of the three powder-bed based technologies, providing an added metric for comparing such processes. The characterization study includes microstructure and mechanical properties (ultimate tensile strength, % elongation, yield strength, modulus of elasticity, and hardness). The goal was to fabricate Inconel alloy 625 samples using binder jetting, SLM, and EBM, while keeping the traditional attributes comparable to wrought and forged Inconel 625, determined by ASTM standard F3056-14 [45]. Characterization was first done to the precursor powder material, and continued to microstructure and mechanical properties after fabrication was complete. Two distinct build orientations were investigated to determine its effect on the performance of the samples fabricated by each technology.

The two orientations used are as follows: (1) horizontal or in the X orientation and (2) vertical in the Z orientation. Build orientation was labeled to correspond to ASTM standard terminology for AM coordinate system and test methodologies [7]. A total of 12 cylindrical samples were fabricated using each technology; six in the Z orientation and six in the X orientation (general build setup is represented on Figure 15). Samples were tested for density measurements as fabricated, then 3 samples of each build orientation were post-fabricated treated with a process known as hot isostatic processing (HIP). HIPing is performed on the fabricated samples to remove possible internal porosity and collapse internal voids that may diminish mechanical properties of the fabricated samples [46]. HIPing is also used to create more uniform grain structure and reduce statistical spread in material properties [46]. The HIPing cycle used for this material was 3 hours at 1162.78°C (+/- 3.5°C) in 101.697 MPa (+/- 1.72 MPa). Specimens of EBM were fabricated using an Arcam A2 system with in-house developed processing parameters. SLM parts were fabricated with an SLM Solutions 125HL using stock parameters that provided by SLM Solutions. For both EBM and SLM, fabrication was performed at the W.M. Keck Center for 3D Innovation at UTEP. Binder jetting specimens were fabricated by the ExOne Company using a polymer based

binder to produce a green product. Green body samples were sintered at a maximum temperature of 1310°C (soaked for 2 hrs) and taking a total of 16 hours for completion. The full sintering cycle took 16 hours to complete. It is possible that the build parameters used for the fabrication of EBM and binder jetting specimens are not optimized with that fact that they are parameters under developments.

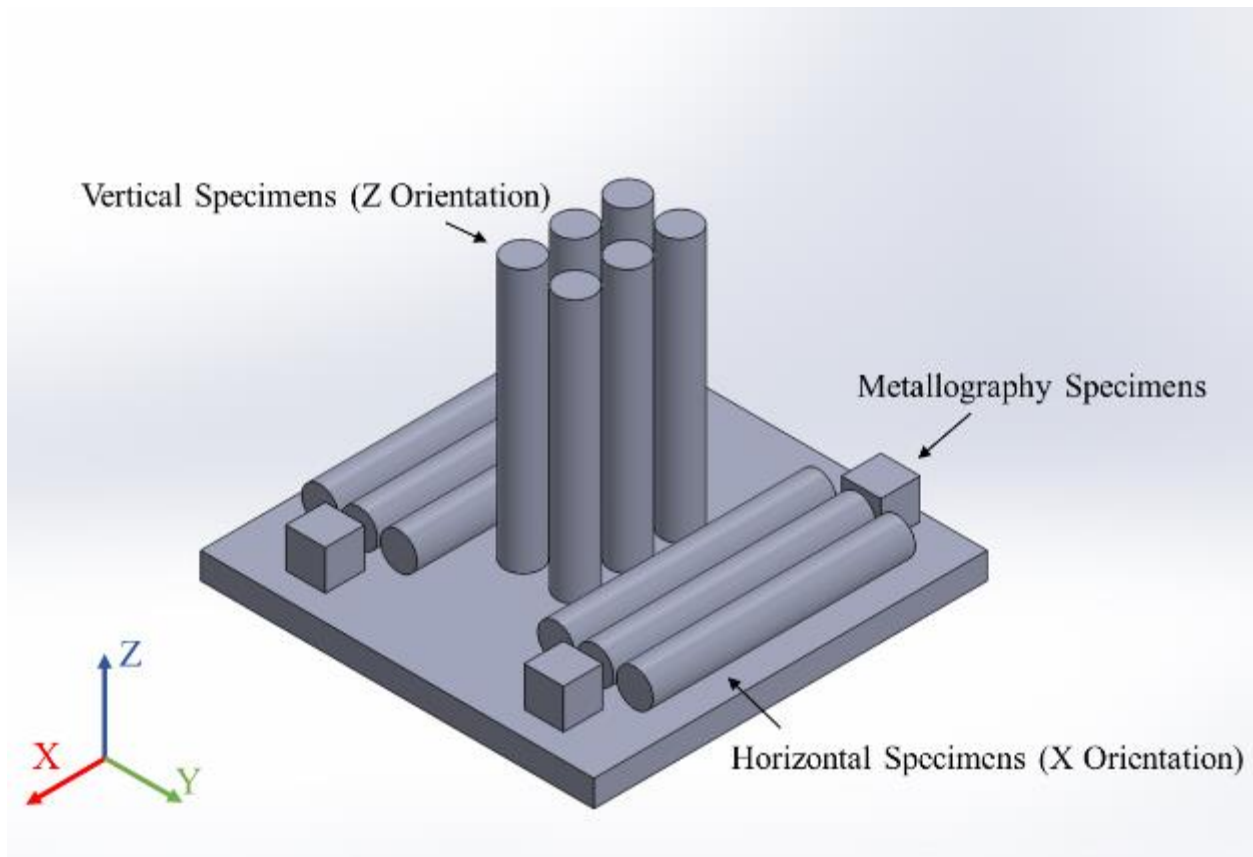


Figure 15. Isometric view of build setup used for fabrication using the powder bed-based AM technologies

5.1 Powder Analysis

Powder used for each technology were obtained from various manufacturers. Powder used for EBM fabrication was purchased from Carpenter Powder Products (Product #2221103-0007, Bridgeville, PA). The powder for SLM was purchased directly from SLM Solutions Company (Product #2015000568, Lübeck, Germany). Finally, as previously noted, ExOne produced the testing specimens in their North Huntingdon, PA facility where the powder was also received from an unknown supplier. Powder morphology, particle size and chemical composition were evaluated using a Hitachi TM 1000 Tabletop Scanning Electron Microscope (Tokyo, Japan) to determine powder characteristics prior to fabrication.

Images of powder's morphology is shown in Figure 16 (A) for binder jetting, (B) for EBM, and (C) for SLM, in the as-received condition. From the SEM images obtained, powder used for the binder jetting process shows the smallest particle size, with an average particle size of 11 μm , followed by SLM with an average particle size of 16 μm , then EBM with the largest particle size of the three technologies with 23 μm as the average particle size. The morphology of the powder for EBM and SLM appears spherical in shape with some splat caps on certain powders accompanied by some satellites, related to the gas atomization production process used for the making of such powders. The shape of the powder for binder jetting exhibits a combination of spherical, elongated, and irregular morphology, a common feature with fine powders, resulting in an increase of satellites formation [47].

The ASTM Standard B213-13 was followed to determine the flow rate of the powder. The standard requires that 50 grams of powder flow through a Hall flowmeter funnel (ACuPowder International, USA). In this technique, the material is first weighed, then placed inside of the funnel with a calibrated orifice of 2.54 mm while covering the outlet. The obstruction is then removed allowing the powder to flow, and the time required to empty the funnel this recorded. A slight tap is allowed to start the flow of powder onto the outer surface of the funnel. [48]. Results for the powder flow properties are shown on Table 3 comparing the three powders used. A more flowable

powder is desired for powder bed-based technologies for efficient packing of the powder bed that can lead to reduced porosity of the final construct [49].

The next aspect of powder analysis includes the measurement of the powders' apparent density. The ASTM standard B212-09 was followed to measure the apparent density. In this process, powder is again allowed to flow through the Hall Flow meter funnel and captured into a brass cup with a calibrated volume of 25cm³. The powder filled cup is then leveled, removing the excess powder and the weight of the powder is calculated by subtracting the weight of the empty cup. The apparent density is then calculated as the mass of the powder divided by the volume of the density cup, reported to the nearest 0.01g/cm³. Those values are also summarized on Table 3.

The final powder metric that was characterized was chemical composition. Through this analysis, variations in the powder chemical composition before their use were identified. The results of the chemical composition test for all three powders is provided in Table 4, indicating that there were no substantial differences in chemistry for the three materials analyzed.

Table 3. Powder analysis of as-received powders for each technology, including average particle size, flow rate and apparent density

Powder Analysis						
Tech.	Mass (g)	AD (g/cc)	Solid density (g/cc)	% Density change	Flow rate x Avg. (s/50g)	Avg. Particle size
Binder Jetting	97.56	3.9	8.44	46.16	18.56	11 µm
EBM	108.82	4.35	8.44	51.57	130.69	23 µm
SLM	82.78	3.31	8.44	39.23	204.3	16 µm

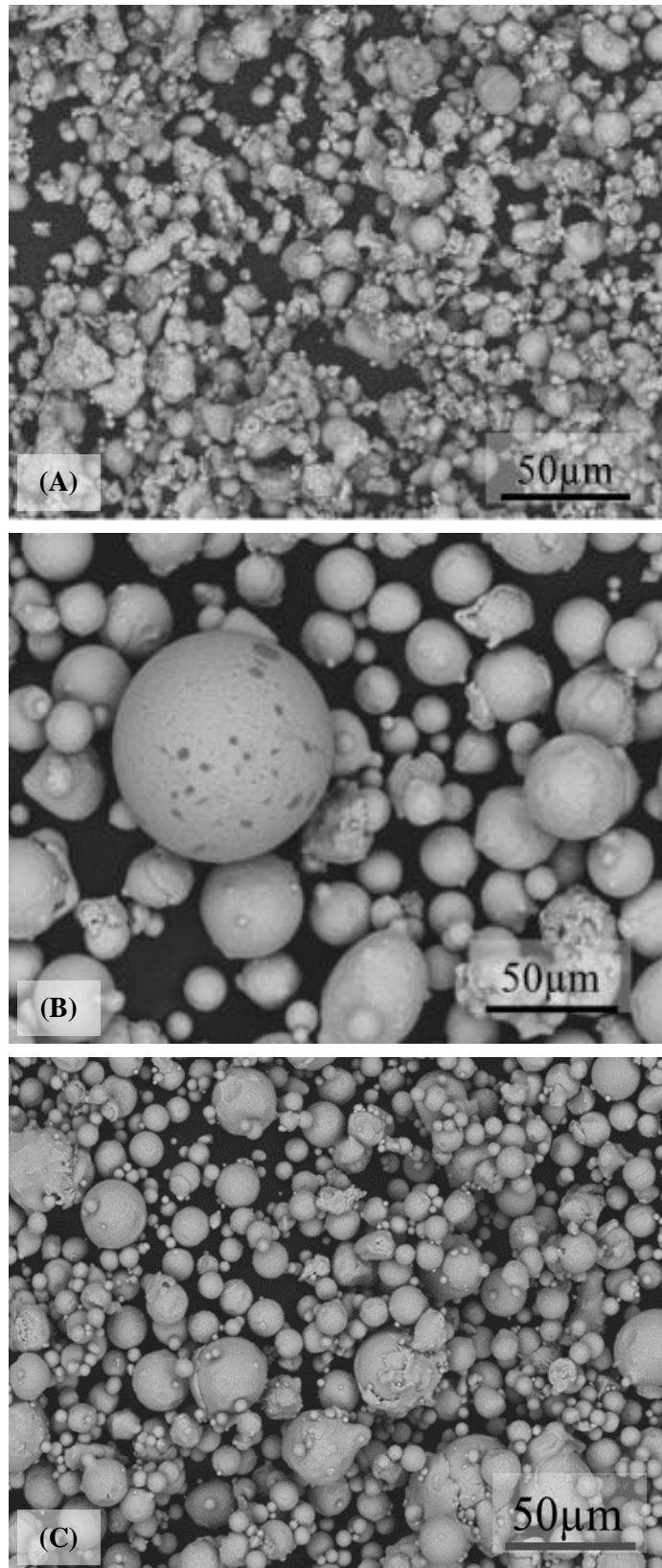


Figure 16. SEM Images of precursor powder used for the fabrication using (A) binder jetting, (B) EBM, and (C) SLM.

Table 4. Chemical Composition of as-received powder for each technology

Element (wt %)	Ni	Cr	Mo	Nb	Fe	Mn	Si
Binder Jetting	60.12	22.84	9.16	4.15	2.9	0.42	0.32
EBM	61.3	21.01	9.8	4.1	3.0	0.33	0.4
SLM	61.55	21.25	9.55	4.05	2.8	0.5	0.2
ASTM Requirements	Balance	20-23	8-10	3.15 - 4.15	5.0 (max)	0.5 (max)	0.5 (max)

5.2 Built Components Density Measurements

Apparent density measurements of fabricated samples, both as-fabricated and HIPed, were calculated with the use of ASTM standard B311-13. Figure 17 depicts equipment setup to measure component density. The standard requires for weight measurements to be made by weighing the samples of interest in air and in water separately. As such, this method is recognized as the Archimedes method. The apparent density of parts was calculated by using the following formula:

$$D = (A \times E) / (A - F)$$

The variables in the formula are defined as follows: A is the mass of the test specimen in air, F is the mass of the test specimen immersed in water and E as the density of water at the working

temperature. Since the test was conducted at 24°C, the value of the E used was 0.9975 g/cm³ as indicated by the ASTM standard [50]. The percent relative density (%RD) for parts was calculated as the quotient of the obtained density value over the density for Inconel 625 of 8.44g/cm³ [30]. Reported values were the average of three different measurements for each sample.

The average density values for the as-fabricated samples were 96.51% for binder jetting, 99.9% for EBM, and 99.9% for SLM. Post HIPing, both EBM and SLM average apparent density values measured similarly as before with an average of 99.9%. In the case of binder jetting, a 2% increase was observed from the previous measurement amounting to 98.33%.

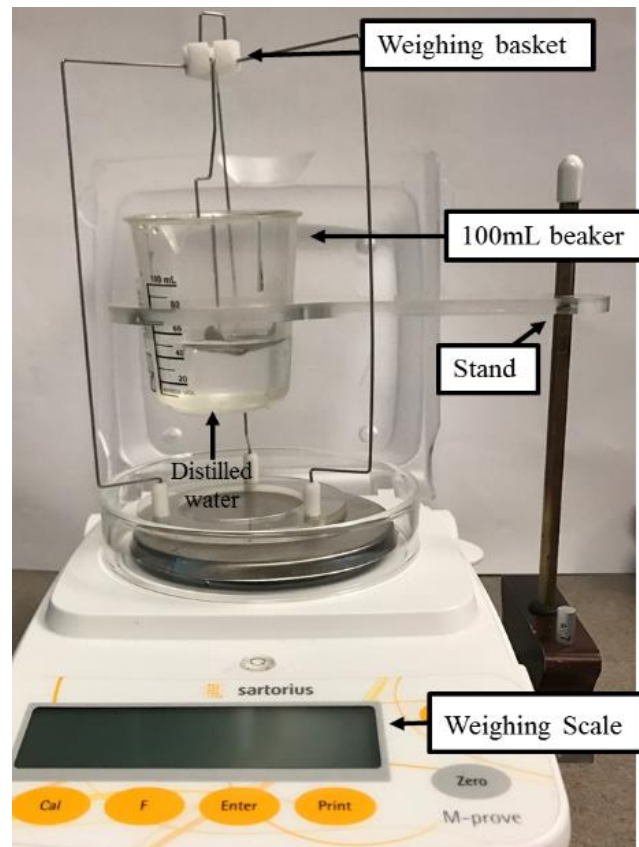


Figure 17. Measurement kit used to obtain apparent densities of samples.

5.3 Microstructure

Microstructure analysis provides an insight on how the fabrication process may affect the microstructural and mechanical properties, and hence the final product performance. Past research studies have discovered that AM processes observe anisotropic properties (properties differing in XY and XZ/YZ planes), an effect that is related to the anisotropy of microstructure such as the observed preferential growth of grains in the build direction in EBM. To investigate these effects, this study performed metallography of built specimens to observe characteristics on planes parallel and perpendicular to build direction [14] [51]. Specimens were prepared for metallographic analysis to determine grain structure and orientation differences between the fabrication processes following the ASTM E3 standard. Cubes measuring (15 mm) were fabricated using each technology and prepared for metallography analysis. The process of metallography included casted mounting of specimens using a self-curing resin epoxy from Koldmount (Product #ME-22P), grinding of the surface of interest in the specimen using SiC grit paper (Struers, Cleveland, OH, USA), and polishing with an alumina (Al_2O_3) mixture with the use of a Buehler Metaserv 25 Grind-Polisher (Lake Bluff, IL, USA). Upon completion of final alumina mixture ($0.5\mu\text{m}$) polishing treatment, the specimens were electro-etched to reveal sample's microstructure by applying a 5V for 7 seconds within a chromic acid bath by placing samples onto a Struers LetroPol-5 electrolytic system. Etched samples were examined under bright field optical microscopy using a Leica Reichert MEF4 A/M inverted metallographic system (Leica Microsystems, Wetzlar, Germany). Both as-fabricated and HIPed samples were examined to distinguish microstructural differences before and after this post-treatment.

5.3.1 As-Fabricated Microstructure

Referring to the optical images captured, the binder jetting samples have an appearance of equiaxed morphology grain shape (regardless of build direction) when compared to the fusion technologies. For these samples, a sizeable amount of porosity (dark voids) can be seen in microscopy images corresponding to the build direction (Figure 18A). The porosity was somehow

expected based on the density measurements of as-fabricated binder jetting samples. For EBM, the microstructure shows columnar grains that are parallel to the build direction (cross section) leading to a highly textured morphology (Figure 18B). In the opposite direction, or the top of the sample (perpendicular to the build direction) grains have a more uniform pattern. Similar effects have been documented previously on metals fabricated by EBM [52]. For instance, Murr *et al.* characterized Inconel alloys, such as 625 and 718, and described the directional growth of precipitate within the EBM melt zones [51]. These precipitates are formed in a columnar orientation parallel to the build direction, following the columnar grain and the low-angle grain boundaries, have been determined to be γ'' (bct) Ni_3Nb disk platelets coincident with Ni-Cr (fcc) $\{111\}$ planes [51]. From the images obtained in this work, the dark linear streaks visible in Figure 18B are the γ'' precipitates, all having a directional pattern with the microstructure (higher magnified microstructure seen in Figure 20). The columnar grain texture indicates that samples fabricated with EBM technology will experience anisotropic mechanical properties. Directional solidification fabrication methods, such as AM, can induce this effect of developing columnar microstructure ideal for turbine blade applications [53]. The microstructure of SLM produced Inconel 625 appears with an arch-shaped pattern parallel to the build direction (Figure 18C), and a linear pattern perpendicular to build direction. The linear pattern is a result from an equally raster scan parameter, that creates melt pool during fabrication process, and is a common feature for SLM fabricated samples that have not been post-fabrication treated [54]. The arch-shape microstructure is formed during the solidification of the metal molten pool, when the temperature gradient is the highest [55]. The radial inward flow of the melt pool caused during the melting of the metallic powder, and with Marangoni convection forces cause the flow of the melt pool to occur from a region of decreasing temperature [56], resulting in the arch-shape pattern after solidification and the microstructure seen in Figure 18C.

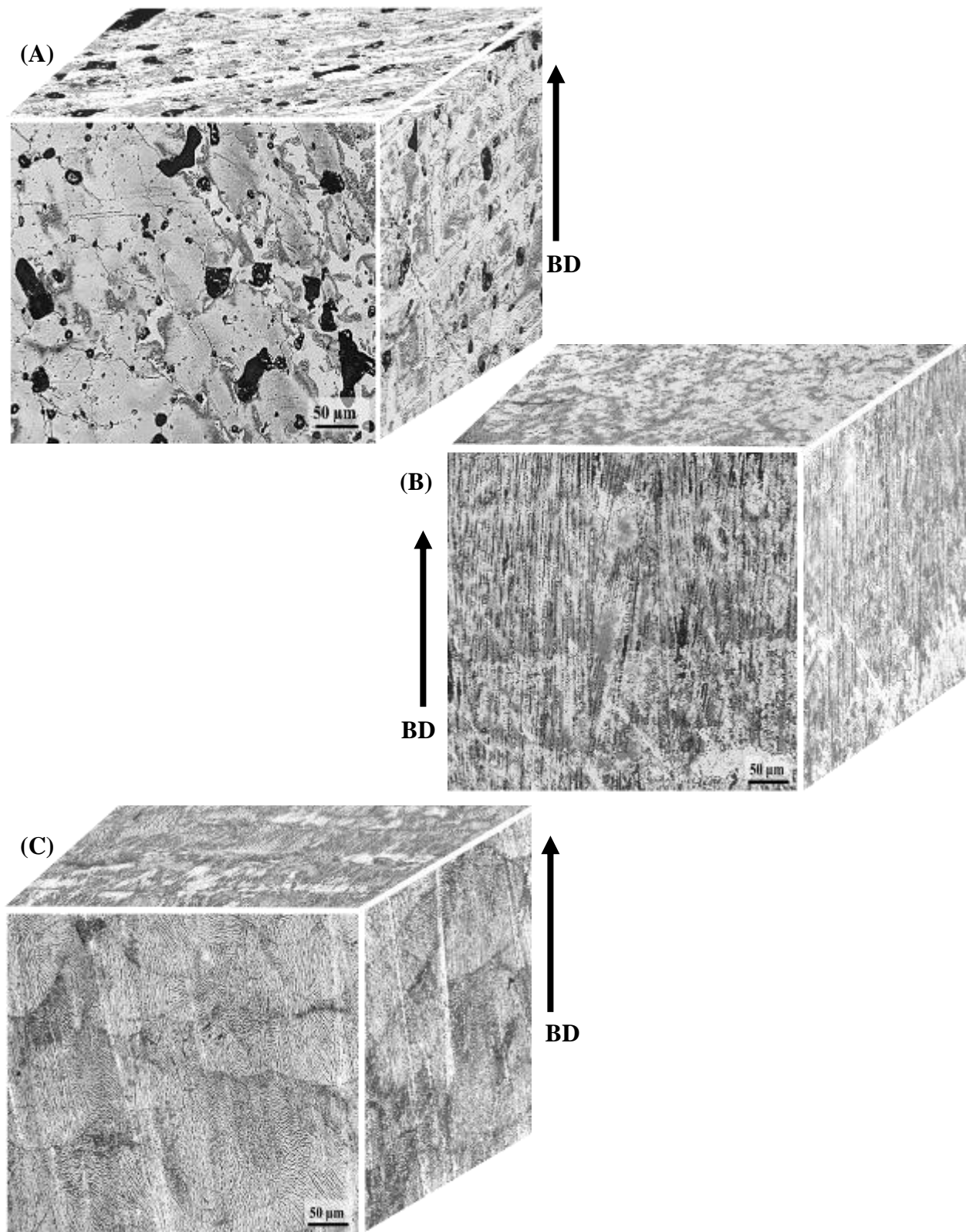


Figure 18. Microstructure cubes of as-fabricated Inconel alloy 625 manufactured by (a) binder jetting, (B) EBM, and (C) SLM. Build direction indicated by arrow

5.3.2 HIPed Microstructure

A considerable decrease in porosity for binder jetting samples can be observed in samples that were HIPed (Figure 19A), correspondingly to an increase in density. It is ideal that all internal porosity is removed due to eliminate weak points that may cause premature failure of the component. Binder jetting samples also reveal the formation of twins in the austenite grains, a characteristic of alloys with a low stacking-fault energy [57]. The formation of twins occurs when recrystallization cubic-closed packed austenitic metals is achieved at elevated temperatures [57], in this case during the sintering process. Binder jetting appeared with larger grains in comparison to the EBM and SLM, $\sim 57 \mu\text{m}$, measured using the line intercept method. In result, by applying the Hall-Petch relation, which states that a finer grain size will create a higher resistance in dislocation motion, lower mechanical properties may be the outcome. The HIPed EBM parts showed a negligible change in microstructure when compared to as-fabricated EBM samples (Figure 19B), still exhibiting columnar grain structure, measuring an average of $\sim 16 \mu\text{m}$ wide and $356 \mu\text{m}$ in length parallel to build direction very similar to as-fabricated samples. From the three technologies, SLM samples had the most notable alteration in microstructure between as-fabricated and HIPed samples. SLM HIPed samples now appear with a more obvious equiaxed, grain structure (Figure 19C), with an average diameter of $\sim 27 \mu\text{m}$ (measured using the line-intercept method), completely reducing the arch-shape pattern from the microstructure. Grains now resemble a grain structure where full recrystallization has occurred after the HIPing process with annealed twins present within the grains, common during the annealing of Inconel 625 once deformation of the material has taken place [58]. The altered microstructure now leads to a decrease in anisotropic mechanical properties, resulting in more ideal properties like those found in annealed Inconel 625 samples fabricated by traditional means. After all the microstructure was evaluated, it can be perceived that samples fabricated by binder jetting will experience pre-mature fractures due to remaining internal porosity, EBM samples will have anisotropic properties due to the build direction, and SLM samples should have the most similar properties to annealed Inconel 625 after a HIPing process.

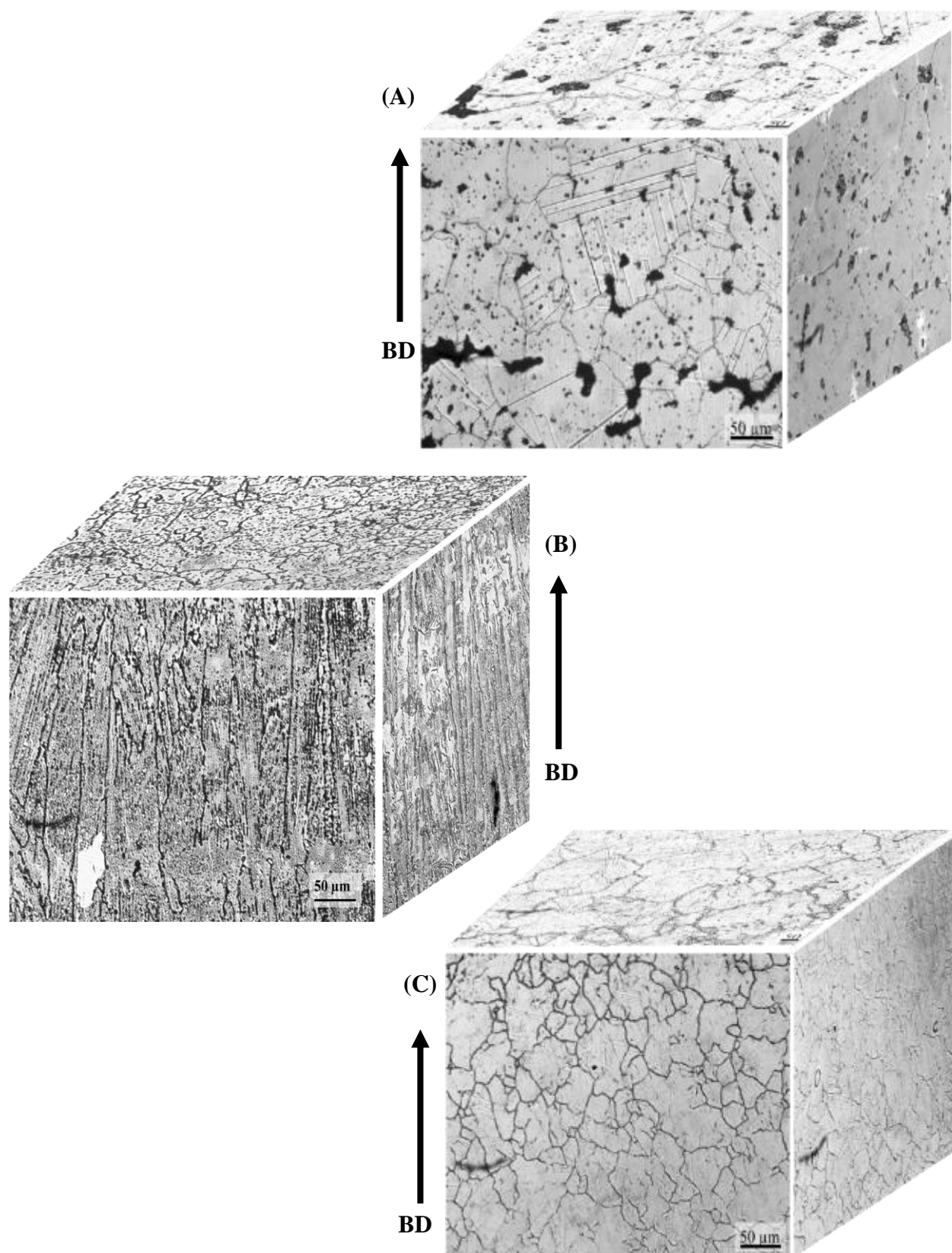


Figure 19. Microstructure cubes of HIPed treated Inconel alloy 625 manufactured by (a) binder jetting, (B) EBM, and (C) SLM. Build direction indicated by arrow

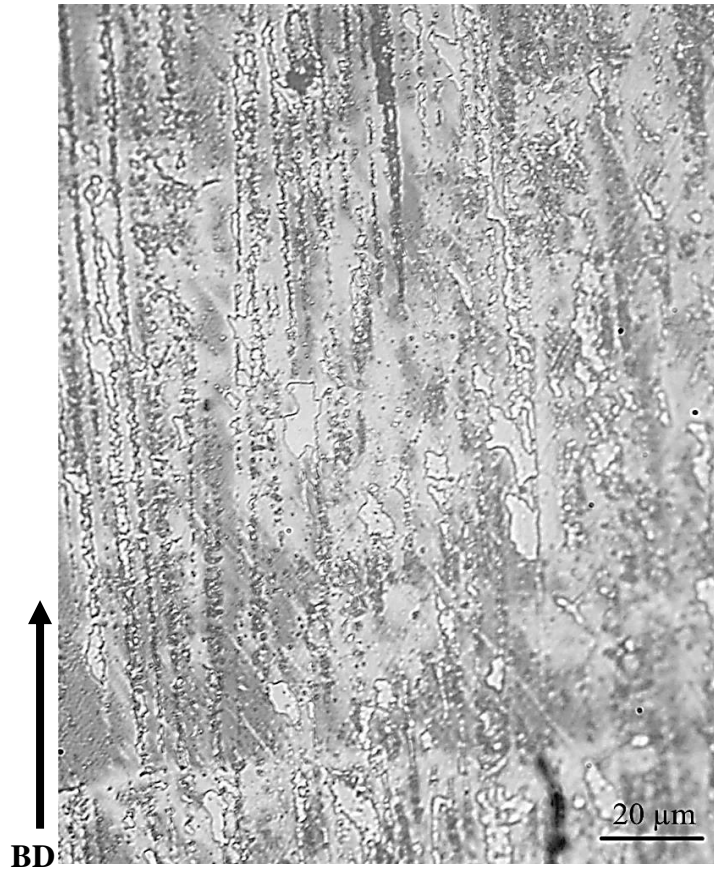


Figure 20. High magnification of Inconel 625 fabricated by EBM technology showing directional pattern of precipitates

5.4 Mechanical Properties

Tensile testing was performed on samples fabricated with all three technologies to determine mechanical properties. The tests were conducted in an MTS Landmark Servo-hydraulic test system (MTS Systems Corporation, USA). The design of specimens and the testing parameters were established based on ASTM standard E8/E8M-13a. Cylindrical rods were initially fabricated by each technology out of Inconel 625. The rods were then machined to follow E8M standards, to

create the testing specimens (Figure 21). During the test, the specimens were exposed to uniaxial load conditions, using a closed-loop control with a straining rate of 0.015 +/- 0.006 mm/mm/min pre-determined by the ASTM standard. Experiments were performed under required conditions at atmospheric with minimal temperature variation. Tensile load data and displacement was recorded by the testing system and that data was used to calculate stress and strain values. Engineering tensile stress (σ) was calculated by the following equation:

$$\sigma = \frac{P}{A}$$

Where P , or the load value provided by the operating system is divided by the measured cross-sectional area ($\sim 27.5 \text{ mm}^2$) of the testing specimen at the gauge section or A [59]. An extensometer was used during the testing (shown in Figure 22) recorded the displacement at the gauge length for each specimen. The value was used to calculate engineering strain (ϵ) with the equation:

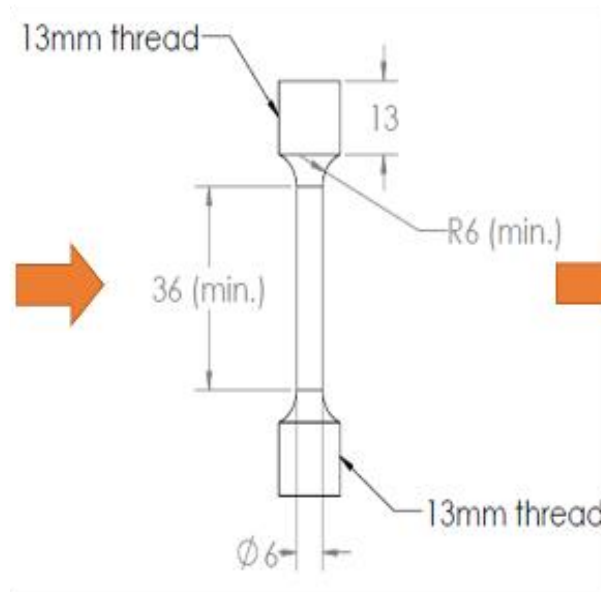
$$\epsilon = \frac{\Delta l}{l_o}$$

Where Δl is difference between the original length and final length, and l_o is the original gauge length [59], which in this case was defined as 30 mm. All testing results for all technologies are plotted in stress versus strain charts found in the Appendix (A3-A14). The data collected was used as an added metric for the analysis performed in this work. The data allowed to calculate tensile properties of the material that included ultimate tensile stress, elongation at break, yield strength, and modulus of elasticity.

Fabricated stock material



E8M Specimen Design



Machined Specimen



Figure 21. Process of tension specimens' preparation. Dimensions of design are in mm.

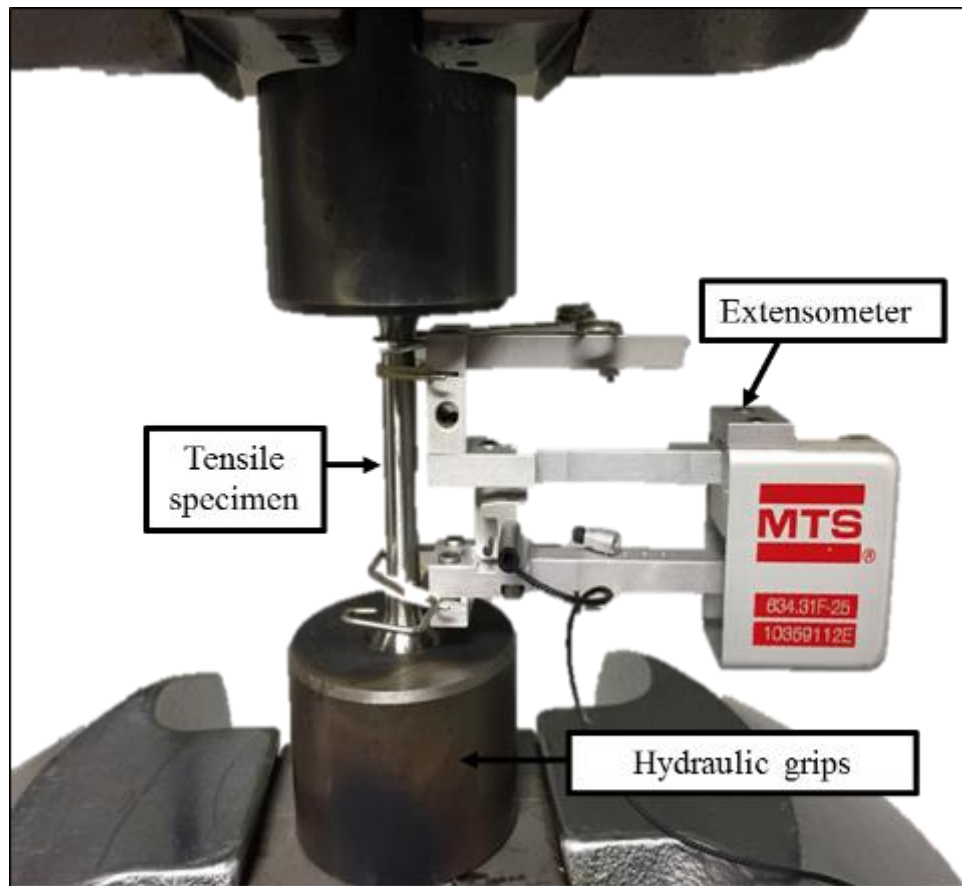


Figure 22. Tensile testing setup with specimen set to test.

Results of the three technologies were compared to ASTM standard F3056-14. This standard's intentions are to provide consumers with baseline requirements and to standardize minimum properties to be achieved for nickel alloys fabricated using AM powder bed fusion technology comparable to wrought and forged mechanical properties of Inconel 625 [45]. The minimum requirements were used as an outline for samples acceptance as well as a baseline metric

to quantify parts performance. Statistical analysis for the three technologies was performed with the use of a t-test on the tensile results. The t-test compares two sets of data results using of the following equation:

$$t = \frac{x_1 - x_2}{\sqrt{\frac{S_1}{n_1} + \frac{S_2}{n_2}}}$$

Where x are the mean values for data set 1 and 2, and S stands for the standard deviation for data set 1 and 2, respectively. Variable n is the number of values for each data set [60]. Based on t-test results is used to determine a p-value with the use of a t-distribution. P-value is used to determine statistical difference between two data populations where the null hypothesis is rejected when p is less than 0.05 (at a 95% confident level) [60]. By rejecting the null hypothesis, it concludes that a significant difference exists between the two compared data sets, on the contrary if the null hypothesis is accepted then the two compared technologies show no significant difference in the compared mechanical property [60]. Statistical analysis was only performed on samples that were HIPed, since as-fabricated samples appeared with a large variance within results.

5.4.1 Ultimate Tensile Strength

To calculate the ultimate tensile strength (UTS), the largest value of force (kN) that the specimen could withstand during the tensile test was divided by original cross-sectional area (mm²) of the specimen.

The results obtained for specimens built in the X orientation are described next. The SLM technique achieved the highest value of UTS at 1,027 MPa, followed by EBM at 806 MPa, and then binder jetting at 684 MPa. In a similar fashion, for the specimens built in the Z orientation, were SLM reached 892 MPa, EBM 522 MPa, and binder jetting 723MPa. These results are compared in Figure 23A. The results indicate that for all as-fabricated specimens, the average UTS

for both build directions met or exceeded the minimum requirements of 485MPa set by the ASTM standard.

The next set of data results compared are those of samples that were HIPed post fabrication. The results for these specimens that were fabricated in the X orientation after HIPing performed as follows: SLM with the highest average UTS of 906 MPa (± 28 MPa), followed by EBM with 849 MPa (± 28 MPa), and binder jetting displaying the least averaged value of 707 MPa (± 12 MPa). No significant difference between SLM and EBM specimens was observed, but a significant difference was noted between binder jetting samples and the other two technologies. Specimens fabricated in the Z orientation, displayed similar order with SLM the highest UTS (842 ± 15 MPa) trailed by EBM (723 ± 29 MPa) then binder jetting (702 ± 22 MPa) with only a 14 MPa non-significant difference between the two. SLM did however, demonstrate a significant difference when compared with the two other technologies. Again, all technologies were able to exceed exceeded the minimum requirements of 485MPa set by the ASTM standard, for both build orientations. Results for HIPed UTS values were recorded and compared in Figure 23B, with tables summarizing all averaged UTS values in Table 5.

Table 5. Average UTS values for as-fabricated and HIPed fabricated Inconel 625 by the powder bed-based technologies comparing both X and Z built orientation

UTS (MPa)	As-Fabricated		HIPed	
	X	Z	X	Z
Binder Jetting	684 \pm 45.68	723 \pm 30.18	707 \pm 12.25	709 \pm 22.22
EBM	806 \pm 29.01	522 \pm 205.34	849 \pm 36.98	723 \pm 29.33
SLM	1,027 \pm 135.51	892 \pm 4.58	906 \pm 28.33	842 \pm 14.48

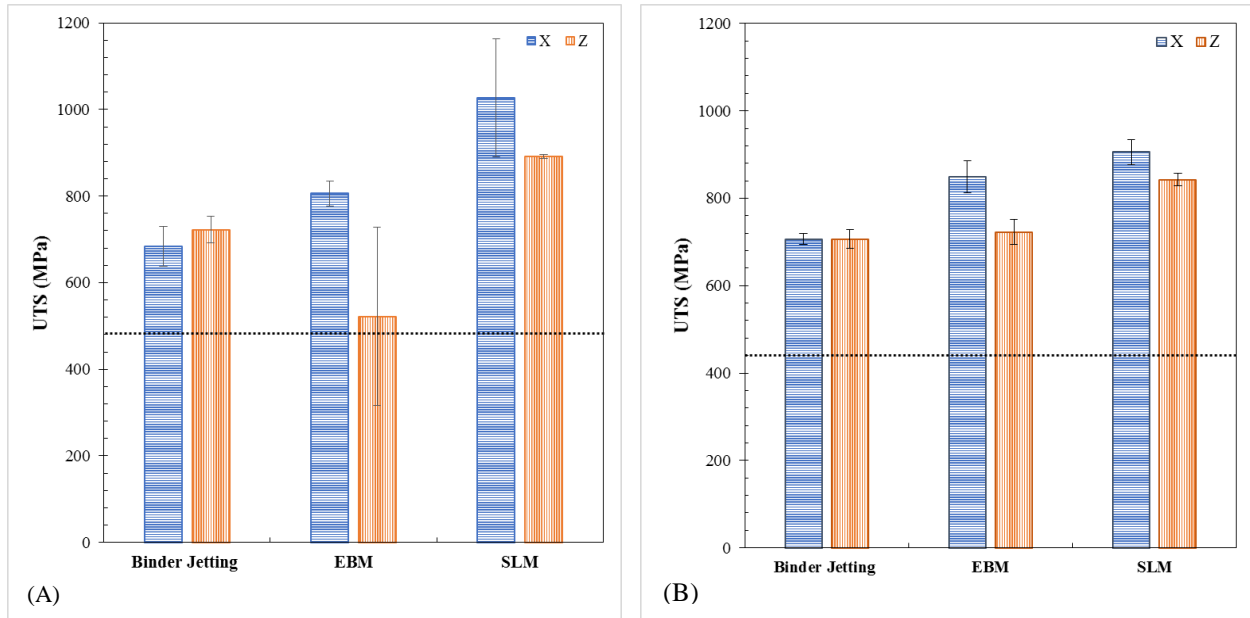


Figure 23. Average UTS for Inconel alloy 625 fabricated by powder bed-based AM technologies. (A) Results of as-fabricated samples and (B) HIPed samples. Dotted line indicates the minimum value required by ASTM standard F3056-14.

5.4.2 % Elongation (at Break)

The percent elongation is the maximum linear deflection the tested specimens endured before rupture and complete material separation. Values from tested specimens in as-fabricated form built in the X orientation were as follows: 53% ($\pm 2.5\%$) for binder jetting, 45% ($\pm 15\%$) for SLM, and 29% ($\pm 1.8\%$) for EBM. Concerning the Z orientation, the highest values obtained was for SLM at 39% ($\pm 1.3\%$), then binder jetting with 27% ($\pm 5.4\%$), and lastly EBM with 16% ($\pm 22\%$). Graphically represented of results is seen in Figure 24A.

For HIPed specimens, X orientation build specimens achieved the largest elongation. Those values reaching 62% ($\pm 2\%$) for SLM reaching 62.34%, binder jetting reaching 59% ($\pm 2\%$), and EBM reaching 44% ($\pm 5\%$). There was significant difference, at a 95% confidence level, between binder jetting and SLM, however a significant difference was noted between the other

tested technology (EBM). For specimens built in the Z orientation, the elongation value achieved by SLM was much higher in comparison to the two; with differences of ~29% EBM and binder. A clear significant difference was evident between SLM and the two other technologies but not amongst binder jetting and EBM. All results are plotted and compared on Figure 24B.

Looking at the overall results, all X orientated built specimens for all technologies in both states (as-fabricated and HIPed) met or exceeded the minimum ASTM standard of 30% elongation, excluding EBM as-fabricated. A summary of the results obtained for elongation is listed in Table 6, where the values that did not meet the minimum required are indicated in red. Nevertheless, Z orientated builds failed to meet such standard, with SLM being the only technology exceeding the minimum requirement. Figure 24 compares the averaged values for percent elongation (at break) of as-fabricated samples.

Table 6. Average % Elongation (at break) values for as-fabricated and HIPed fabricated Inconel 625 by the powder bed-based technologies comparing both X and Z built orientation. Red values indicate failure to meet ASTM F3056-14 minimum requirements.

% Elongation (at break)	As-Fabricated		HIPed	
	X	Z	X	Z
Binder Jetting	52.91± 2.47	27.02± 5.39	58.74± 2.14	26.92± 5.39
EBM	29.18± 1.79	15.9± 21.8	44.32± 4.95	27± 5.49
SLM	45.16± 14.6	39.47± 1.25	62.34± 1.99	56.30± 6.24

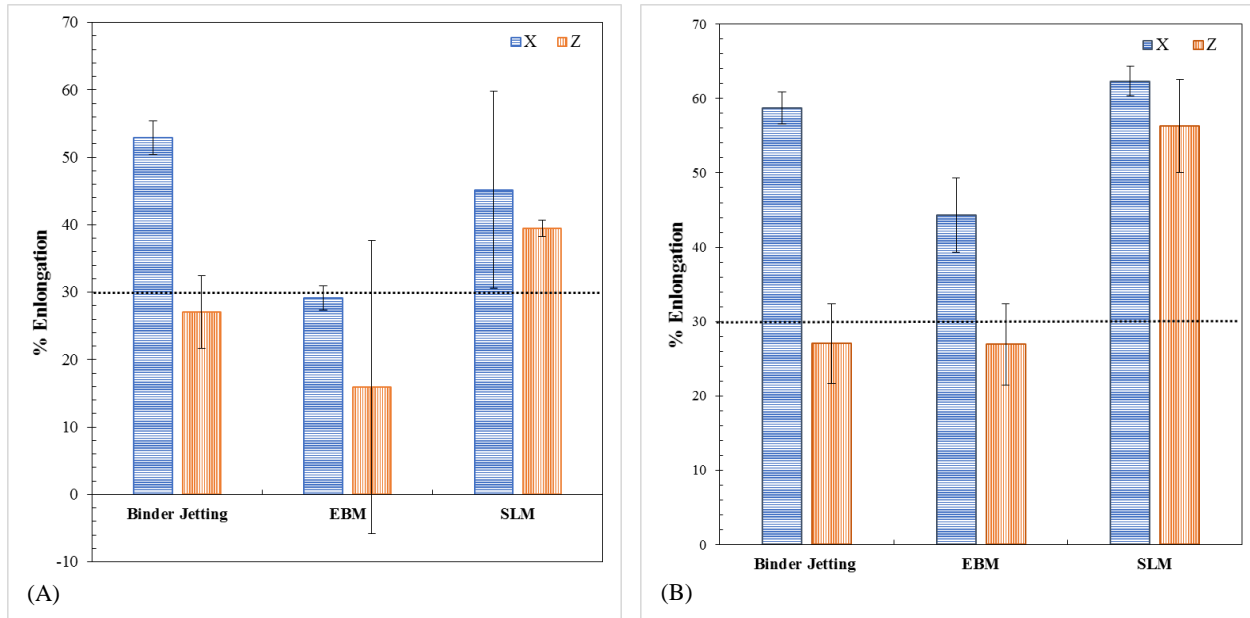


Figure 24. Average %Elongation (at break) for Inconel alloy 625 fabricated by powder bed-based AM technologies. (A) Results of as-fabricated samples and (B) HIPed samples. Dotted line indicates the minimum value required by ASTM standard F3056-14.

5.4.3 Yield Stress

The stress attained before plastic deformation occurs on the specimen [59], or yield strength (YS), was next mechanical property evaluated. YS was measured using the 0.2% offset method, identifying the stress obtained within the stress/strain curve for tensile test.

For as-fabricated specimens the results obtained are described next. For specimens built in the X orientation, average yield strength values were 684 MPa (± 230 MPa) for SLM, 390MPa (± 15 MPa) for EBM, and 330MPa (± 33 MPa) for binder jetting. For specimens fabricated in the Z orientation, the values were 654 MPa (± 11 MPa) for SLM, 341MPa (± 17 MPa) for EBM, and 302 MPa (± 2 MPa) for binder jetting. The results indicated the superior YS of SLM versus EBM and binder jetting. Graphical representation can be found on Figure 25A.

A similar analysis was done for specimens that were HIPed (Figure 25B) to obtain tensile strength properties. Specimens fabricated in the X orientation appeared with similar YS values with SLM surpassing EBM and binder jetting by only 29 MPa and 46 MPa, respectively. As statistical results indicate, no significant difference was present between SLM and EBM. On the other hand, binder jetting did show a significant difference from the other two powder bed fusion technologies. For specimens fabricated in the Z orientation, binder jetting displayed the highest YS (393 ± 24 MPa) and SLM the lowest (349 ± 6 MPa). No significant difference was seen between EBM and binder jetting, but was observed between SLM and other two technologies.

All technologies, in all tested conditions, met or exceeded the ASTM standard (275 MPa) required for yield stress, with results compared on Table 7.

Table 7. Average YS values for as-fabricated and HIPed fabricated Inconel 625 by the powder bed-based technologies comparing both X and Z built orientation.

Yield Stress (MPa)	As-Fabricated		HIPed	
	X	Z	X	Z
Binder Jetting	329.6 \pm 32.92	301.9 \pm 1.62	320.1 \pm 14.32	392.7 \pm 24.4
EBM	389.9 \pm 15.04	340.7 \pm 17.14	367.1 \pm 2.77	369.8 \pm 7.91
SLM	684.23 \pm 229.9	653.63 \pm 10.92	396.4 \pm 32.7	349.27 \pm 5.83

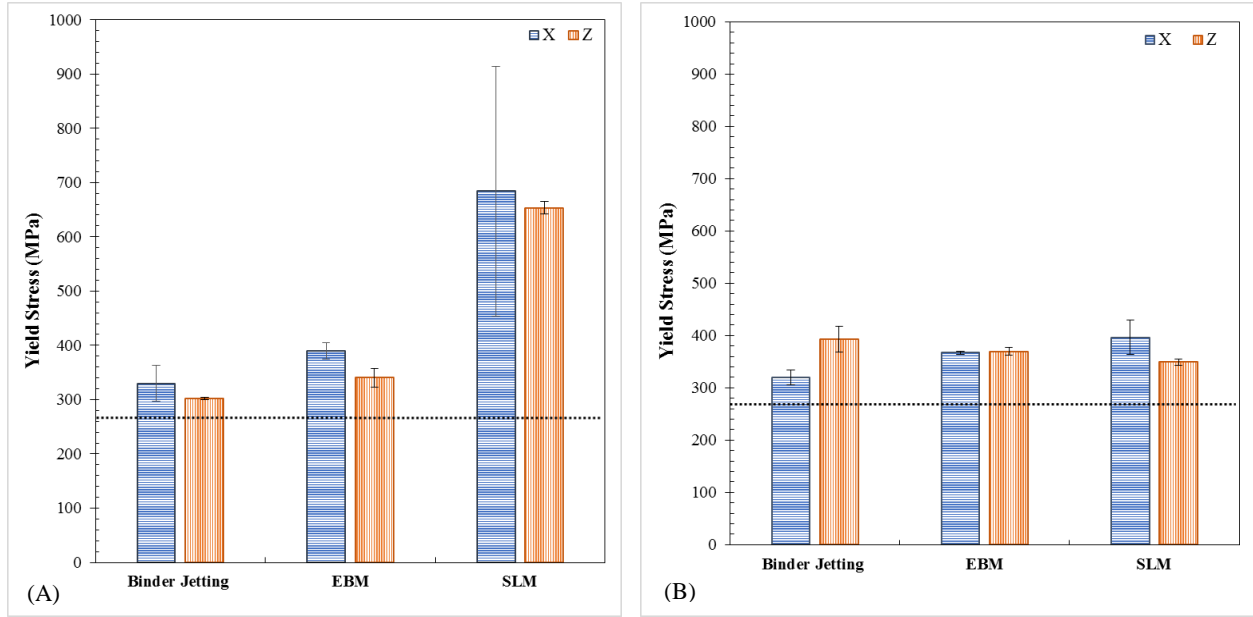


Figure 25. Average YS for Inconel alloy 625 fabricated by powder bed-based AM technologies. (A) Results of as-fabricated samples and (B) HIPed samples. Dotted line indicates the minimum value required by ASTM standard F3056-14.

5.4.4 Modulus of Elasticity

The final mechanical property evaluated is the modulus of elasticity or E . Modulus of elasticity is a material property that relates stress to strain. This relationship is expressed by Hooke's law [59] in the following equation:

$$\sigma = E\varepsilon$$

Where σ was defined as the engineering stress and ε is defined as the engineering strain for elastic deformation [59]. The modulus of elasticity (E), is the proportionality constant relating these two values, indicating the resistance to deformation or stiffness of the material. The value of E can be

obtained by calculating the slope from the linear portion of the stress-strain diagram. The values of E were calculated for specimens produced using all three technologies.

As-fabricated samples built in the X orientation had modulus of elasticity of 561 MPa (± 75 MPa) for SLM, 456 MPa (± 38 MPa) for EBM, and 414 MPa (± 27 MPa) for binder jetting. As-fabricated specimens built in the Z orientation had modulus of elasticity of 520 MPa (± 19 MPa) for SLM, 415 MPa (± 6 MPa) for EBM, and 425 MPa (± 12 MPa) for binder jetting. The results for modulus of elasticity of As-fabricated specimens are plotted on Figure 26A.

Similarly, the modulus of elasticity for specimens that were HIPed (Figure 26B) resulted in the following values: the greatest modulus of elasticity for specimens fabricated in the X orientation was seen in SLM (561 ± 36 MPa) while the lowest was given by EBM (484 ± 53 MPa). A similar order was noted in Z orientation fabricated samples. However, no significant difference between any of the tested samples in either orientation was seen at a 95% confidence level. Average values of E for the three technologies are compared on Table 8.

Table 8. Average E values for as-fabricated and HIPed fabricated Inconel 625 by the powder bed-based technologies comparing both X and Z built orientation.

E (MPa)	As-Fabricated		HIPed	
	X	Z	X	Z
Binder Jetting	414 \pm 27.2	425 \pm 12.4	523.5 \pm 47.0	506.2 \pm 51.1
EBM	456 \pm 37.7	415 \pm 5.7	483.6 \pm 52.8	459.6 \pm 36.4
SLM	561 \pm 74.8	520 \pm 19.3	561.1 \pm 36.4	539.7 \pm 58.6

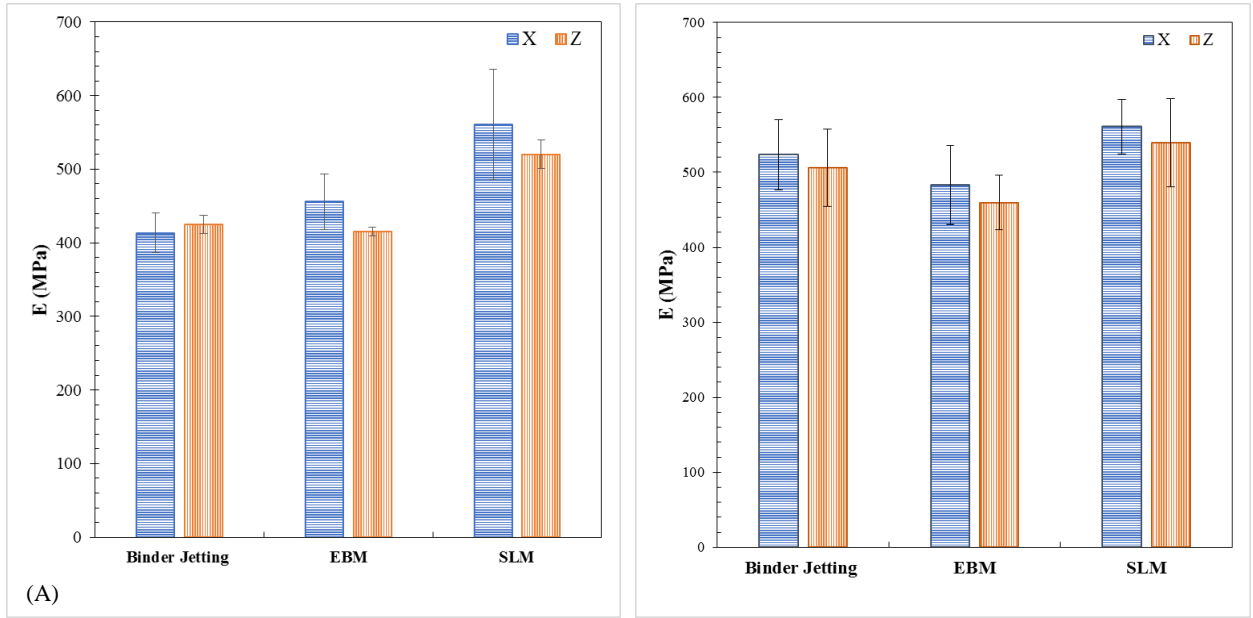


Figure 26. Average E for Inconel alloy 625 fabricated by powder bed-based AM technologies. (A) Results of as-fabricated samples and (B) HIPed samples

5.4.5 Hardness Results

Another mechanical property that was considered for this comparison is hardness. Hardness is the ability of a material to resist localized plastic deformation such as scratches or notches [59]. A Rockwell tests was performed on fabricated specimens by the three powder bed based technologies. The test involves the use of a 1/16 (diameter) diamond indenter to apply pressure into a polished surface under a prescribed load. The ASTM standard E-18 was followed to test for hardness of Inconel 625 fabricated specimens. Scale B was used for all measurements. A hardness value is determined based from two indenter depth values under minor and major loads. [59]. A Wilson Rockwell Series 2000 system (Wilson Instruments, USA) was used to perform all hardness tests. Five hardness measurements were taken parallel to the build direction and averaged to understand the hardness internally not superficial. As before, measurements were taken for as-fabricated and HIPed specimens.

Average values for as-fabricated sample were 75.28 HRB for SLM, 70.14 HRB for EBM, and 46.70 HRB for binder jetting with. After HIPing, hardness values for both EBM and SLM specimens were lower when compared to the as-fabricated condition averaging 63.92 HRB and 68.50 HRB respectively. In the case of binder jetting post-HIPing, an increase was observed averaging 65.12 HRB. Table 9 the average hardness values for the three technologies and two post-fabrication conditions.

Table 9. Rockwell hardness results for the three powder bed-based AM technologies using the B-scale

Rockwell Hardness (HRB)	Binder Jetting	EBM	SLM
As-Fab.	46.7 ± 1.94	70.14 ± 1.18	75.28 ± 2.27
HIPed	65.12 ± 0.33	68.5 ± 0.54	63.92 ± 0.89

5.5 Chapter Conclusion

The previous sections in this chapter have presented a comparative analysis of the microstructural and mechanical properties of parts produced by EBM, SLM, and binder jetting AM processes. From that analysis, the following conclusions can be drawn:

Binder jetting attained the lowest relative density of the three technologies, only reaching 96.5% dense parts as-fabricated and 98.3% after HIPing, compared to 99.9% reached by the powder bed fusion technologies. Metallographic analysis affirmed that EBM fabricated specimens obtained grains dependent on the build direction, in the form of a columnar grain structure in the build direction. Binder jetting appeared with sizeable pores and equiaxed grains, with lowest measured grains reaching $\sim 57 \mu\text{m}$ post HIPing. SLM specimen had a transformation of grain structure, altering from arc-shape melt pools present as-fabricated to a more homogenous grain structure after the performance of HIPing. Also, a refinement in microstructure ($\sim 53\%$ decrease in grain diameter compared to binder jetting) was achieved by the fabrication of Inconel 625 using SLM, having the most common features found in the annealed state of the alloy.

For the mechanical properties evaluated, all technologies were able to surpass the ASTM F3056-14 minimum requirement in ultimate tensile stress and yield stress. However, only SLM fabricated specimens exceeded the % elongation (at break) conditions stated by the standard, with EBM build parts (both build directions as-fabricated and Z orientation HIPed) as well as binder jetting (As-fabricated and HIPed both in the Z orientation) failing to meet minimum requirements, due to possible non-optimized build parameters .

A final concluding remark can be stated as the suitability of the three AM techniques used to produce parts that meet or exceed the mechanical properties outlined by the applicable ASTM standard, which were comparable to forgings and wrought Inconel 625 products. 625 [45].

As a continuation of the current analysis, the next chapter will determine the fracture mechanics and fracture modes of the tensile tested produced using the three technologies of interest.

Chapter 6: Fractography of Inconel 625 Fabricated Samples Fabricated by Powder Bed-Based Additive Manufacturing Technologies

Failure analysis of post-tensile tested specimens was carried out in a Hitachi Scanning Electron Microscope SU3500 (Hitachi, Japan). SEM images were taken of the fracture surface to categorize the failure mode. Examination of the fracture surface morphology is directly associated to the fracture mode of the material. Either ductile or brittle fracture modes can be identified. One as-fabricated and one HIPed fractured specimen built using each technology for both build orientations (X and Z orientation), were selected for analysis. The fracture surface images correlate with the mechanical properties attained and that were discussed in the previous chapter. A ductile fracture mode was expected for all specimens analyzed, based on the large amount of elongation during tensile testing.

6.1 Macro-Scale Evaluation

Nearly all specimen appeared with a ductile fracture feature referred to double-cup feature observed in macro-scale evaluation. Figure 27 Double cup fracture occurs when localized shear bands ahead of the crack tip lead to the separation of metal [61]. The continuation of the shear bands ahead of the crack tip, which will then lead to the two separated fragments to form an appearance of two cups. This double-cup feature is clear indicator of ductile fracture of metallic components.

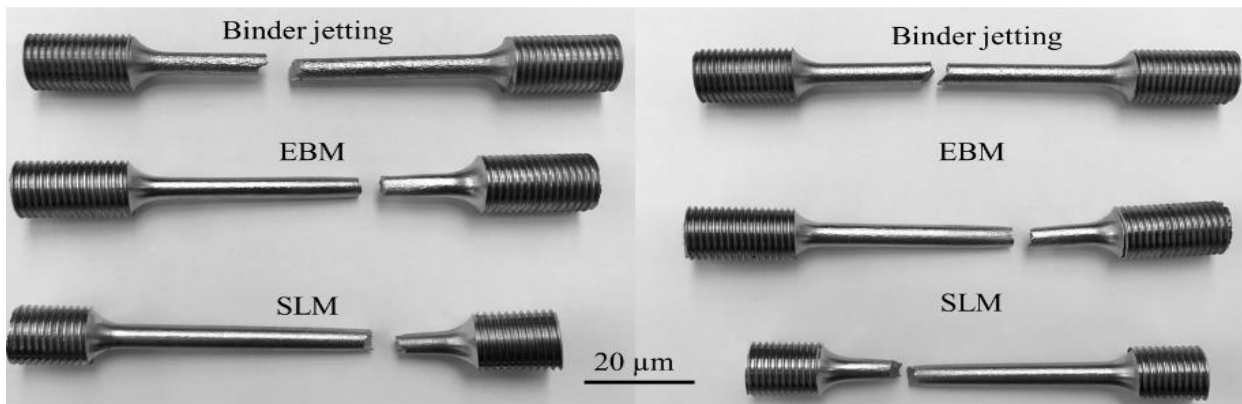


Figure 27. Macro-scale inspection of the three powder bed-based AM technologies fracture where double cup fractures are visible; (left) as-fabricated and (right) HIPed.

6.2 Fractography of As-Fabricated Specimens

After the tensile test, care was taken to preserve the fractured surface for observation. All samples show evidence of dimples on the fracture surface. Dimples found on the fracture surface are produced during the plastic flow of the matrix metal surrounding nucleation sites promoting the formation of micro-voids [62]. The presence of this dimples is an indication that ductile fracture transpired. Figure 28 A and B correspond to the SEM images for as-fabricated binder jetting specimens in the X and Z orientations respectively. A remarkable observation from these images is the presence of un-sintered powder particles within the micro-voids that are not ordinarily found on traditional manufactured metallic components. These particles have similar morphology to the precursor powder used for fabrication. A further investigation of the origin and chemical trace of these particles is discussed in section 6.4. Observations of as-fabricated binder jetting specimens indicated that a larger number of un-sintered particles are present on the fracture surface of the specimens built in the Z orientation suggesting reduced mechanical properties (i.e. % elongation, YS, and modulus of elasticity) when compared to specimens built on the X orientation. Furthermore, for these specimens, the fracture surface does not reveal the characteristic dimples that will indicate ductile fracture.

The next set of images discussed are for fracture surfaces of as-fabricated EBM samples. These images correspond to Figure 29 A and B where a noticeable pattern of dimples can be seen. Further observations reveal a distinctive pattern or texture on the fracture surface images of X oriented specimens (Figure 29A). The pattern of the horizontal build sample fracture surface that is predominant in comparison to that found on Figure 29B. In the past, similar observations have been made for metallic components mechanically processed that lead to alignment of phases and they have been referred to as “woody structures” [63]. This pattern is ordinary in metallic components that have been formerly mechanically processed and may result in alloy segregation stringers, leading to phases to alignment along a specific orientation, that may in return construct weak paths during deformation [63]. The origin of this characteristic texture resembling wood fibers is hypothesized on the microstructure of as-fabricated EBM specimens. As was previously

discussed, the microstructure of EBM built parts observes the formation of precipitates in a columnar orientation, parallel to the build direction, that were determined to be γ' (bct) Ni_3Nb disk platelets. The columnar precipitates seem to lead to the formation of the wood like structure being a path for voids to originated and led to segregation of phases, which may be reduced by modifying build parameters or HIPing cycle.

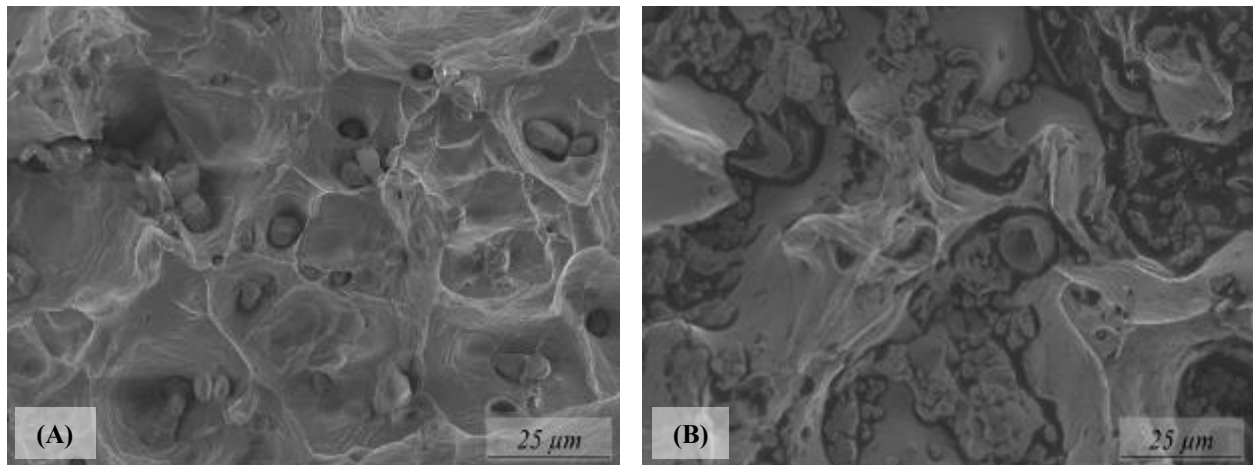


Figure 28. SEM images of fracture surfaces of failed binder jetting as-fabricated specimens. (A) Shows the fracture surface of EBM X orientation and (B) of Z orientation

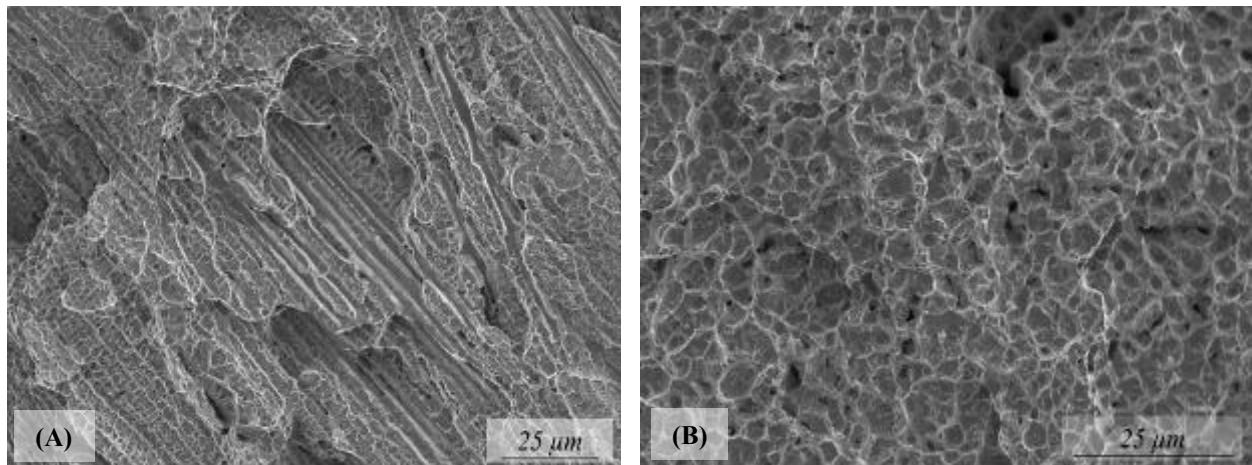


Figure 29. SEM images of fracture surfaces of failed EBM as-fabricated specimens. (A) Shows the fracture surface of SLM X orientation and (B) of Z orientation

A large variance in mechanical properties for Z oriented EBM specimens was observed. For this reason the fracture surface of an additional specimen (that failed prematurely during tensile testing) was observed under the SEM. Figure 30 displays the fracture surface of the premature failed specimen analyzed. In this case, evidence of un-sintered powder particles within the fracture surface provides an explanation for the early failure of this specimen leading to the large variance observed in mechanical properties for these set of specimens (EBM Z oriented), further supporting that non-optimum build parameters were used for the fabrication of tensile specimens.

The last images in Figure 31 (A and B) correspond to the fracture surface for as-fabricated SLM specimens in the X and Z orientations respectively. For both orientations, the regular dimple-like features are observed indicative of ductile failure mode.

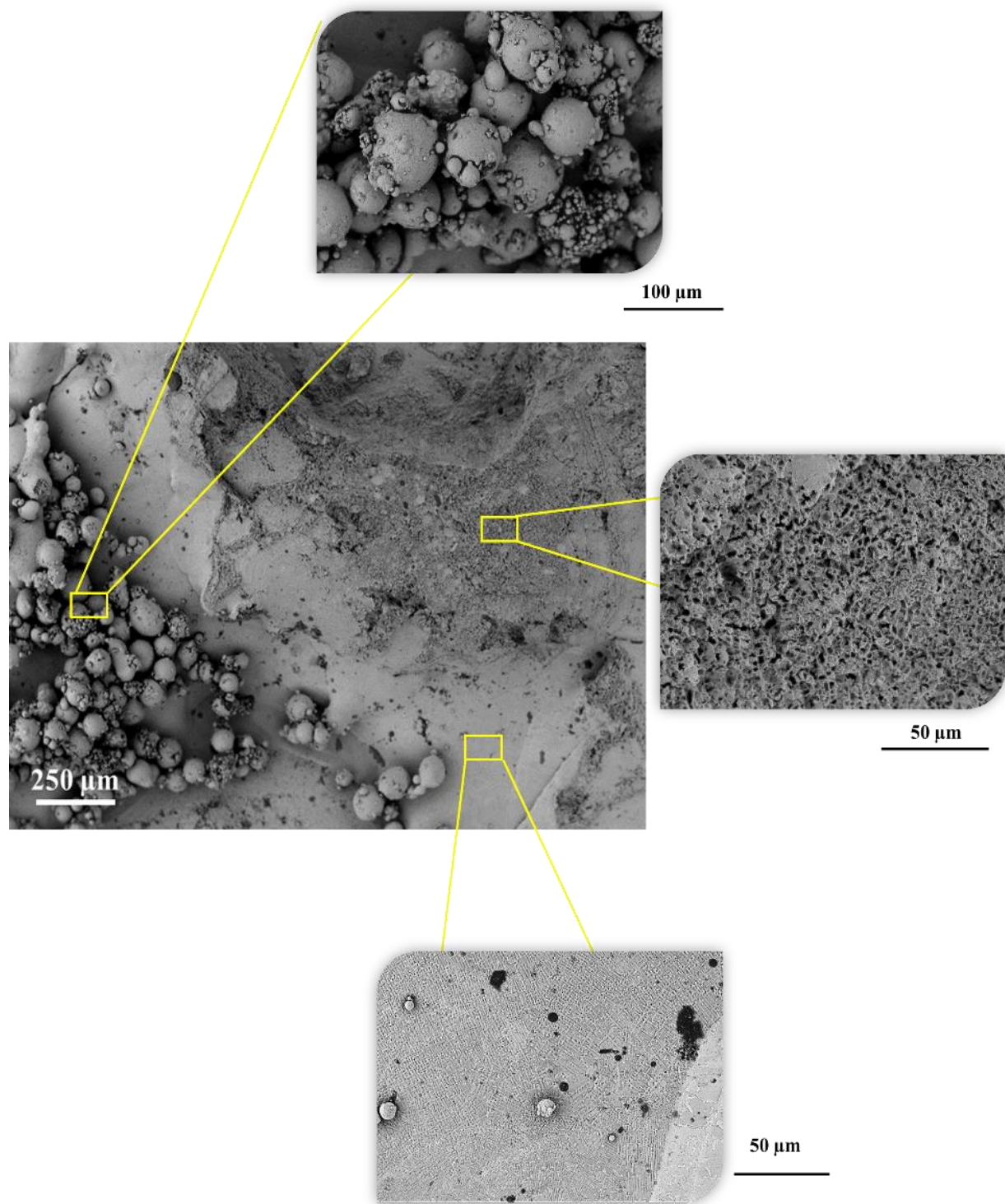


Figure 30. Example of a fracture surface of pre-mature as-fabricated EBM sample

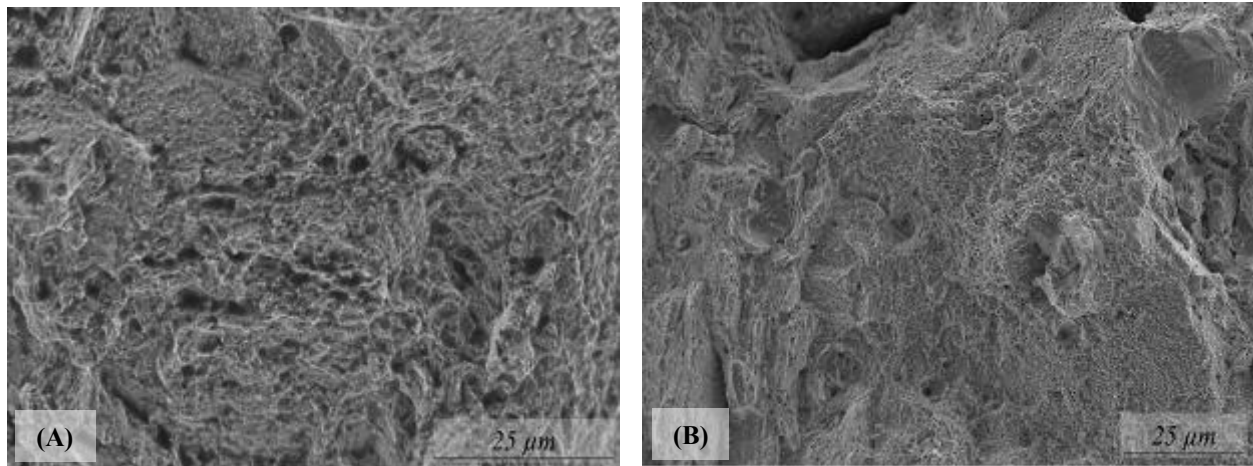


Figure 31. SEM images of fracture surfaces of failed SLM as-fabricated specimens. (A) Shows the fracture surface of binder jetting X orientation and (B) of Z orientation

6.3 Fractography of HIPed Specimens

Similar to those of as-fabricated specimens, all HIPed fracture surfaces showed the formation of dimples further specifying that the metallic specimens failed in a ductile manner. For HIPed specimens produced with binder jetting technology (Figure 32A and B), there was a larger number of particles and they seemed more organized as opposed to randomly distributed.

HIPed specimens fabricated by EBM in the Z orientation show common fracture features for ductile metals (Figure 33B), but X fabricated samples still appear to have the same “woody like” fracture surface (Figure 33A). The improvement in nearly all the mechanical properties for EBM samples fabricated in the X orientation rather than those built in the Z orientation may be related to the overall microstructure and how grains with higher strength were able to impede dislocation movement. In general, an increased number of grain boundaries and inclusions, counteract stress fields and enhance the mechanical properties.

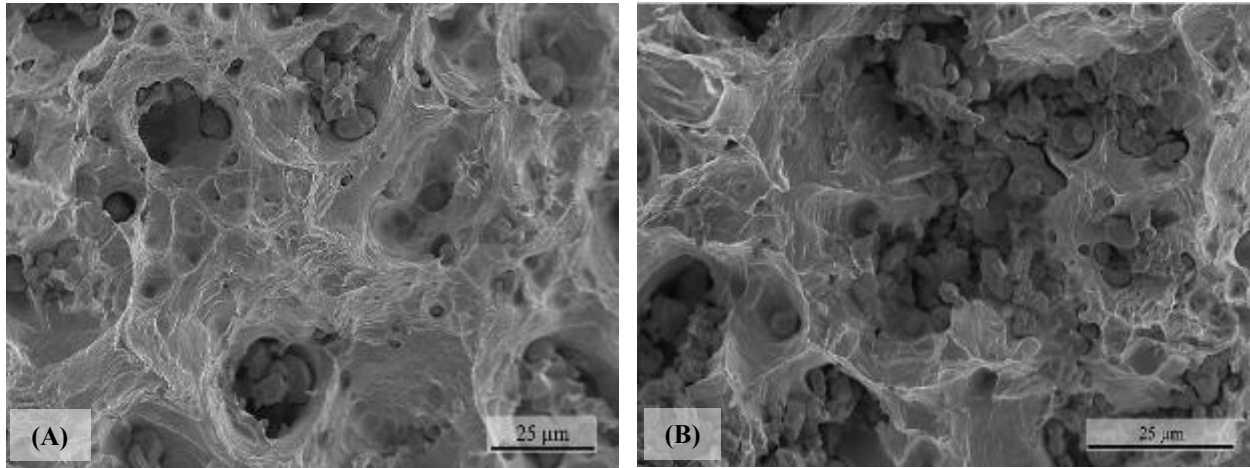


Figure 32. SEM images of fracture surfaces of failed binder jetting HIPed specimens. (A) Shows the fracture surface of binder jetting X orientation and (B) of Z orientation

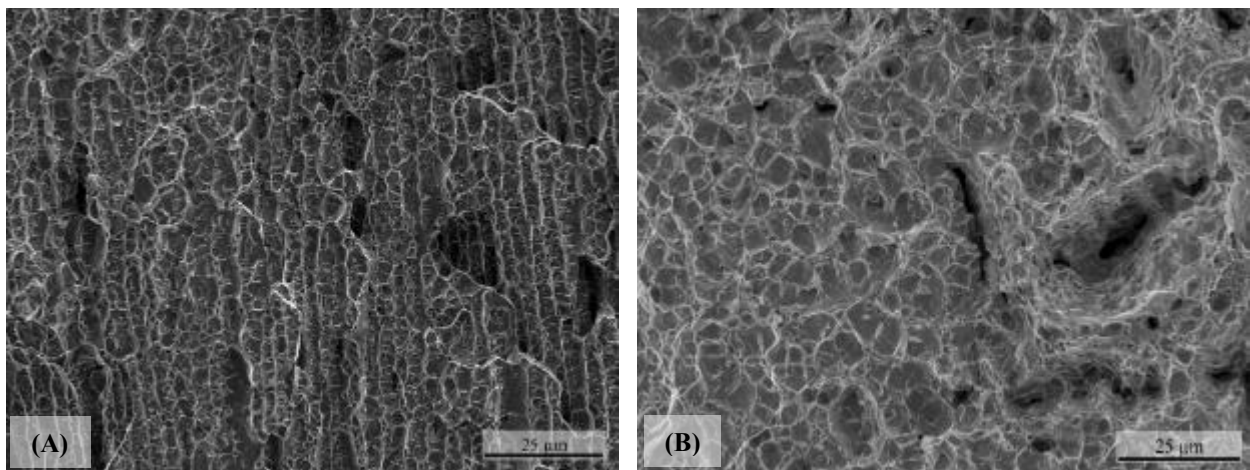


Figure 33. SEM images of fracture surfaces of failed EBM HIPed specimens. (A) Shows the fracture surface of EBM X orientation and (B) of Z orientation

The SLM fabricated HIPed samples, have the most homogenous shape of dimples present on both build orientations (Figure 34A, B). The formation of equiaxed dimples with spherical morphology, formed during plastic deformation occurs, when voids coalesce at inclusions during plastic deformation [64]. Figure 35 has an example of the fracture surface of SLM where voids began to coalesce at an inclusion point.

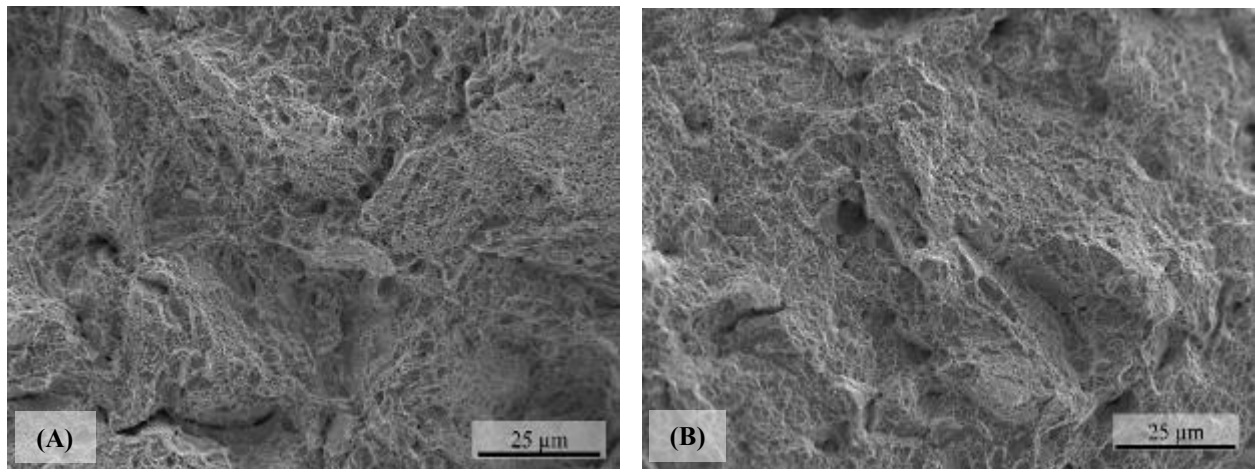


Figure 34. SEM images of fracture surfaces of failed SLM HIPed specimens. (A) Shows the fracture surface of SLM X orientation and (B) of Z orientation

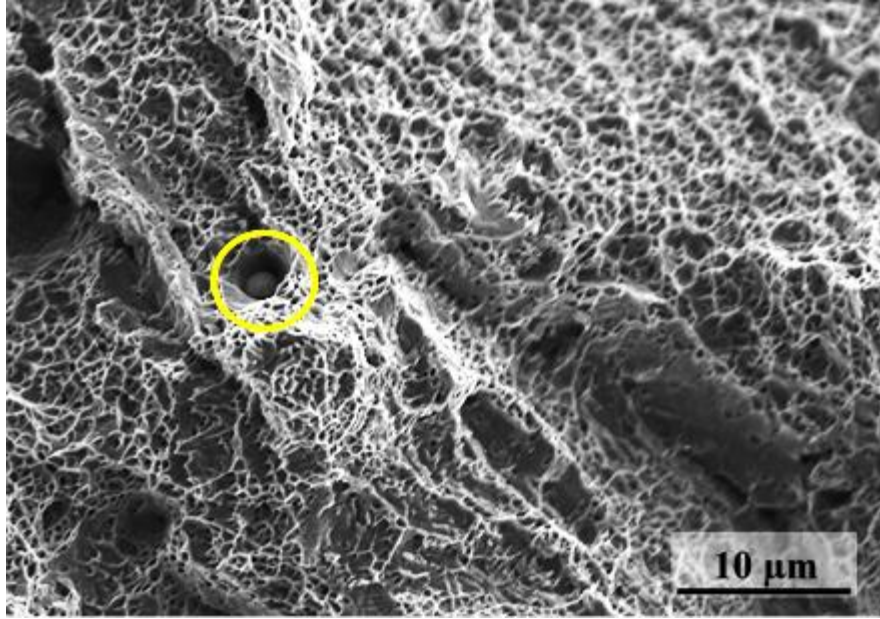


Figure 35. High magnification SEM image of SLM fracture surface with an example of an inclusion (precipitate) within the micro-voids.

6.4 Chemical Analysis

Due to the rare un-sintered particle inspected on the fracture surfaces of binder jetting fabricated samples, energy-dispersive X-ray spectroscopy (EDS) was performed on the particles to precisely investigate their chemical footprint. To perform the EDS analysis, the SEM used previously was furnished with an AZtecEnergy (Oxford Instruments, UK) including software to for analysis of elemental composition. This tool allowed to create maps of elemental distribution. The EDS maps show regions of the SEM image color coded based on the element or elements detected. EDS mapping assigns an individual color map to the identified elements, In the analysis performed, these colors were red, light green, blue, pink, orange and dark green for Cr, Nb, O, Mo, Fe and Ni, respectively. The images are then layered together revealing a colored map, seen on Figure 36. Based on the individual maps, the presence of oxygen is now identified, not found in the precursor

powder used for binder jetting fabrication. Oxygen (shown in blue on Figure 37) is observed, with relative high concentration, in the loose un-sintered particles located within the micro-voids as previously described. The chemical composition of the fracture surface also indicates that oxygen, at 6.35 wt%, was detected. All the other elements that were detected from the maps of the fracture surfaces are within normal values of the chemistry found in Inconel 625 (full chemical composition is listed in Table 10). This manifestation of oxygen being captured may arise during sintering when powder particles are exposure of high temperatures, as well as the vaporization of binder during such process.



Figure 36. Layered elemental mapping image of fracture surface for binder jetting Z-orientation build combining all elements present.

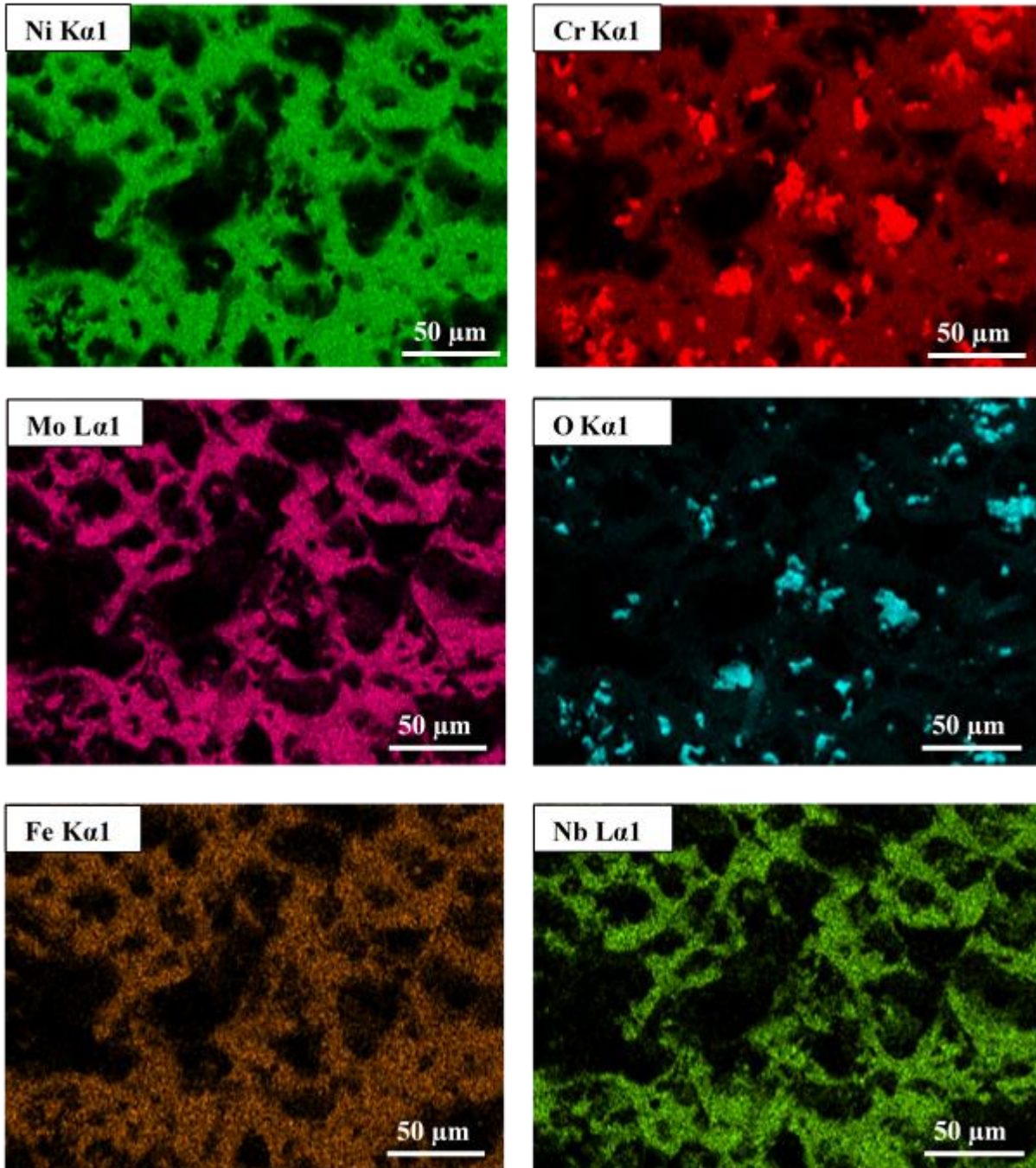


Figure 37. Individual element maps of binder jetting fracture surface based on EDS, oxygen element (blue) is existent within the captured powder particles in high concentration.

Table 10. Chemical composition of binder jetting fracture surface, oxygen content is highlighted since it has increased from the stock powder material.

Element (wt %)	Ni	Cr	Mo	O	Fe	Nb
Wt%	56.84	29.23	5.22	6.35	2.33	0.04

Using EDS point scan functionality, the chemical composition of a specific region within the SEM image was analyzed. This analysis was performed on randomly selected un-sintered particles and on the metal matrix. The obtained images indicate a large concentration of oxygen that is not typical for Inconel 625 chemical formation. Furthermore, the EDS results indicate that the particles are chemically composed of chromium, nickel and oxygen, and the metal matrix shows an atypical concentration when compared to Inconel 625. A change in the other elements may have been affected due to the larger area scanned in comparison to powder analysis. Figure 38 shows an SEM image supplemented with the EDS point results. Chromium can be a sensitive element susceptible to oxidation, due to thermodynamic stability that is achieved when oxides react onto surface at elevated temperatures [65]. As oxygen is in contact with the surface of powder particles, in some cases at ~20%wt, the oxide layer may inhibit bond formation and sintering between particles leading to encapsulation allowing these particles to remain un-sintered, and unaffected in the rest of the material [66].

The reason for higher content of oxygen in the matrix, and the presence of un-sintered particles might be related to the two unique steps only conducted by binder jetting, differing from the two powder bed fusion technologies. These steps are, as mentioned prior, curing producing a green body process and the sintering process. Sintering of samples must be performed at around .80T_M of material, where elevated temperatures are a necessity. The sintering does take place in

an inert gas environment, lower oxygen content but not fully eliminating it from the environment may be a source to form oxide layers onto powder particles. Another source of oxygen, is the use of the ethylene glycol monobutyl Ether binder that during burnout may form oxides on internal powder particles

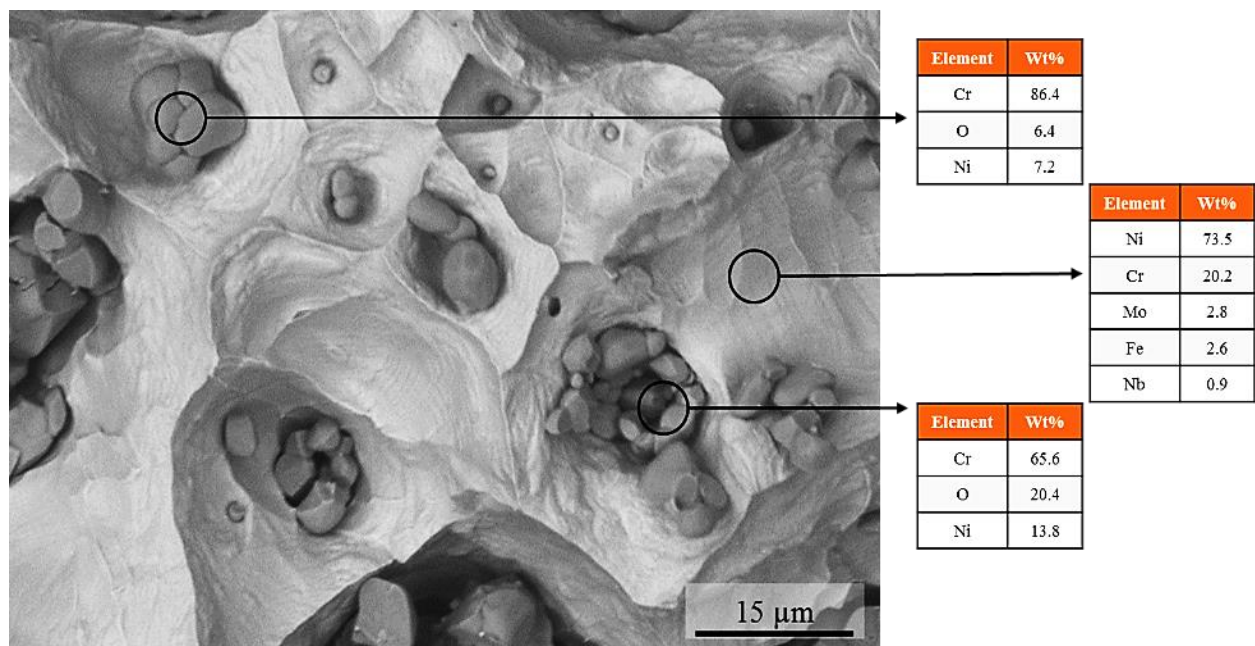


Figure 38. SEM image of binder jetting fracture surface accompanied by EDS analysis on individual particles found on micro-voids as well as the matrix metal.

6.5 Chapter Conclusion

This chapter has presented a fractography analysis that was performed on fractured surfaces of tensile specimens. The evidence suggests the main failure mode for all tested specimens was ductile. This is due to features such as micro-voids or dimples and the double cup formation present in the fractured surface. Some remarks worth of mention include the dimple formation of SLM specimens built in both X and Z orientations, which resembled those seen traditional in Inconel 625 fractures [67]. The EBM specimens fabricated in the X build orientation showed a “woody” fiber pattern in relation to the γ'' precipitates formed in a columnar formation during the fabrication process. The precipitates acted as barriers preventing micro-void coalescence, thus increasing mechanical properties. An additional fractography analysis was performed for an as-fabricated EBM specimen built in the Z orientation that allowed to distinguish un-sintered powder particles that are responsible for pre-mature failure during testing. Un-sintered powder in specimens has been identified as the source of lower mechanical properties pertaining to the non-bonded within the material matrix. Binder jetting specimens demonstrated the formation of oxides on certain powder particles, reducing the bonding effect of the powder particles. Oxide formation detected on un-sintered powder particles, not present in the initial powder, reduced component's density and led to stress concentration, effectively lowering the mechanical properties of binder jetting specimens. If possible to perform sintering in a high vacuum cycle continuously throughout the sintering process and modifying the chemistry of binder used for binder jetting fabrication, these un-sintered oxide powder particles may be avoided.

Chapter 7: Stop-and-Go Interruption Fabrication Process Using Powder Bed-Based AM Technologies for Smart Sensing applications

For this dissertation work, the final comparative analysis of the powder-bed based AM technologies, was based on the feasibility of fabricating “smart parts” with all three. A part is considered to be “smart” if it has the addition of an embedded components, such as sensors or electronics that provide extended functionality to increase functionality and performance. To achieve the process of “smart part” fabrication, the regular additive process was modified to allow insertion of components. This was achieved by pausing the additive process at a prescribed location, followed by sensor insertion, and then resuming of the additive process until fabrication was done, resulting in multi-functional final product. Specific methodologies were followed to achieve smart fabrication in all three technologies of interest, having in mind their requirements, process steps, and limitations. The following discussion describes the methods of fabrication that were implemented in all three technologies that allowed embedding of a piezoelectric ceramic sensor, that resulted in multi-functional metallic or “smart part” capable to withstand harsh environments.

A “smart part” design (seen in Figure 39) referred as a “smart cylinder” was the initial component that was explored for proof of concept. This smart cylinder had a piezoelectric ceramic inserted at the center of the design, achieved by accessing the unfinished component at the desired position. Following the insertion of the piezoelectric, other components that include electrodes, sensing ceramic, and an insulation ceramic, and then the build sequence is resumed. The result is a monolithic component with sensing capabilities for use in high temperature and pressure applications.

During the process of fabricating a smart part, an interface is formed between material that is deposited prior to the pause, and the material deposited after the pause. From a functionality perspective, it was important to characterize the metallurgical soundness, microstructural variations, and chemical composition changes across the interface. These parameters are important to ensure survivability and functionality of both the sensors and the smart part.

The final portion of this chapter, is the fabrication of a “smart fuel injector”, embedding the sensor in the internal cavity where the combustion process occurs, to provide temperature reading similar to those obtained by a thermocouples place on the spray tip to prove that “smart parts” are functional. This research is to promote the capabilities of AM technologies for embedding of sensors within energy systems (Figure 39B) to create a cleaner, efficient process

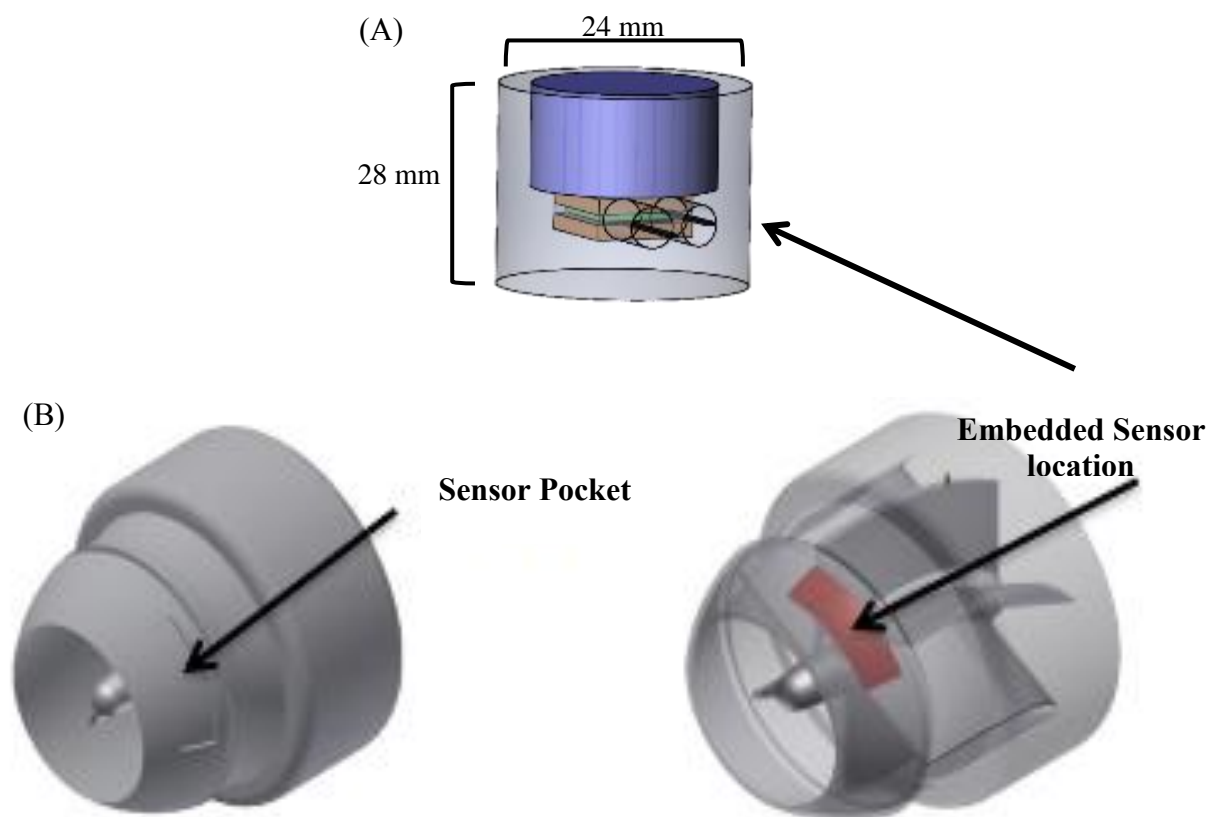


Figure 39. (A) “Smart cylinder” and (B) “smart turbine engine” design where arrows indicate the placement of the embedded sensor.

7.1 “Smart Part” Fabrication using Stop –and-Go Process

The stop-and-go process was an extension of a method previously developed at the W. M. Keck Center done to fabricate multi-material components using EBM technology [43]. To effectively fabricate smart part using all three powder bed-based AM technologies, an embedding method in variation was designed to adjust to an exclusive fabrication processes providing an opportunity for the insertion of sensor.

7.1.1 EBM Stop-and-Go Fabrication Method

The first process, detailed in Figure 40, is defined for the technology of EBM. The steps include the fabrication of insert part and bottom part (step 1), where a mask plate is introduced (step 3) to create a flushed fabrication surface. The assembled bottom part is placed within the mask plate using a press fit to insure a tight fit between the two parts. Due to the centering of electron beam prior to fabrication, a misalignment issue was observed between the two build, pertaining to human error. [68]

7.1.2 SLM Stop-and-Go Fabrication Method

The SLM stop-and-go method differs in a few steps than those required for EBM fabrication. First no mask plate is required for the continuation of the fabrication process. In contrast to the EBM process, no issues are experienced with misalignment for the SLM built smart parts since the fabrication plate is bolted during the fabrication process. Next, the completed “smart part” is removed from the build plate by using a band saw, where in EBM the part just removed using a press fit. Figure 41 list and illustrates the steps of the SLM fabrication method.

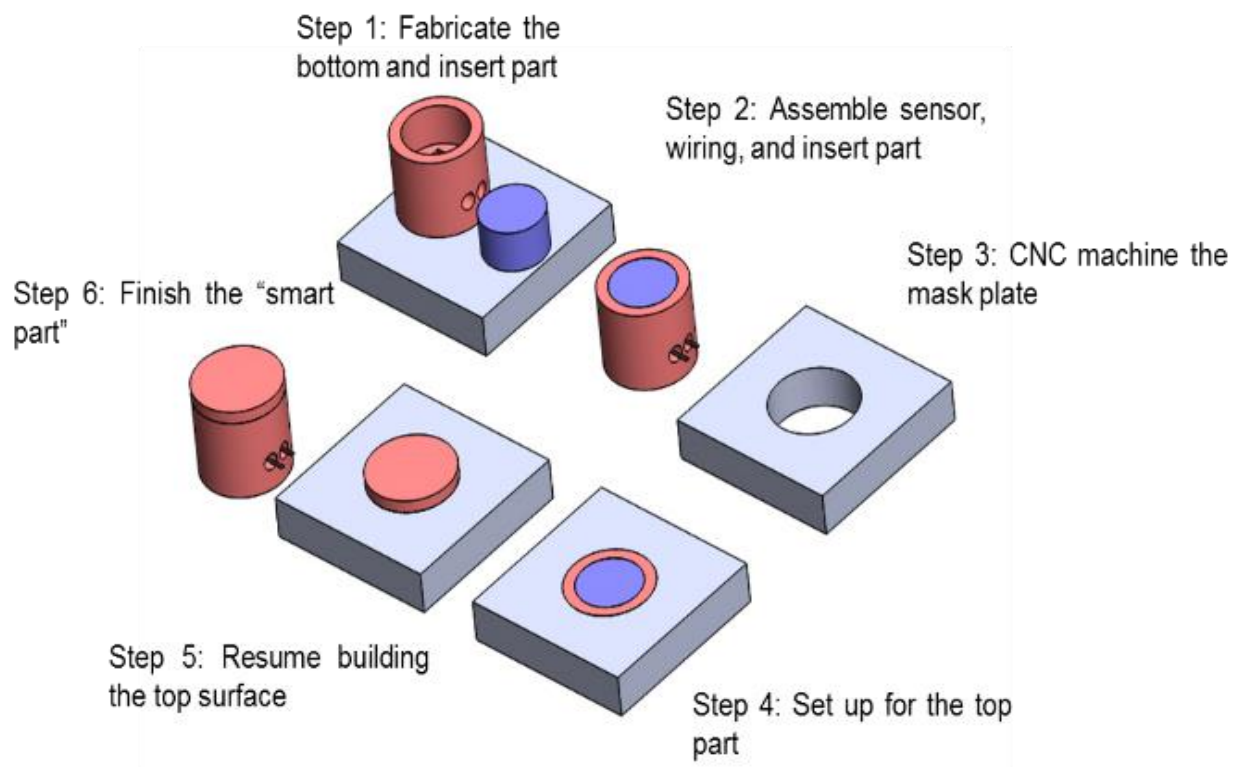


Figure 40. EBM fabrication process integrating a stop-and-go method for the insertion of a sensor for pressure and temperature sensing reading capabilities [68].

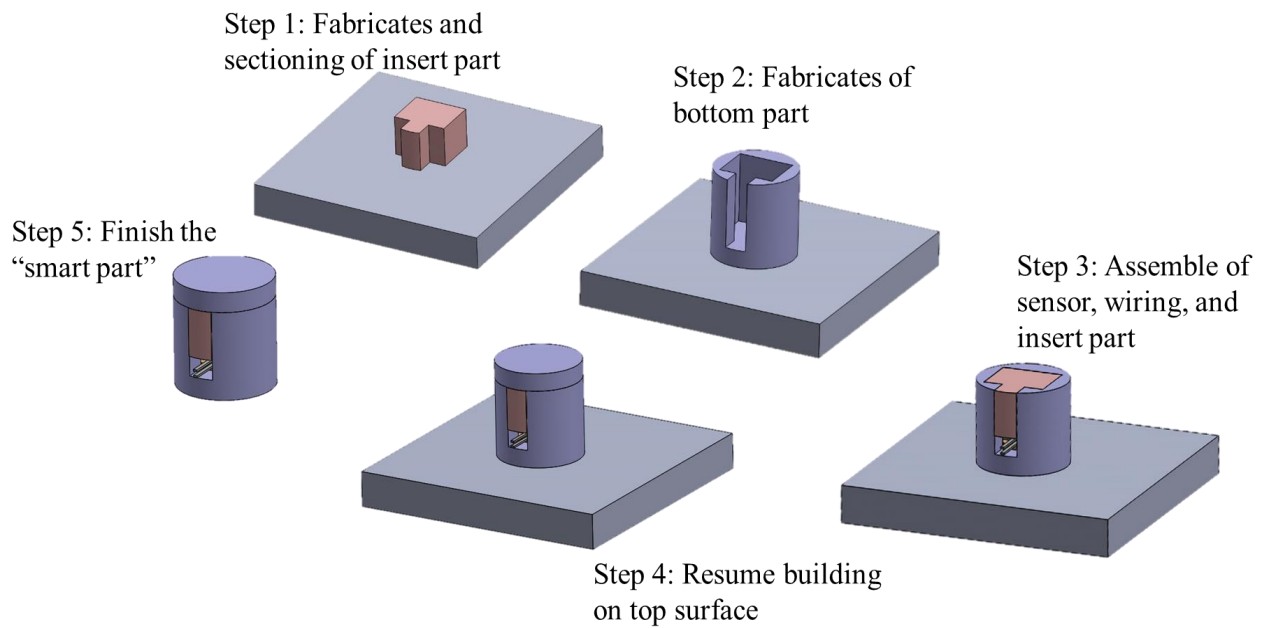


Figure 41. SLM fabrication process integrating a stop-and-go method for the insertion of a sensor providing pressure and temperature reading capabilities.

7.1.3 Binder Jetting Fabrication Method

In the case of smart part fabrication using binder jetting, this objective is accomplished in an easier fashion as compared to the EBM and SLM processes described before. First, a single step instead of a stop and go process is performed. In this process, green bodies are fabricated for the cavity that serves to insert the sensor, and a cap that will cover the sensor in the finalized smart part. After fabrication of these parts, the sensor is inserted in the cavity and the cap placed atop. Then the whole assembly is subjected to sintering to achieve densification. A detailed diagram with the steps to achieve smart part fabrication in BJ is shown in Figure 42. This fabrication method is still being developed and evaluated to determine if it is considered an efficient fabrication process for the creation of “smart parts”. Due to the bonding between the two separate components, a deficient or lack of bonding may be accomplished not resulting in adequate fabrication method for such energy systems, but developing only a fabrication method. Further experimental producers and sintering are to continue to achieve the fabrication of a functional “smart part”.

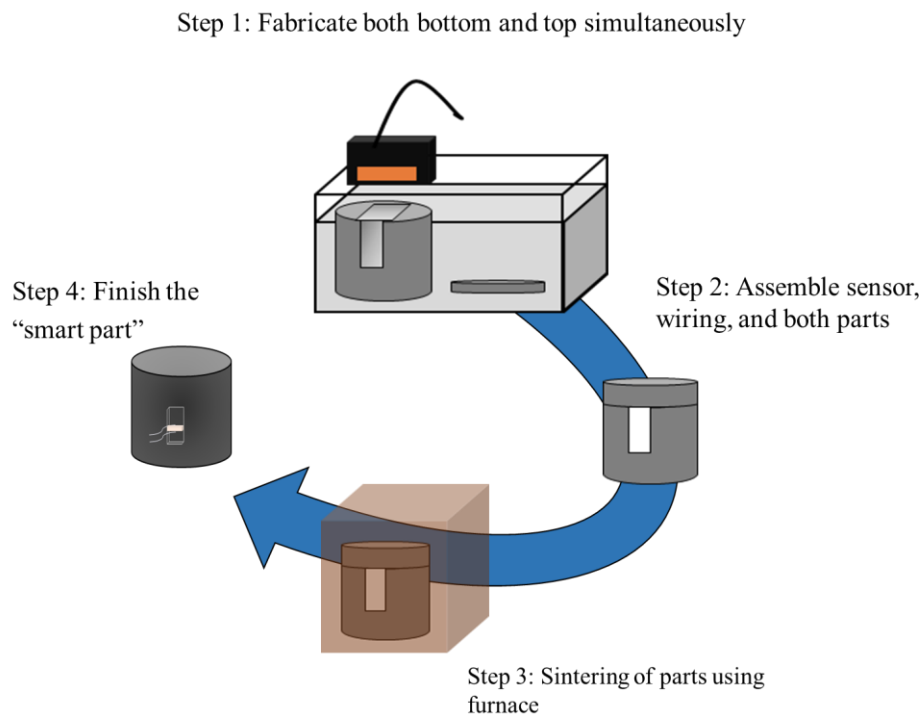


Figure 42. Binder jetting fabrication process steps to produce “smart parts”, where a sensor is embedded providing pressure and temperature reading capabilities

7.2 Sensor Protection by Housing Design

After initial trials for smart part fabrications, the need to provide protection to either the sensor or its electrical leads, through the use of an electrically insulant material, was identified [68]. This was necessary to guarantee functionality of sensor after fabrication, and to prevent sensor deterioration when the “smart part” was exposed to harsh environments during the initial fabrication trials of the smart cylinder in EBM. A simple alumina plate was originally used as insulation material (design 1 shown in Figure 43), however the EBM fabrication process caused metallization to occur onto the surface of the piezoceramic material effectively shorting the sensor circuit. This phenomenon arises due to the vacuum and high temperature environment where the metal powder is melted during the EBM fabrication process. Metal is then evaporated and as it condensates as a thin metal fil on the ceramic material, it makes it conductive. The alumina parts were then producing a low resistance of about $\sim 31\Omega$, making the material conductive. SLM did not have the metallization problem and design 1 was used for the fabrication of the “smart cylinder”.

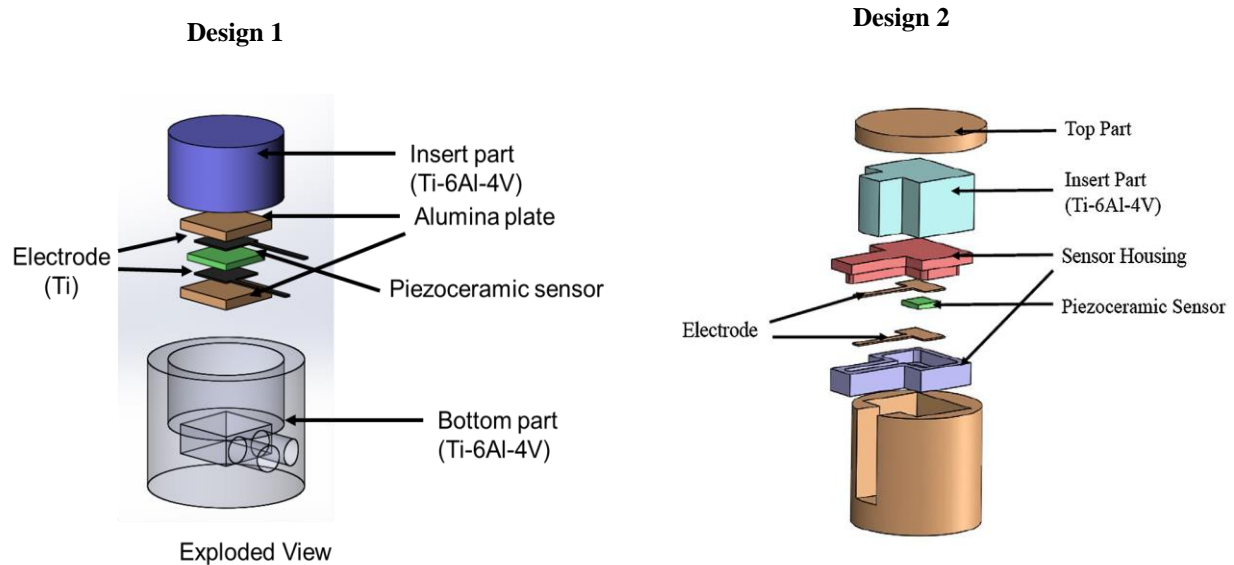


Figure 43. Exploded views of the two different designs used for the “smart cylinders”. Design 1 (left) uses two simple ceramic plates to isolate the sensor from the metallic body, where design 2 (right) contains a ceramic sensor housing for protection of sensor in harsh fabrication environments [68].

To prevent the undesirable effects of metallization, a more complex design (Figure 43 design 2) consisting of a ceramic enclosure, was implemented to reduce exposure of piezoceramic surfaces. the open surfaces and exposure of the sensing material. The enclosure was designed to avoid any form of metallization while still allowing sensing capabilities for the piezoelectric ceramic. Design 2 utilized a sensor housing (Figure 44) where the piezoelectric ceramic is contained, while an electrode leg allows for electrodes to be connected after the smart part is fabricated. The housing was designed out of alumina to withstand high temperatures. The housing was machined from an alumina block (Cotronics Corporation, USA) using a CNC Mini Mill 2 (HAAS Automatic Inc., USA) (Figure 45). The housing along with the sensor and electrodes are fitted into the cavity, then topped with the previously fabricated part, allowing fabrication to continue using EBM technology.

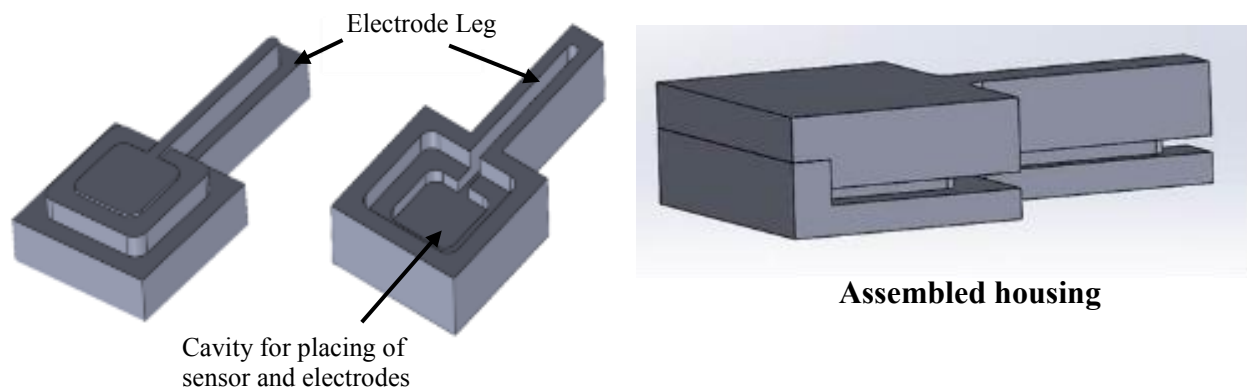


Figure 44. CAD design of the two parts of the sensor housing, followed by the assembled housing

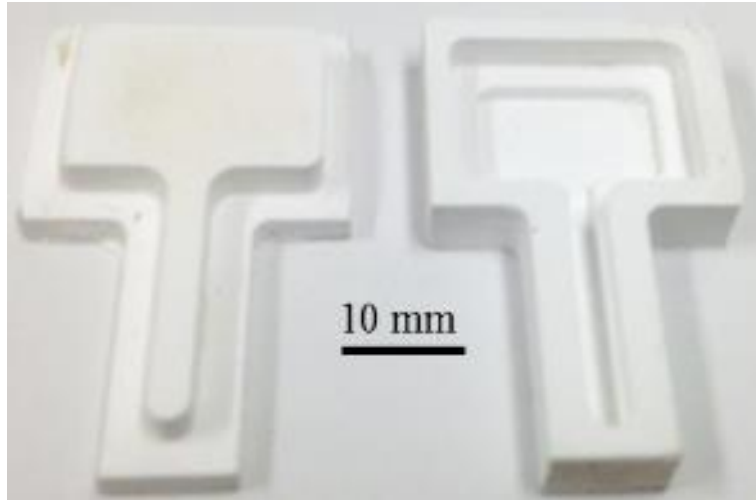


Figure 45. Sensor housing fabricated from machined alumina [68]

7.2.1 Fabrication of Ceramic Sensor Housing Using Binder Jetting Technology

A second method to fabricate the sensor housing was implemented exploiting binder jetting additive manufacturing. The sensor housing was fabricated on an ExOne M-Lab system (Irwin, PA serial number: 0600H2) using alumina powders of different grit sizes that were obtained from Ted Pella, Inc. Three unique grits size 240, 320, and 400 were blended together to achieve a large powder particle size distribution (15-106 μ m).

During the fabrication experiments, the layer thickness and the sintering profile were identified as the two key parameters to produce dense parts. Three layer thicknesses were used for these experiments and they were based on the powder particle size of the alumina at 106µm, 45µm, and 15µm [23]. With respect to the sintering cycle, two profiles were investigated corresponding to sintering times of 2hr and 16hr respectively [23]. Sintering was conducted using a Rapid Temp Model 1710 FL Laboratory Box Furnace (CM Furnace, Inc., USA), where the soaking temperature determined for the sintering profile was set at constant 1600 °C (0.8T_M of Alumina). Using the Archimedes method the maximum density obtained for the ceramic housing was 96.51% [23].

To fabricate the housing to the correct dimensions, shrinkage factors for the three ordinate directions were applied to the CAD before fabrication. These shrinkage factors were determined as 8.75% in the X direction, 10.92% in the Y direction, and 8.63% in the Z direction [23]. Figure 46 shows an image of the green body sensor housing, accompanied by the final product after sintering was performed. Table 11 summarizes the fabrication parameters for producing alumina with binder jetting AM technology.

After experimentation, the build parameters providing better fabrication were a layer thickness of 45 µm with the sintering profile of 1600 °C for 16 hrs. [23]. The quality of fabrication for the ceramic housing was evaluated by measuring density of constructs. This was done as before,

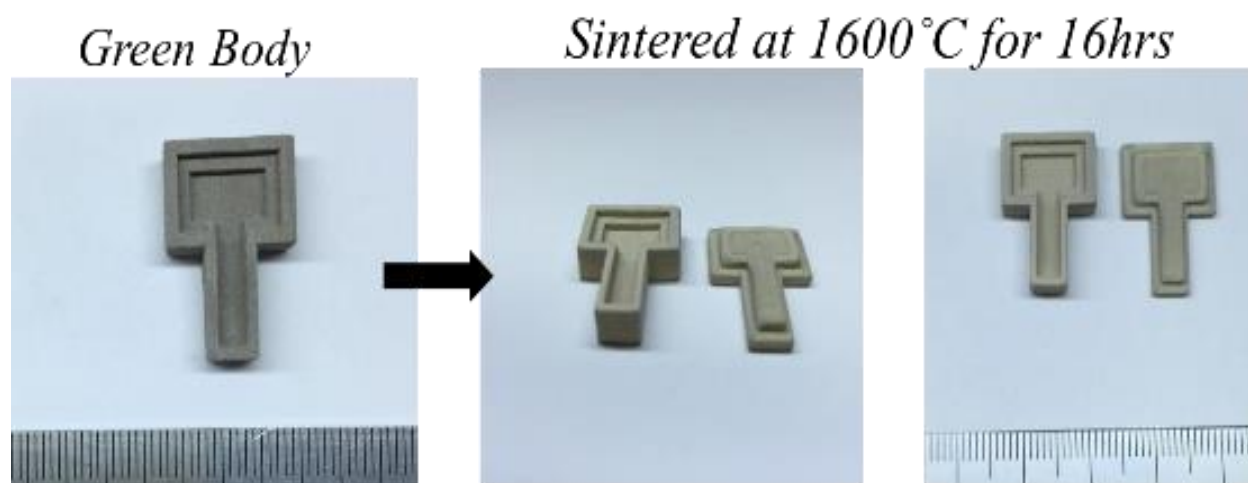


Figure 46. Alumina fabricated sensor housing using binder jetting AM technology.

Table 11. Characterization of alumina fabricated parts using binder jetting AM technology

Particle Size	Layer Thickness	Apparent ρ	%Relative ρ	X% Shrinkage	Y% Shrinkage	Z% Shrinkage
Mixed	45 μ m	3.81g/cm ³	96.51	8.75	10.92	8.63

Both fabricated sensor housings were used for only EBM fabrication of the “smart cylinder”, and the machined housing was determined to have better protective properties against metallization, due to porosity still existent in the housing fabricated by binder jetting.

7.3 Interface bonding

The properties of the interface formed during the stop and go process for producing smart parts were evaluated. One smart part fabricated was cross sectioned using a IsoMet 4000 Linear Precision Saw (BUEHLER, Lake Bluff, IL) parallel the build direction, and mounted in resin to characterize the interface formed during the stop and resume fabrication process. A similar procedure for grinding and polishing was followed, as described before. The etching step to reveal microstructure was done selectively, depending on the AM technology used for fabrication. For the EBM fabricated smart part Keller’s Reagent (95% distilled water, 2.5% nitric acid, 1.5% hydrochloric acid, and 1% hydrofluoric acid) was used. The SLM fabricated smart part, was electro-etched (5V for 7 seconds) using chromic acid. An accumulation of various micrographs were taken Leica Reichert MEF4 A/M optical microscope (Leica Microsystems, Wetzlar, Germany) which were stitched (a set of images compressed together) in order revealing the entire area of the microstructure for the interface in a single micrograph. The analysis was done to evaluate potential microstructural variations from each of the regions adjacent to and at the interface. The lack of these microstructure variations indicates the metallurgical soundness at the interface which is preferred to avoid potential anisotropy of mechanical properties or poor metallurgical bond that could lower performance of “smart parts”.

7.3.1 Microstructure Evaluation of Stop-and Go Process

The microstructure of the EBM fabricated “smart part” is represented in Figure 47. A magnified view of the first material deposited (first build), the interface, and the second material deposited (second build) are seen in Figure 47 (B), (C), and (D) respectively. From observations of these micrographs, a Widmanstätten microstructure is present throughout the two built sections

with alternating α (light) and β (dark) phases. Alpha phase (HCP) formation is stabilized by the 6%wt aluminum, and beta phase (BCC) is stabilized by the 4% wt vanadium [69]. The second built has an appearance of finer grains than that of the first built. Comparing the lath thicknesses between the two regions, material fabricated in the second step had a lath thickness of $\sim 1.3\mu\text{m}$, whereas the first step had lath thickness of $\sim 2.4\mu\text{m}$, or an 85% increase in thickness. A decrease in alpha grains size might be a beneficial effect as it can lead to improvement in yield strength, ductility, and crack propagation [69]. The increase in thickness of the first deposited material can be explained from exposure to elevated temperatures for longer times due to the second material deposition process. The interface at the microstructure appears to have a large amount of coarse grains in comparison the other two regions identified in the micrograph. The microstructure for the SLM fabricated “smart part” is shown in Figure 48 with all three regions of interest highlighted: where (B) is first material deposited in the first build, (C) interface, and (D) material deposited in the second build. The micrograph reveals the presence of melt pools, with no distinguishable difference amongst the three regions. After magnification, similarities in precipitate formation are also observed for all regions. Similar precipitate formation was observed for SLM produced Inconel 625 as described previously in chapter 5. The main difference observed between regions was the distance between the melt pools of the first and second builds to the interface. As the second build process is initiated, the top surface of the material deposited in the first build is affected by the laser multiple times leading to this pattern of melt pools that appear closer; whereas for the first build the melt pools are distanced in average $23\mu\text{m}$, for the material deposited in the second build, this distance averages $45\mu\text{m}$. This metallurgical effect might be removed with appropriate heat treatment that can effectively remove the observed melt pools and leave an equiaxed and homogeneous microstructure. (Chapter 5 section 5.3). From the discussion above, it can be concluded that the microstructure before, at, and after the interface is more homogeneous for the SLM produced smart parts, indicating higher metallurgical compatibility and soundness of the bond. Therefore, this technology might be preferred for fabrication of smart parts.

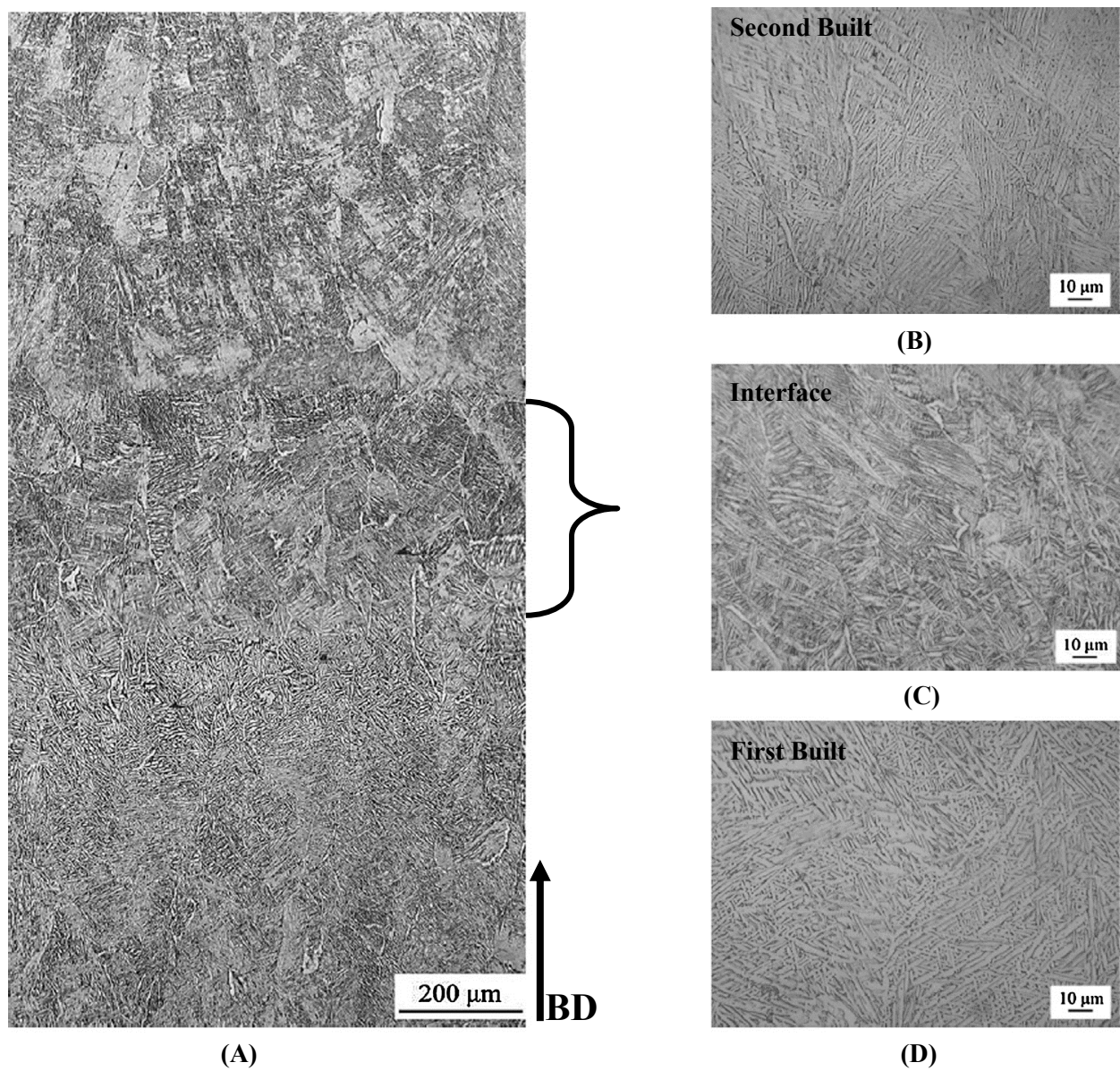


Figure 47. Optical images of microstructure for EBM fabricated smart part, (A) entire microstructure view showing the evolution of the microstructure is paused, then continued; with a magnified view of (B) Second fabrication, (C) interface bonded section, and (D) first fabrication [68].

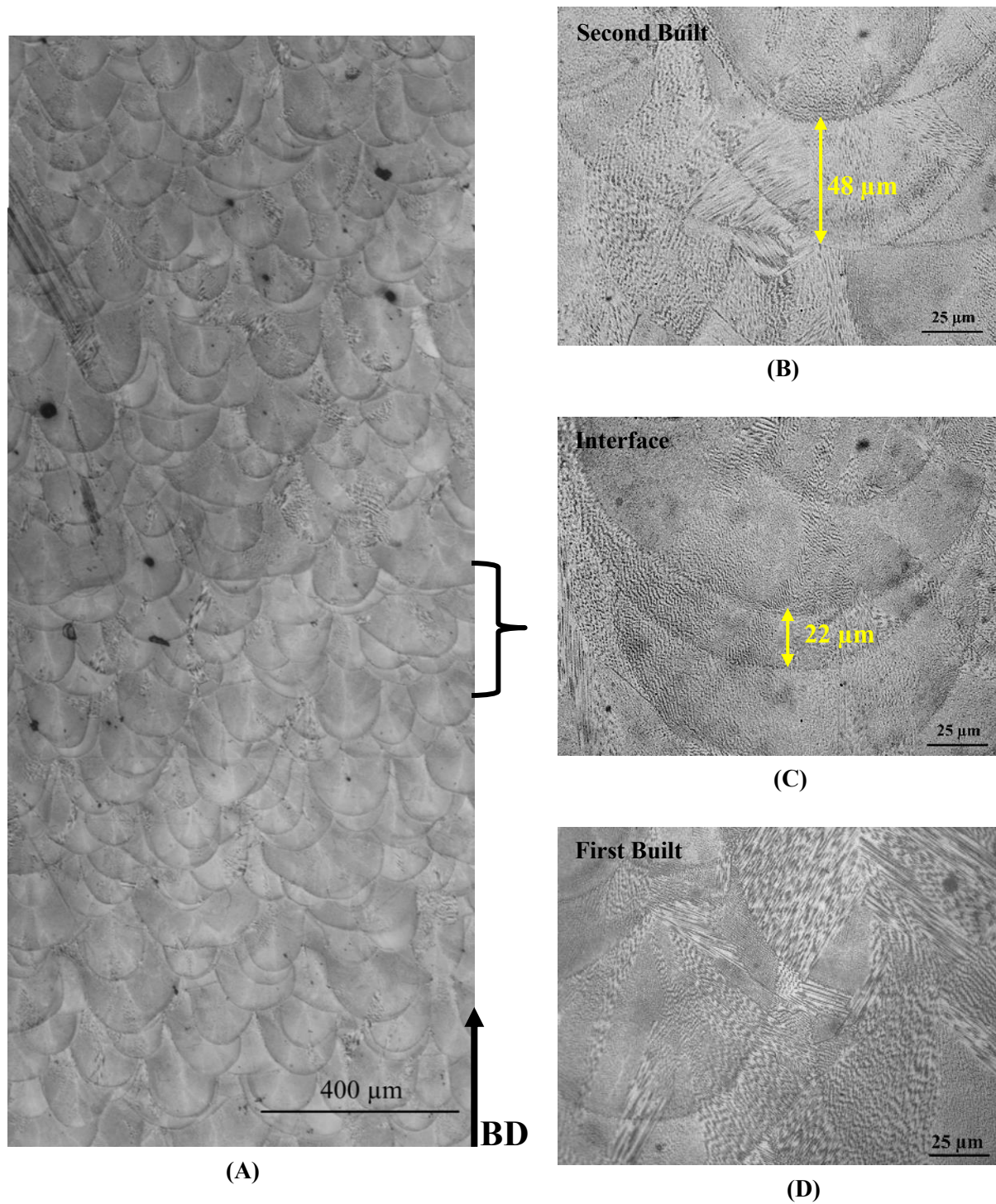


Figure 48. Optical images of microstructure for SLM fabricated smart part, (A) entire microstructure view showing the evolution of the microstructure is paused, then continued; with a magnified view of (B) Second fabrication, (C) interface bonded section, and (D) first fabrication.

7.3.2 Chemical Composition Evaluation of Stop-and Go Process

To determine any type of discrepancies in chemical composition created during the multi-step fabrication process, EDS was performed on the three areas of interest: before, at, and after the interface. “Smart parts” were viewed under a Hitachi Scanning Electron Microscope SU3500 (Japan) creating SEM images, followed by EDS analysis using AZtecEnergy (Oxford Instruments, UK) acquisition and EDS analysis software.

An SEM image of the microstructure of an EBM produced “smart part” is shown in Figure 49 with areas that were investigated by EDS highlighted in yellow bounding boxes. EDS results show similar chemical composition for first build, interface, and second build. This supports the claim that all three areas of interest share a similar Ti-6Al-4V microstructure. The results of the EDS analysis (% content for each element) are listed in Table 12.

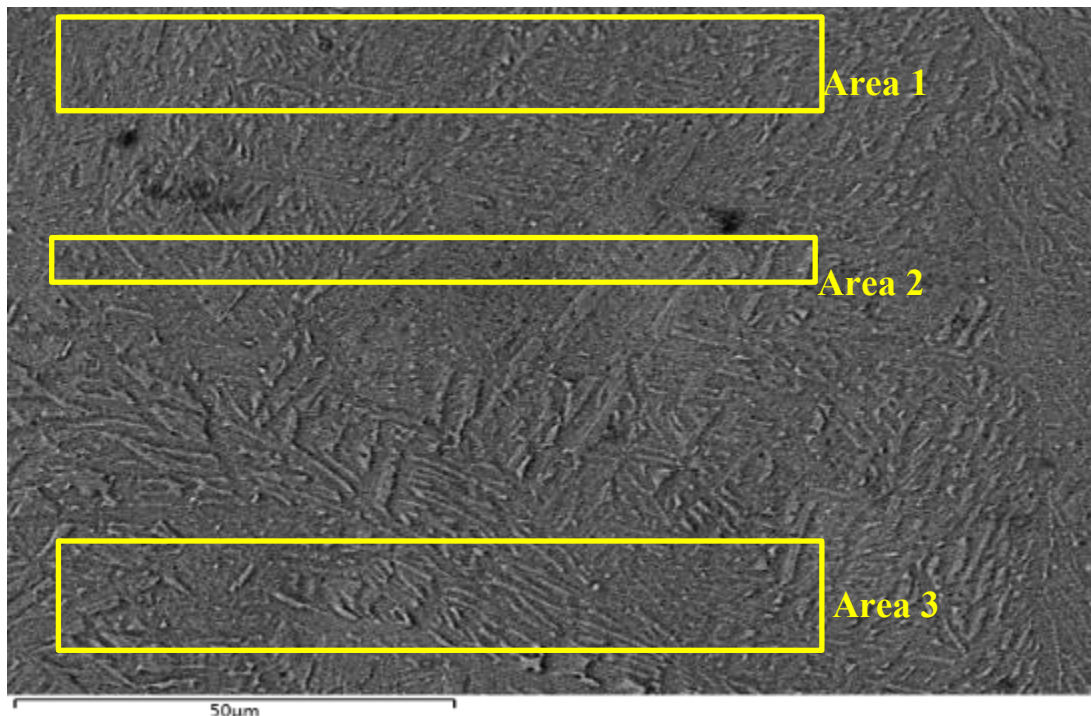


Figure 49. SEM image of the EBM interface indicating the three individual areas where EDS analysis was performed.

Table 12. Chemical analysis of the three individual areas for the stop-and-go EBM fabricated sample

Element (wt. %)	Ti	Al	V
Area 1 (Second build)	90.4	5.3	4.2
Area 2 (Interface)	90.6	5.3	4
Area 3 (First build)	90.2	5.4	4.4

The EDS analysis was also performed on the “smart part” fabricated by SLM. Figure 50 shows the SEM image that was used for EDS analysis, with the three areas investigated highlighted in yellow boxes. In this case, no differences in chemical composition were seen for the three areas of interest. The EDS analysis indicates the three regions have the conventional chemistry of Inconel 625 (Table 13).

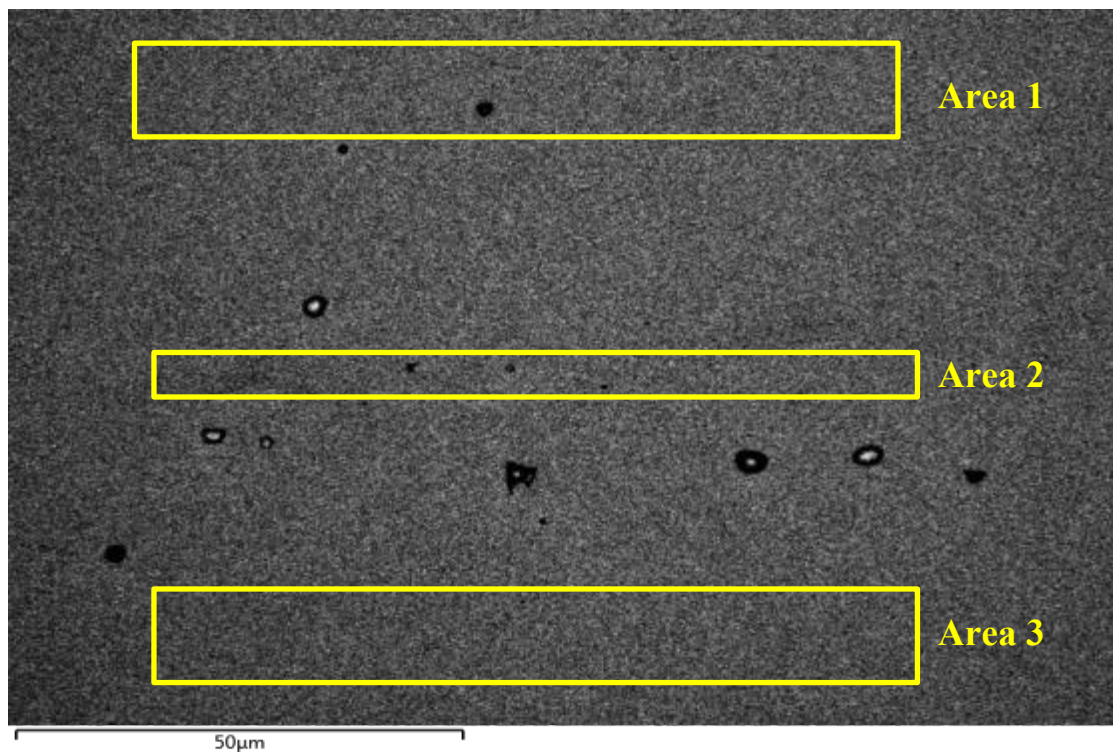


Figure 50. SEM image of the SLM interface indicating the three individual areas where EDS analysis was performed.

Table 13. Chemical analysis of the three individual areas for the stop-and-go SLM fabricated sample.

Element (wt. %)	Ni	Cr	Mo	Nb	Fe
Area 1 (Second build)	63.39	21.76	8.79	3.32	2.47
Area 2 (Interface)	64.3	21.7	8.2	3	2.3
Area 3 (First build)	63.9	21.8	8.6	3.2	2.4

7.3.3 Identified Defects on Interface

During the stop and go process, the interruption can lead to the development of defects after the build is resumed. As the new layer is raked onto the already existent surface, some powder particles may not fully melt, as revealed in micrographs. For example, Figure 51 shows defects at the interface of EBM produced “smart parts”. Similarly, Figure 52 shows defects that developed in the SLM produced smart part. These defects are spherical voids or pores that appear to originate from un-melted powder particles removed from the surface during preparation of the metallographic specimen. These defects indicate the potential for optimizing the stop and go process for the SLM technology.

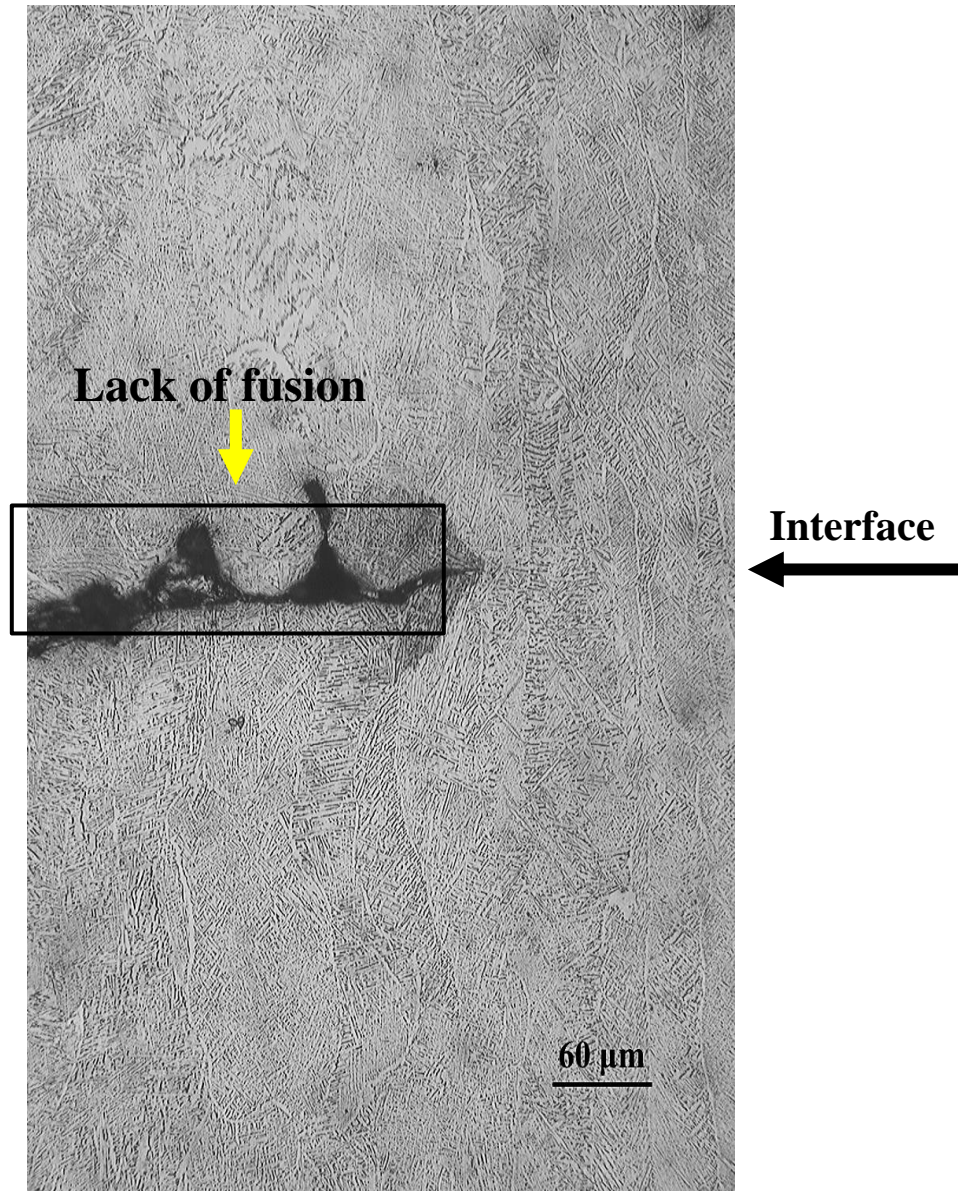


Figure 51. Optical image detecting a defect from the stop-and-go EBM fabrication process, where certain powder particles were not melted during second fabrication.

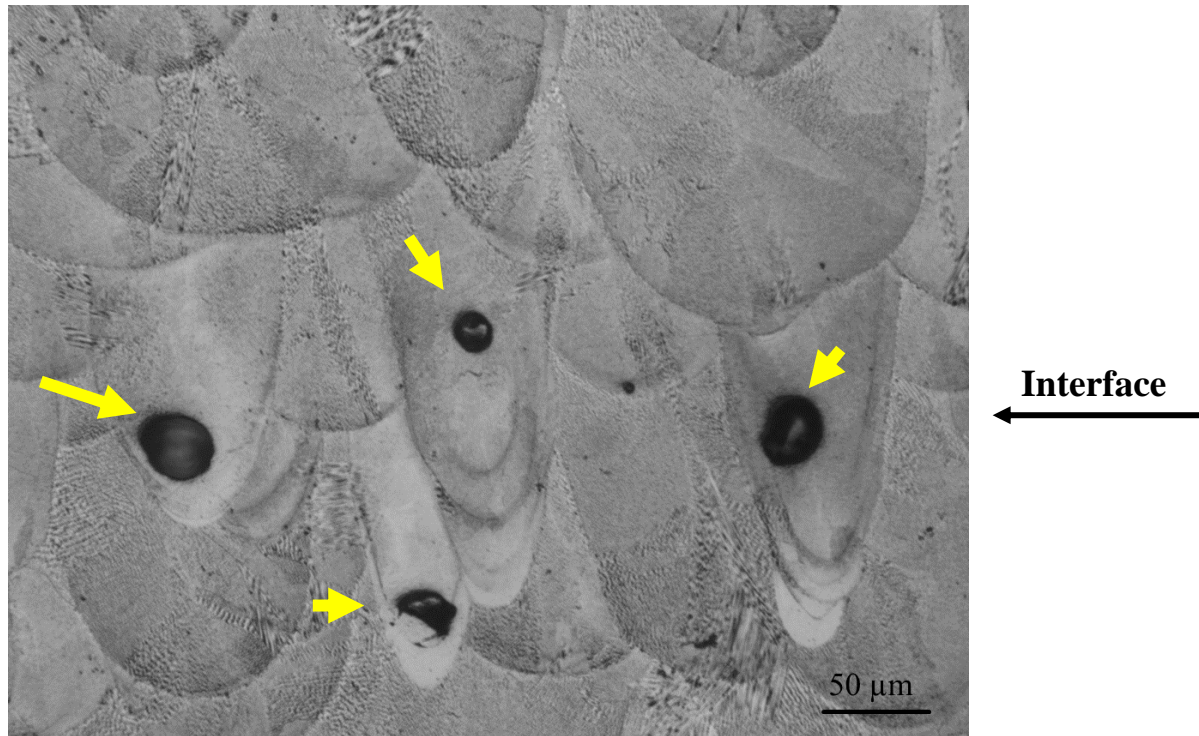


Figure 52. Optical image detecting a defect from the stop-and-go SLM fabrication process, where pores can reduce the bonding of the two different builds

7.4 “Smart Part” Sensing Capabilities

The force sensing capabilities of “smart part” were tested using a compression-compression test. For these assessment, a load concentrator was used to apply the load on the center plane of the “smart part”. The electrodes of the “smart part” were connected to a Data acquisition system (DAQ) using a clamp to record the voltage response (V) [68]. Four different load application frequencies were used for testing the sensing range across various dynamic loads. The frequencies were 10Hz, 15Hz, 20Hz, and 25Hz [68]. The piezoelectric voltage response under these frequencies, showing correspondence to the applied force (F) is graphed in Figure 53 [68]. The charts indicate the functionality and sensitivity of the piezoelectric sensor embedded in the smart part [68]. The results obtained for the fabrication of smart parts are encouraging, and they warrant continued development of this concept in future research thus, providing a working “smart part” was achieved using powder bed fusion AM technologies, and leading to further development in “smart part” design.

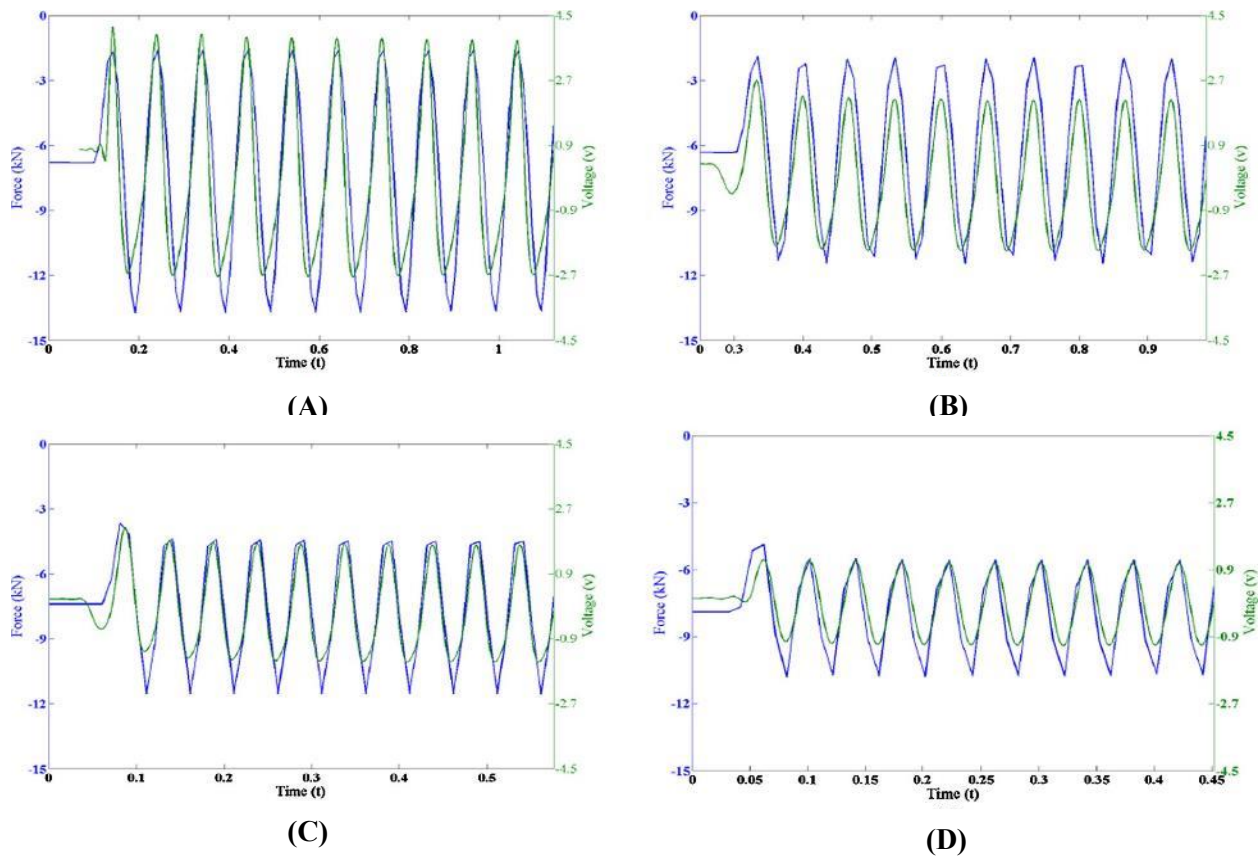


Figure 53. Voltage response based on compressive applied force obtained from “smart part”. The voltage response was obtained at frequencies of (A) 10Hz, (B) 15Hz, (C) 20 Hz, and (D) 25 Hz [68].

7.5 Applications of “Smart Parts”

The success in producing smart parts using powder bed fusion AM techniques was used to explore the next objective of this research. This objective was the fabrication of a smart components with a real-world application in an energy system. The component selected was a coaxial shear fuel injector that would be tested at the facilities of the University of Texas at El Paso. This fuel injector design can be used in high temperature combustion chambers within turbine engines, allowing for operation at lower safety factors with higher efficiencies. The

embedded sensor can also aid with real time monitoring of temperate and pressure during the combustion process. Three “smart fuel injector” were fabricated in total. One injector was made using a combination of electrical discharge machining (EDM) or traditional machining, one using SLM, and one more using EBM. The powder bed fusion technologies had a small pocket for embedding of a piezoelectric ceramic. Two ceramics chosen for sensing, were a lead zirconate titanate (PZT) and lithium niobate (LiNbO_3) due to their resistance to high temperatures (320°C for PZT and $>1210^\circ\text{C}$ for LiNbO_3). Stainless steel electrodes were used to achieve the electrical interconnect, accompanied by alumina ceramic tubes for isolation of internal metallic walls (Figure 54). The three fabricated fuel injectors are shown in Figure 55.

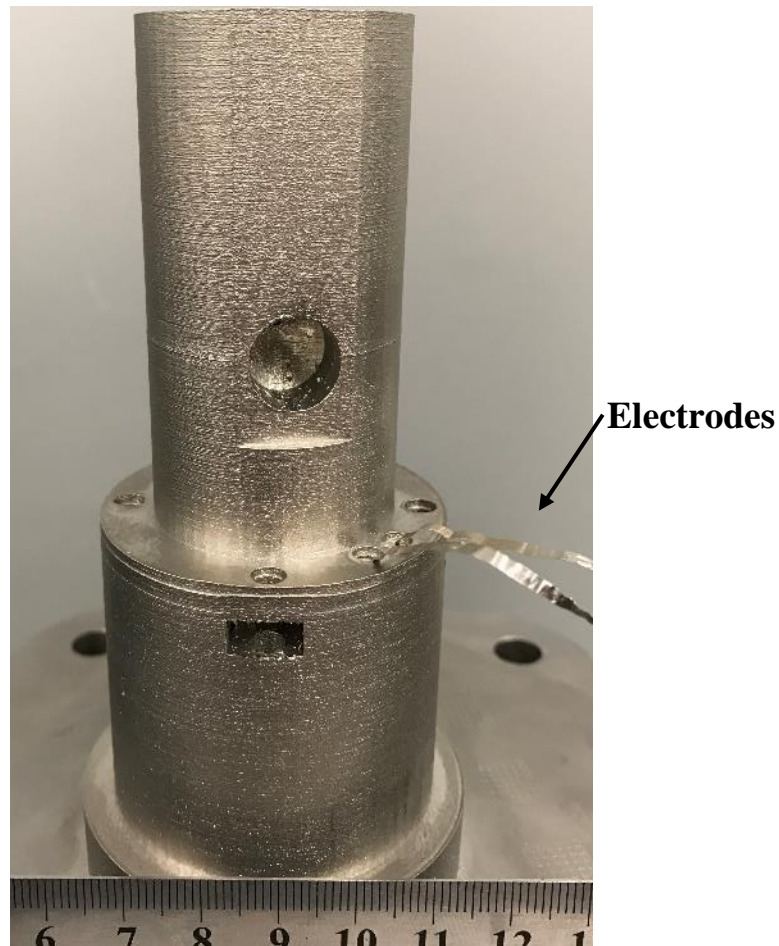


Figure 54. SLM fabricated “Smart fuel injector”

From an injector performance perspective, the general surface (outside) roughness has tremendous a tremendous effect. The roughness values were measured for the three injectors using an optical profilometer. The EBM produced injector measured the highest surface roughness at $\sim 69\text{ }\mu\text{m}$, followed by the one built by SLM with $\sim 23\text{ }\mu\text{m}$, and then the one produced by traditional EDM machined measuring $\sim 9\text{ }\mu\text{m}$. With a 7.6X increase than EDM in surface roughness as compared to EDM, the EBM fabricated injector was not further explored for fabrication of “smart fuel injector”.



Figure 55. “Smart fuel injector” with embedded sensor fabricated using traditional

The SLM process was selected as the best candidate to produce smart injectors for two main reasons: first, because it lowered the cost from an estimated \$6,000 USD from using EDM, to around \$1,500 USD for prototype. The second reason is that fabrication lead times were lower; while the fabrication lead time of an EDM (providing the best results from previous fabrication machined fuel injector is roughly 3 months to achieve), the complexity required, (including internal channels and cavities) whereas the SLM process carries an estimated lead time of 3 days (possibly also effected to in house availability of AM system).

The machined and SLM fabricated injectors were water pressured through both oxidizer and fuel channels separately to see the pressure drop and determining desired flow rate for testing. The main purpose of the design to ensure a functional SLM fabricated “smart fuel injector” by providing heat exposure to the coaxial shear injector and comparing temperature readings measured for the embedded sensor and compared to a thermocouple placed at different location of the system, thus simulating real energy system applications. Experiments were carried out in the Multi-Purpose Optically Accessible Combustor (MOAC), within a Multi Altitude Simulation System (MASS) chamber. The hot-firing test setup is described in Figure 56. The test was conducted at pressures ranging between 20 and 45 psi. Methane gas was used as the fuel along with air as the oxidizer, using a fuel ratio of 17.2., a spark was created using built-in electrodes powdered by a DC high voltage supply. The tests had a duration of 5 to 10 seconds for safety purposes, while still allowing the flux to reach the embedded sensor inside the injector. The pyroelectric current was calculated using the temperature experienced by the sensor during the combustion process.

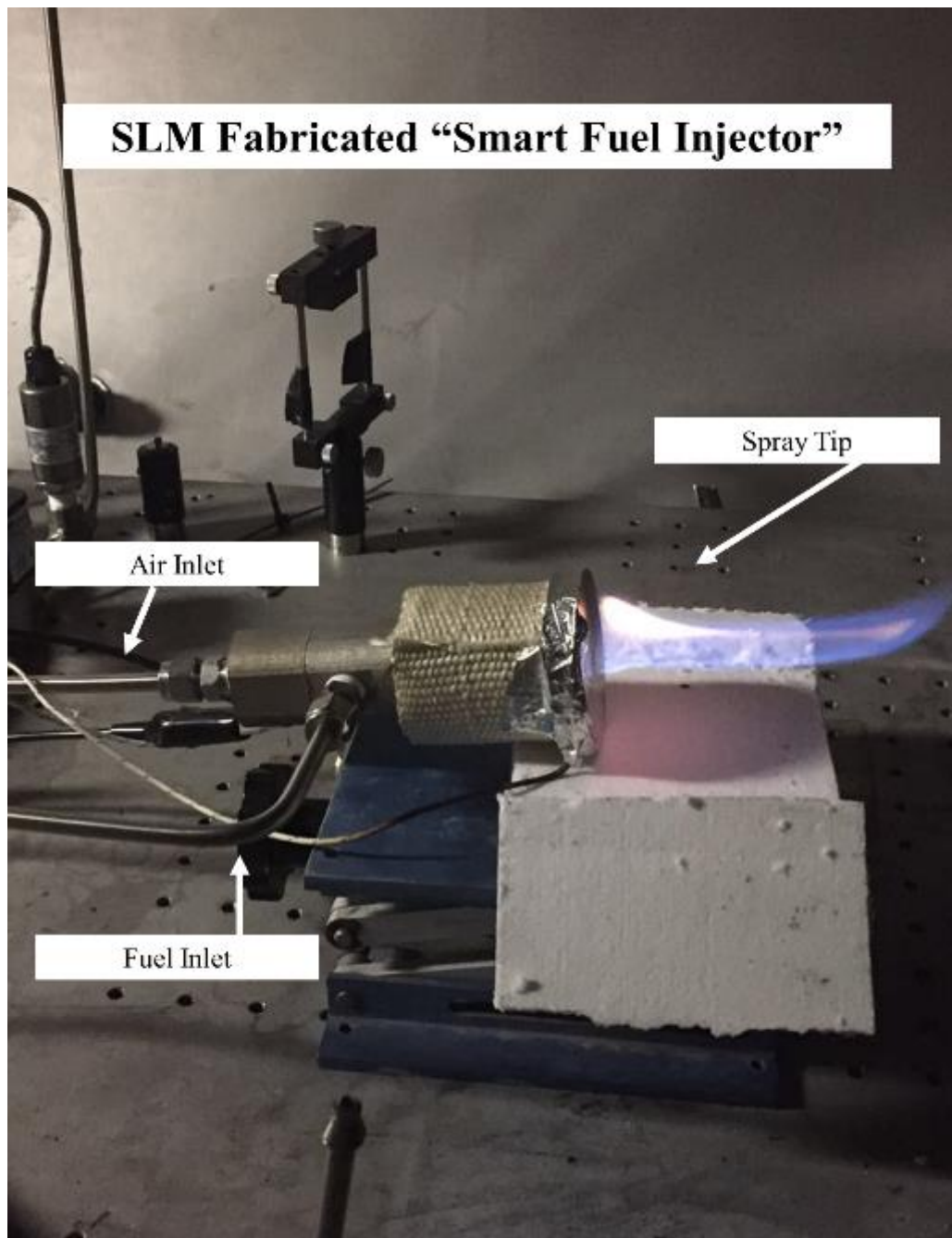


Figure 56. Testing setup of SLM fabricated "smart fuel injector" detailing the fuel injectors componets.



Figure 57. Top view of SLM fabricated “smart fuel injector” spray tip with produced flame after combustion.

The top view of the flame created during the combustion process is shown in Figure 57, indicating proper functionality of the SLM “smart fuel injector. The results of the temperature values obtained both from the pyroelectric sensor and the thermocouple placed at the spray tip outlet, are graphically compared in Figure 58. The chart demonstrates the ability of the pyroelectric for measuring temperatures during the combustion process. The minor difference between the two plots is due to the difference in location of the embedded sensor (internal), versus the thermocouple (external).

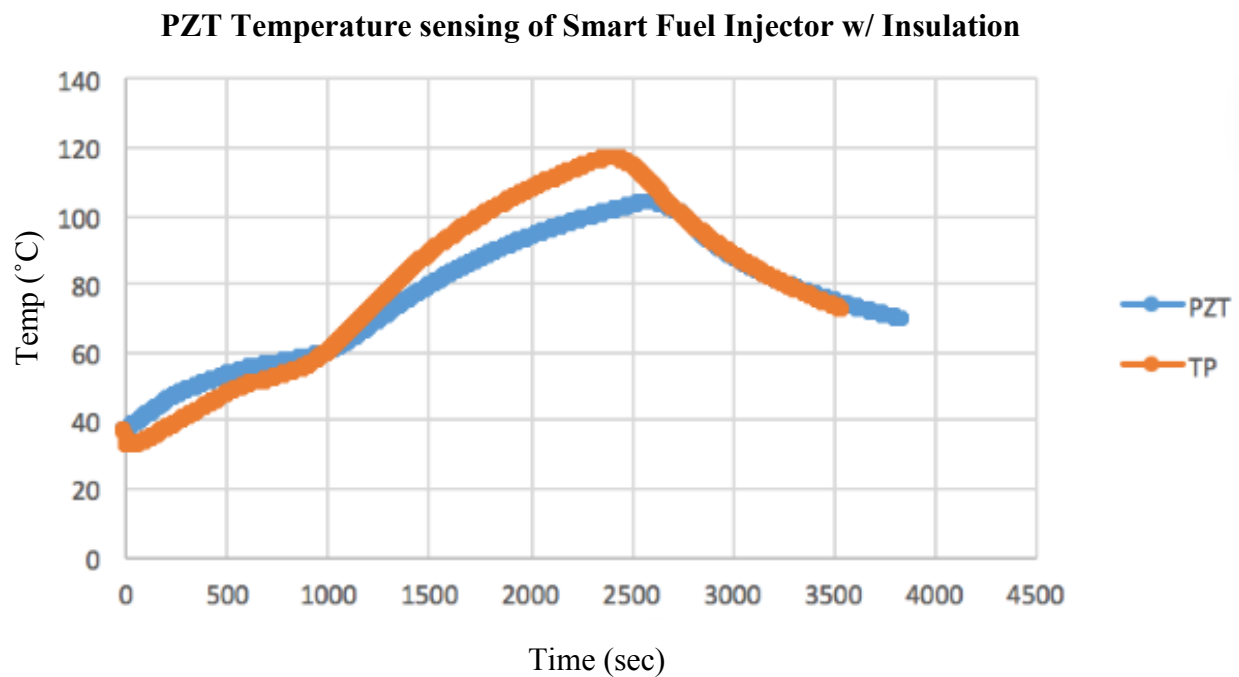


Figure 58. Temperature vs. time experienced by SLM fabricated “smart fuel injector”. Blue line represents values obtained by embedded sensor, where orange values are thermocouple readings.

7.6 Chapter Conclusion

Powder bed fusion technologies were successfully used for the fabrication of energy systems components with embedded sensor, or “smart parts”. A stop and go fabrication method was implemented for each of the AM techniques used. The smart parts were able to measure pressure and temperatures values, indicating the functionality of the embedded sensors. Minor changes in microstructure were observed, caused by the interruption that is required for sensor insertion. However, heat-treatment may be explored for the creation of a uniform microstructure across the various regions formed during smart part fabrication. No chemical compositions discrepancies existed between first build, interface, and second build. During the second phase of the study, a functional smart fuel injector with embedded temperature sensors was fabricated and tested, demonstrating functionality. It can be concluded that the SLM technique is viable for producing smart components with good performance, such as the injector, while lowering the cost and time for production. Future research will investigate the implementation of this and other smart components for real-time sensing and monitoring of energy systems.

Chapter 8: Conclusions and Recommendations

8.1 Conclusions

In this work, three powder bed based technologies were evaluated for the fabrication of metallic components. A powder bed-based AM technology comparison was achieved that included: economic analysis, mechanical and metallurgical study for fabricated Inconel 625, and stop and go demonstration for the fabrication of “smart parts”.

The three systems employed for fabrication time/ energy consumption model comparison were the ExOne M-Flex for binder jetting, a Arcam Q20plus for EBM, and SLM Solutions 280HL for SLM. Through this study, the aim was to identify the differences that exist between these technologies, using metrics that included fabrication time, cost, and mechanical properties. For the cost analysis on initial capital cost was considered. Fabrication time and cost were evaluated for all three systems were assessed under various scenarios of build volume utilization that emulated conditions of use in a production environment.

The final cost comparison analysis concluded that binder jetting provides the least amount of initial capital cost in comparison to EBM and SLM. For a scenario looking at producing single parts of small volume, binder jetting is least effective, given the time associated with the binder curing and the sintering post-processes. EBM technology was shown to be a viable option for a production environment of multiple part fabrication of large volumes. Finally, in the case of SLM, the high fabrication times incurred, due to the laser scanning speed, for large volume builds, but the technique is viable for short production runs including scenarios of single parts, or minimal volume builds.

As for the fabrication of Inconel 625 using the three powder bed-based AM technologies is concerned, binder jetting was the only technology that failed to reach 99.9% dense parts, both as-fabricated and HIPed, creating limiting performance in a couple of mechanical properties (% elongation and hardness). This may be an indication that further advancements can be developed on build parameters for EBM and binder jetting for fabricating Inconel 625. As far as the

microstructure analysis, columnar grains were observed in EBM produced Inconel 625. This directional microstructure, following the temperature gradient in EBM, can be associated with anisotropic mechanical properties. The SLM micrographs showed the arc-shape pattern of the melt pool in as-fabricated specimens, where the pattern was removed once HIPing was performed, leaving behind equiaxed grains. For binder jetting parts the micrographs showed the presence of internal pores and defects that may lead to pre-mature fractures.

The analysis of mechanical properties performed, also indicated differences between binder jetting, EBM and SLM. SLM produced tensile specimens had the highest tensile properties for either X or Z build orientations for as-fabricated and HIPed samples. The as-fabricated EBM specimens had large variation in mechanical properties; however, the variance was reduced after HIPing was performed. All technologies were able to meet or exceed the minimum values for UTS and YS that are required by the ASTM standard F3056-14 making the technologies comparable to wrought or forged Inconel 625 properties. However, only SLM specimens surpassed the minimum requirement for % elongation.

Fracture analysis of the fractured tensile specimens using techniques for macro and micro analysis revealed that all tested specimens failed by ductile fracture mode. All specimens had the formation of dimples, formed through the coalescence of micro-voids, which lead to the rupture of the samples being tested with a uniaxial tensile stress. The EBM specimens fabricated in X orientation showed a “woody structure” or a wood fiber like features that showed correspondence with the columnar precipitates formed during fabrication. The specimens created with binder jetting specimens displayed entrapped powder particles within micro-voids that showed increased levels of oxygen using EDS.

In the last part of this study, the fabrication of “smart parts” (parts with enhanced functionality through embedded sensors) was achieved using both EBM and SLM. A technology specific stop-and-go fabrication process was implemented to allow embedding of sensors within the built component. The method interrupted the fabrication process at a specified layer, allowing the insertion of sensors before resuming the fabrication. The use of embedded sensors can increase

longevity of components as it allows for in-situ monitoring of the environment. In the case of smart components for energy systems, the embedded sensors can enable monitoring of the harsh conditions such as high pressure, high temperature, etc. To demonstrate the technique, a “Smart fuel injector” was successfully fabricated using SLM, and compared against an EDM fabricated fuel injector. The performance of the smart injector was comparable to that of EDM, while reducing cost and fabrication time. Testing of the smart parts demonstrated sensitivity of embedded sensors and functionality of “smart parts” leading to future exploration of advance design.

The properties of the interface created during smart part fabrication was studied through microscopy and chemical analysis. These analyses indicated metallurgical soundness of the interface. However, possible the presence of defects indicates that further improvements are required for the “smart parts” fabrication process.

8.2 Recommendations

While the focus this work consisted of comparing fabrication time, cost, energy consumption, and mechanical and metallurgical features, other variables outside the scope of this work also need consideration prior to the selection of a powder bed-based manufacturing process for a given application. The following are recommendations for future work include:

- ❖ Perform an analysis, measure real time energy consumption data, providing a cost value for part fabrication by each system
- ❖ This study simulated fabrication times. To improve the analysis, experiments are needed to measure the actual energy draw during fabrication for the various build volume utilization scenarios
- ❖ Evaluation of dynamic material properties, such as low and high cycle fatigue. In this work, only the static properties have been evaluated
- ❖ Study to improve sintering cycles of binder jetting, reducing possible oxidation of powder particles

- ❖ Investigation to remove oxidation sources, including binding agent
- ❖ Further microstructure characterization of interface in smart parts to optimize stop and go process
- ❖ Tensile test of parts with interfaces created from the stop and go process.

References

- [1] Context 3D Printing Analysis Service , "Powder Bed 3D Printing Solutions on the Rise Powder Bed Fusion for Metal and Plastics set for highest growth potential amongst seven main," 8 September 2016. [Online]. Available: https://www.contextworld.com/documents/20182/367799/CONTEXTQ2_16+Powder+Bed+Fusion+on+the+rise+Sept2016.pdf/4a7ab03c-c80f-451b-8352-8ca89da2b5bf. [Accessed 30 January 2017].
- [2] I. J. Petrick and T. W. Simpson, "3D Printing Disrupts Manufacturing: How Economies of One Create New Rules of Competition," *Research-Technology Management*, vol. 56, p. 12*16, 2015.
- [3] T. Wohlers, "Wohlers Report 2016: 3D Printing and Additive Manufacturing State of the Industry Annual Worldwide Progress Report," Wohlers Associates, Fort Collins, 2016.
- [4] United States International Trade Commission , "dditive Manufacturing Technology: Potential Implications for U.S. Manufacturing Competitiveness," *Journal of International Commerce and Economics* , pp. 1-35, September 2014.
- [5] N. Guo and M. C. Leu, "Additive Manufacturing: technology, applications and research needs," *Front. Mech. Eng.*, pp. 215-243, 2013.
- [6] I. Gibson, D. Rosen and B. Stucker, Additive Manufacturing Technologies: 3D Printing, Rapid Prototyping, and Direct Digital Manufacturing, 2nd ed., New York: Springer-Verlag, 2015, pp. 43-61.
- [7] ASTM International, "Standard Terminology for Additive Manufacturing- Coordinate System and Test Methodologies," ASTM International, West Coshohocken, 2014.
- [8] V. Petrovic, J. V. H. Gonzalez, O. J. Ferrando, J. Delgado Gordillo, J. R. Blasco Puchades and L. Portoles Grinan, "Additive layered manufacturing: sectors of industrial application

- shown through case studies," *International Journal of Production Research*, vol. 49, pp. 1061-1079, 2011.
- [9] W. E. Frazier, "Metal Additive Manufacturing: A Review," *Journal of Materials Engineering and Performance*, vol. 23, pp. 1917-1928, 8 April 2014.
 - [10] P. Edwards and M. Ramulu, "Fatigue performance evaluation of selective laser melted Ti-6Al-4V," *Materials Science & Engineering*, vol. 598, pp. 327-337, 2014.
 - [11] R. Kennedy, "GE Plans to Invest \$1.4B to Acquire Additive Manufacturing Companies Arcam and SLM; Accelerates Efforts in Important Digital Industrial Space," 6 September 2016. [Online]. Available: http://www.geaviation.com/press/other/other_20160906.html. [Accessed 9 December 2016].
 - [12] S. J. Grunewald, "GE is Using 3D Printing and Their New Smart Factory to Revolutionize Large-Scale Manufacturing," 4 April 2016. [Online]. Available: <https://3dprint.com/127906/ge-smart-factory/>. [Accessed 9 December 2016].
 - [13] L. Mullen, R. C. Stamp, W. K. Brooks, E. Jones and C. Sutcliffe, "Selective Laser Melting: A Regular Unit Cell Approach for the Manufacture of Porous, Titanium, Bone In-Growth Constructs, Suitable for Orthopedic Applications," *Journal of Biomedical Materials Research Part B: Applied Biomaterials*, pp. 325-334, 2008.
 - [14] L. E. Murr, S. M. Gaytan, E. Martinez, F. R. Medina and R. B. Wicker, "Fabricating Functional Ti-Alloy Biomedical Implants by Additive Manufacturing Using Electron Beam Melting," *Biotechnol Biomaterial*, vol. 2, no. 3, pp. 1-11, 2012.
 - [15] L. E. Murr, S. A. Quinones, S. M. Gaytan, M. I. Lopez, A. Rodela, E. Y. Martinez, D. H. Hernandez, E. Martinez, F. Medina and R. B. Wicker, "Microstructure and mechanical behavior of Ti-6Al-4V produced by rapid-layer manufacturing, for biomedical applications," *Journal of the Mechanical Behavior of Biomedical Materials*, vol. 2, no. 1, pp. 20-32, 2009.

- [16] O. L. Harrysson, O. Cansizonglu, D. J. Marcellin-Little, D. R. Cormier and H. A. West, "Direct metal fabrication of titanium implants with tailored materials and mechanical properties using electron beam melting technology," *Materials Science and Engineering: C*, vol. 28, no. 3, pp. 366-373, 2008.
- [17] Arcam AB, "Arcam EBM Users's Manual," Sweden, 2011.
- [18] L. E. Murr, E. Martinez, K. N. Amato, S. M. Gaytan, J. Hernandez, D. A. Ramirez, P. W. Shindo, F. Medina and R. B. Wicker, "Fabrication of Metal and Alloy Components by Additive Manufacturing: Examples of 3D Materials Science," *Journal of Materials Research and Technology*, vol. 1, no. 1, pp. 42-54, 2012.
- [19] A. Liu, C. K. Chua and k. F. Leong, "Properties of Test Coupons Fabricated by Selective Laser Melting," *Key Engineering Materials* , Vols. 447-448, pp. 780-784, 2010.
- [20] ASTM, ASTM Standard F2792-12a Standard Terminology for Additive Manufacturing Technologies, 2011.
- [21] S. Bremen, W. Meiners and A. Diatlov, "Selective Laser Melting a manufacturing technology for the future?," *Rapid Manufacturing* , pp. 33-38, 2012.
- [22] K. N. Amato, S. M. Gaytan , L. E. Murr, E. Martinez, P. W. Shindo, J. Herandez, S. Collins and F. Medina, "Microstrectures and mechanical behavior of Inconel 718 fabricated by selective laser melting," *Acta Materiallia*, pp. 2229-2239, 2012.
- [23] J. A. Gonzalez, J. Mireles , Y. Lin and R. B. Wicker , "Characterization of ceramic components fabricated suing binder jetting additive manufacturing technolgy," *Ceramics International* , pp. 10559-10564, 2016.
- [24] S. M. Gaytan, M. A. Cadena, H. Karim, D. Delfin, Y. Lin, D. Espalin, E. MacDonald and R. B. Wicker, "Fabrication of barium titanate by binder jetting additive manufacturing technology," *Ceramics International*, vol. 41, pp. 6610-6619, 2015.

- [25] F. C. Campbell, Elements of Metallurgy and Engineering Alloys, Materials Park, OH: ASM International, 2008.
- [26] J. P. Costes, Y. Guilet, G. Poulachon and M. Dessoly, "Tool-life and wear mechanisms of CBN tools in machining of Inconel 718," *International Journal of Machine Tools and Manufacture*, vol. 47, no. 7-8, pp. 1081-1087, 2007.
- [27] D. Buchbinder, H. Schleifenbaum, S. Heidrich, W. Meiners and J. Bültmann, "High Power Selective Laser Melting (HP SLM) of Aluminum Parts," *Physics Procedia*, vol. 12, pp. 271-278, 2011.
- [28] A. Thomas, M. El-Wahabi, J. M. Cabrera and J. M. Prado, "High temperature deformation of Inconel 718," *Journal of Materials Processing Technology*, pp. 469-472, 2006.
- [29] M. Rahman, W. K. H. Seah and T. T. Teo, "The Machinability of Inconel 718," *Journal of Materials Processing Technology*, pp. 199-204, 1997.
- [30] Special Metals Corporation, "INCONEL Alloy 625," A PCC Company, New Hartford, 2013.
- [31] S. K. Rai, A. Kumar, V. Shankar, T. Jayakumar, K. B. S. Rao and B. Raj, "Characterization of microstructures in Inconel 625 using," *Acta Materialia*, no. 51, pp. 59-63, 2004.
- [32] S. Floreen, G. E. Fuchs and W. J. Yang, "The Metallurgy of Alloy 625," *Superalloys 718, 625, 706 and Various Derivatives*, pp. 13-37, 1994.
- [33] H. X. Hu, Y. Zheng and C. P. Qin, "Comparison of Inconel 625 and Inconel 600 in resistance to cavitation erosion and jet impingement erosion," *Nuclear Engineering and Design*, vol. 240, pp. 2721-2730, 201.
- [34] K. H. Song and K. Nakata, "Effect of precipitation on post-heat-treated Inconel 625 alloy after friction stir welding," *Materials and Design*, vol. 31, pp. 2942-2947, 2010.

- [35] M. Baumers, C. Tuck, R. Hague, I. Ashcroft and R. Wildman, "A Comparative Study of Metallic Additive Manufacturing Power Consumption," in *Solid Freeform Symposium*, 2010.
- [36] M. Baumers , M. Holweg and J. Rowley, "The economics of 3D Printing: A total cost perspective," D2W, 2015.
- [37] R. Tacina, C. Wey, P. Laing and A. Mansour, "A Low NOx Lean-direct Injection, Multipoint Intergrated Module Combustor Concept for Advanced Aircraft Gas Turbines," in *NASA Technical Memorandum NoNASA/TM-2002-211347*, 2002.
- [38] W. R. Fahrner, R. Job and M. Werner, "Sensors and smart electronics in harsh environments applications," *Microsystem Technologies* , pp. 138-144, 2001.
- [39] A. Arnau Vives, *Piezoelecric Transducers and Applications*, Springer Berlin Heidelberg, 2008.
- [40] J. G. Webster, *The Measurement, Instrumentation, and Sensors: Handbook*, Springer Science & Business Media, 1999.
- [41] X. C. Li, F. Prinz and J. Seim, "Thermal Behavior of Metal Embedded Fiber Bragg Grating Sensor," *Smart Materials and Structures*, vol. 10, no. 4, pp. 575-579, 2001.
- [42] E. Aguilera, J. Ramos, D. Espalin, F. Cedillos, D. Muse , R. Wicker and E. Macdonald, "3D Printing of Electro Mechanical Systems," in *24th International SFF Symposium - An Additive Manufacturing Conference, SFF 2013*, Austin, 2013.
- [43] C. A. Terrazas, S. M. Gaytan, E. Rodriguez, D. Espalin, L. E. Murr , F. Medina and R. B. Wicker, "Multi-material Metallic Structure Fabrication Using Electron Beam Melting," *The Internatioal Journal of Advanced Manufacturing Technology*, vol. 71, no. 1-4, pp. 33-45, 2013.

- [44] S. L. N. Ford , "Additive Manufacturing Technology: Potential Implications for U.S. Manufacturing Competitiveness," *Journal of International Commerce and Economics*, pp. 1-35, 2014.
- [45] ASTM International, *ASTM 30546-14 Standard Specification for Additive Manufacturing Nickel Alloy*, West Conshohocken, PA: ASTM International , 2014.
- [46] Kittyhawk Products , "Kittyhawk Products," 2 April 2017. [Online]. Available: <https://kittyhawkinc.com/materials-to-be-hiped/>. [Accessed 2 April 2017].
- [47] S. Ozbilen, "Satellite formation mechanism in gas atomised powders," *Powder Metallurgy*, vol. 1, no. 42, pp. 70-78, 1999.
- [48] ASTM International, "Standard Test Methods for Flow Rate of Metal Powders Using the Hall Flowmeter Funnel," ASTM International, Conshohocken, PA, 2014.
- [49] A. B. Spierings, M. Voegtlin, T. Bauer and K. Wegener, "Powder flowability characterisation methodology for powder-bed-based metal additive manufacturing," *Progress in Additive Manufacturing*, vol. 1, no. 1-2, pp. 9-20, 2016.
- [50] ASTM International , "Standard Test Method for Density of Powder Metallurgy (PM) Materials Containing Less Than Two Percent Porosity," ASTM International , West Conshohocken, 2013.
- [51] L. E. Murr, "Metallurgy of additive manufacturing: Example from electron beam melting," *Additive Manufacturing* , vol. 5, pp. 40-53, 2015.
- [52] S. S. Al-Bermani, M. L. Blackmore, W. Zhang and I. Todd, "The Origin of Microstructural Diversity, Texture, and Mechanical Properties in Electron Beam Melted Ti-6Al-4V," *Metallurgical and Materials Transactions A*, vol. 41, no. 13, pp. 3422-3434, 2010.
- [53] S. M. Yahya, Turbines, compressors, and fans, New Delhi: McGraw-Hill Education, 2011.
- [54] P. Kanagarajah, F. Brenne, T. Niendorf and H. J. Maier , "Inconel 939 processed by selective laser melting: Effect of microstructure and temperature on the mechanical

- properties under static and cyclic loading," *Materials Science & Engineering*, vol. 58, pp. 188-195, 2013.
- [55] F. Liu, X. Lin, C. Huang, M. Song, G. Yang, J. Chen and W. Huang, "The effect of laser scanning path on microstructures and mechanical properties of laser solid formed nickel-base superalloy Inconel 718," *Journal of Alloys and Compounds*, vol. 509, pp. 4505-4509, 2011.
- [56] E. O. Olakanmi, "Selective laser sintering/melting (SLS/SLM) of pure Al, Al–Mg, and Al–Si powders: Effect of processing conditions and powder properties," *Journal of Materials Processing Technology*, vol. 213, pp. 1387-1405, 2013.
- [57] F. Tehovnik, J. Burja, B. Podgornik, M. Godec and F. Vode, "Microstructural Evolution of INCONEL 625 During Hot Rolling," *Materials and technology*, vol. 49, no. 5, pp. 801-806, 2015.
- [58] D. Li, Q. Guo, S. Guo, H. Peng and Z. Wu, "The microstructure evolution and nucleation mechanisms of dynamic recrystallization in hot-deformed Inconel 625 superalloy," *Materials and Design*, vol. 32, pp. 696-705, 2011.
- [59] W. D. Callister Jr., *Materials Science and Engineering an Introduction*, York , PA: John Wiley & Son, Inc., 2007.
- [60] D. C. Montgomery and G. C. Runger, *Applied Statistics and Probability for Engineering*, Upper Saddle River , NJ: Pearson Prentice Hall, 2004.
- [61] D. A. Wigley, *Mechanical Properties of Materials at Low Temperature*, New York : Plenum Press , 1971.
- [62] R. W. Hertzberg, *Deformation and Fracture Mechanics of Engineering Materials*, John Wiley & Sons, 1989.
- [63] A. Blake , *Handbook of Mechanics, Materials, and Structures*, Livermore, CA: Wiley-Interscience, 1985.

- [64] T. L. A. Ted L. Anderson, *Fracture Mechanics: Fundamentals and Applications*, Third Edition, Boca Raton: CRC Press Taylor & Francis Group , 2005.
- [65] T. Tunberg and L. Nyborg, "Surface Reactions During Water Atomisation and Sintering of Austenitic Stainless Steel Powder," *Powder Metallurgy*, vol. 38, no. 2, pp. 120-130, 1995.
- [66] O. Bergman, "Key Aspects of Sintering Powder Metallurgy Steel," Chalmers University of Technology , Gothenburg, Sweden, 2011.
- [67] W. J. Mills, "The deformation and fracture characteristics of inconel X-750 at room temperature and elevated temperatures," *Metallurgical Transactions A*, vol. 11, no. 6, pp. 1039-1047, 1980.
- [68] M. S. Hossian, J. A. Gonzalez, R. Martinez Hernandez, M. A. I. Shuvo , J. Mireles , A. Choudhur , Y. Lin and R. B. Wicker , "Fabrication of smart parts using powder bed fusion additive manufacturing technology," *Additive Manufacturing* , no. 10, pp. 58-66, 2016.
- [69] R. Pederson, *Microstructure and Phase Transformation of Ti-6Al-4V*, Lucea University of Technology , 2002.
- [70] ExOne Digital Part Materialization, "ExOne Industries & Applications," 2016. [Online]. Available: <http://www.exone.com/Industries-Applications>. [Accessed December 2016].
- [71] N. Guo and M. C. Leu, "Additive manufacturing: technologies, applications and research needs," *Front. Mech. Eng.*, vol. 8, no. 3, pp. 215-243, 2013.
- [72] H. L. Eiselstein and D. J. Tillack, "The invention and Definition of Alloy 625," The Minerals, Metals & Materials Society, Huntington, WV, 1991.

Appendix

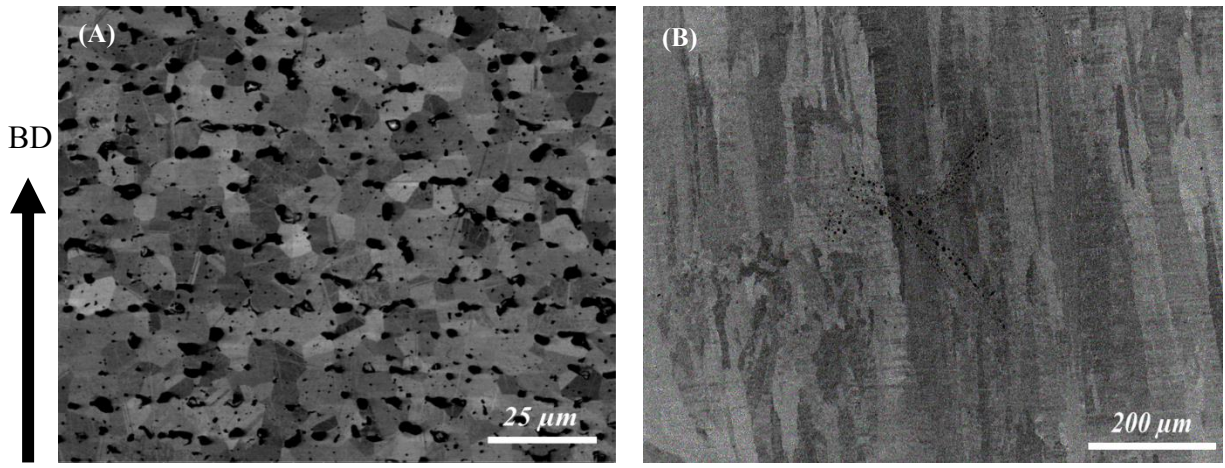


Figure A-1. SEM images revealing a contrast between the grains allowing a visible microstructure of (A) binder jetting and (B) EBM Inconel 625 fabricated samples.

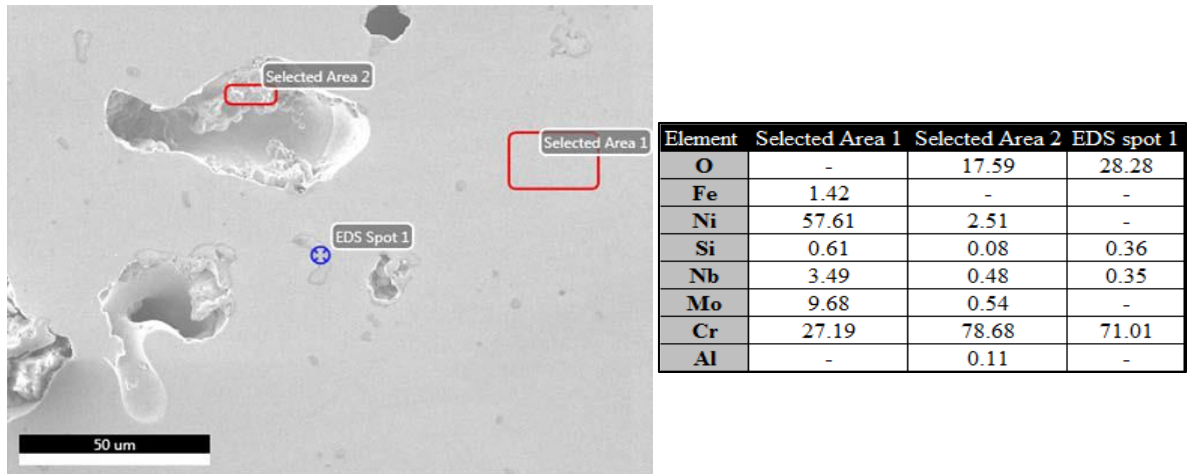


Figure A-2. Various EDS analysis of polished binder jetting fabricated samples. Pores appear to be entrapped Cr-O phase (Area 2). Small Cr-O phase areas remain in the sample (Spot 1).

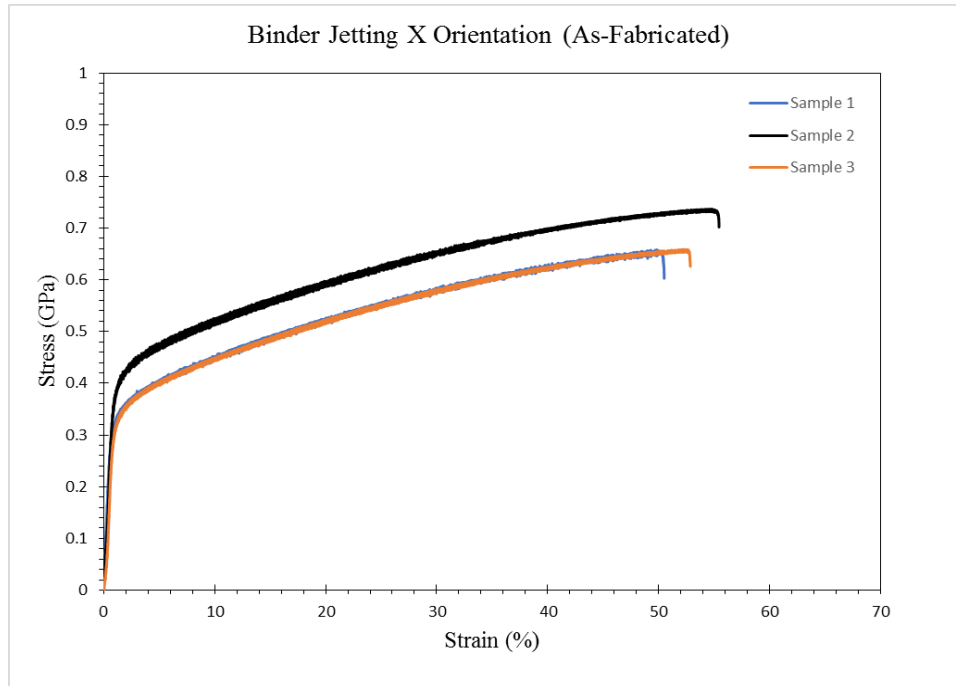


Figure A-3. Stress vs. strain (%) test curves results of As-fabricated binder jetting samples fabricated in the X orientation.

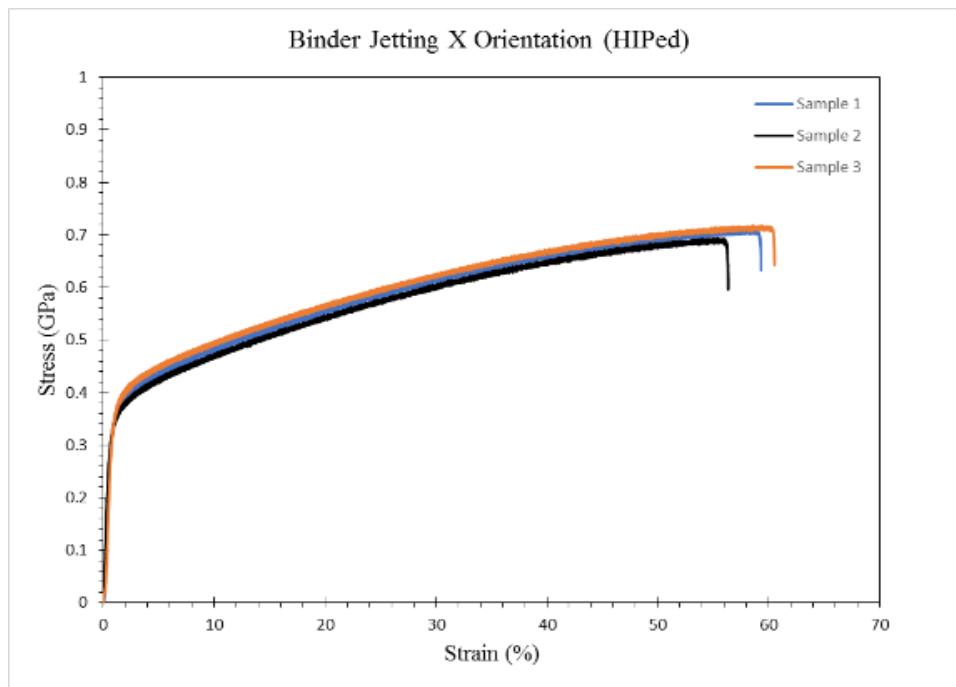


Figure A-4. Stress vs. strain (%) test curves results of HIPed binder jetting samples fabricated in the X orientation.

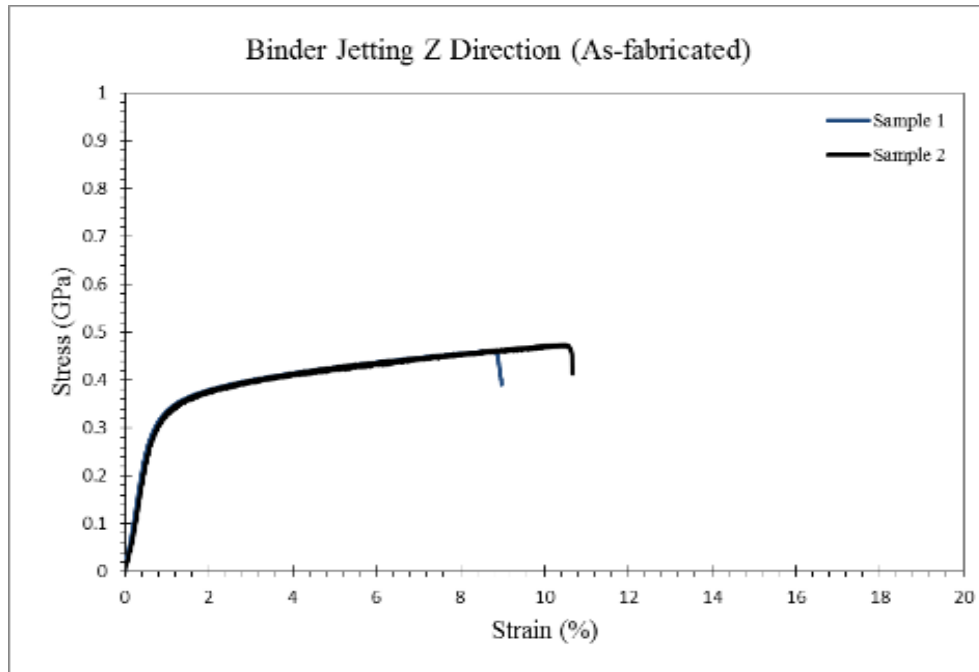


Figure A-5. Stress vs. strain (%) test curves results of as-fabricated binder jetting samples fabricated in the Z orientation.

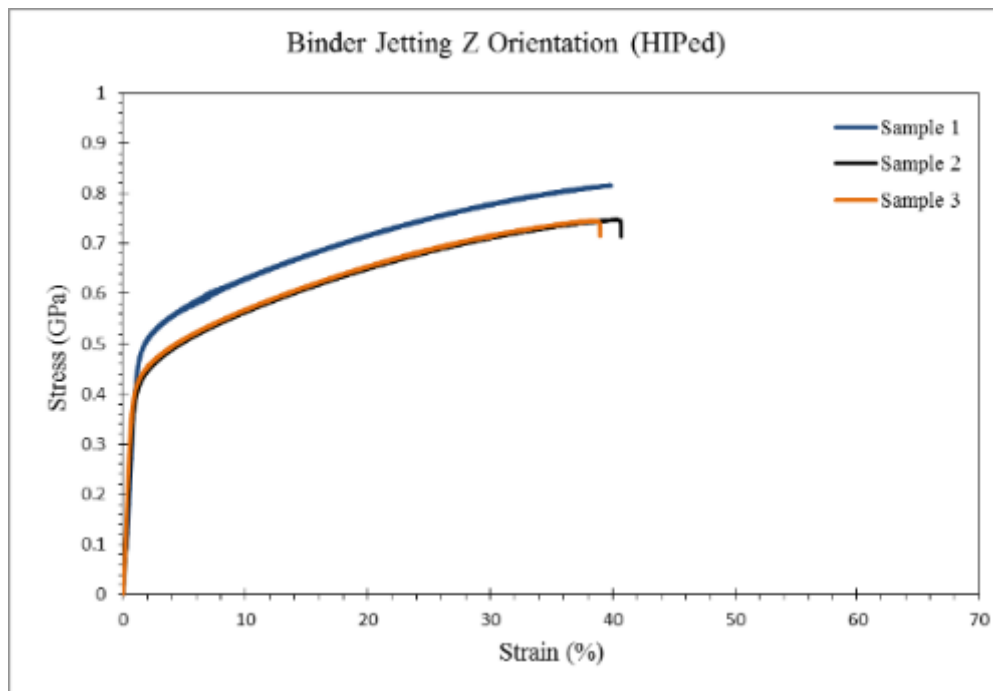


Figure A-6. Stress vs. strain (%) test curves results of HIPed binder jetting samples fabricated in the Z orientation.

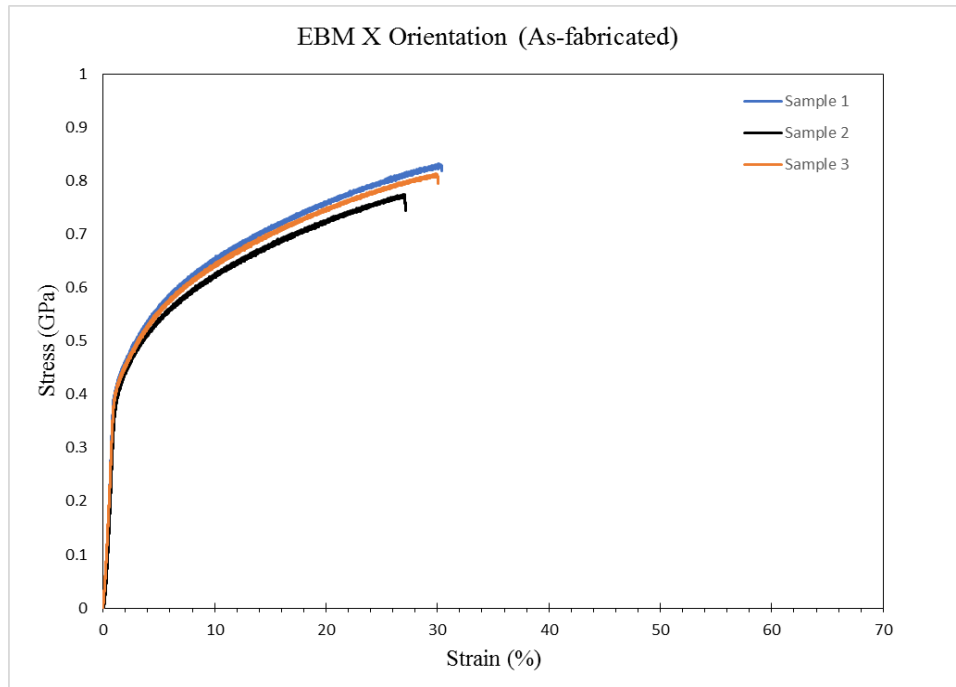


Figure A-7. Stress vs. strain (%) test curves results of as-fabricated EBM samples fabricated in the X orientation.

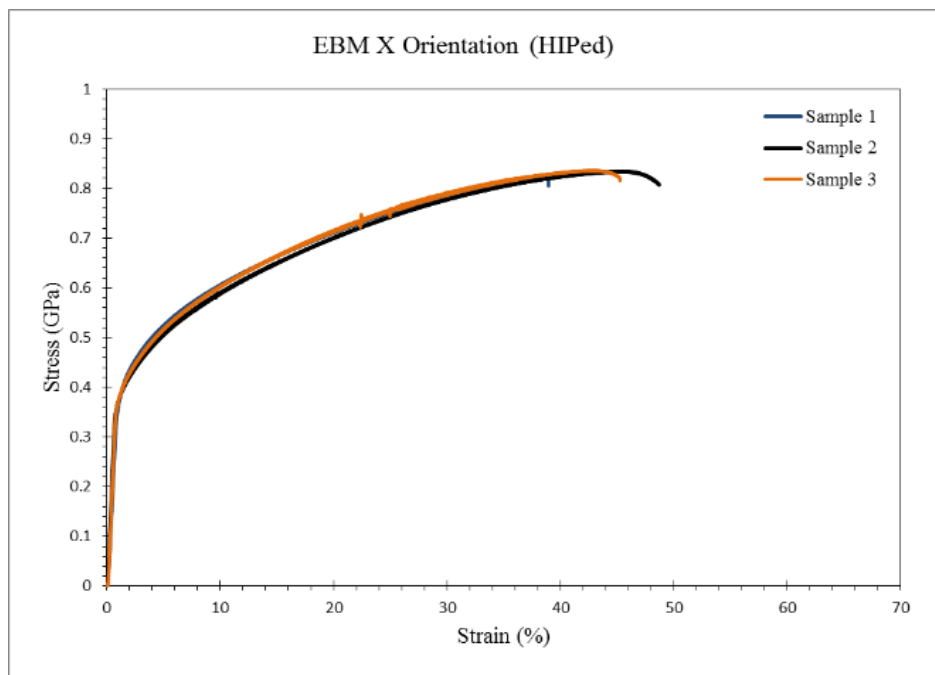


Figure A-8. Stress vs. strain (%) test curves results of HIPed EBM samples fabricated in the X orientation.

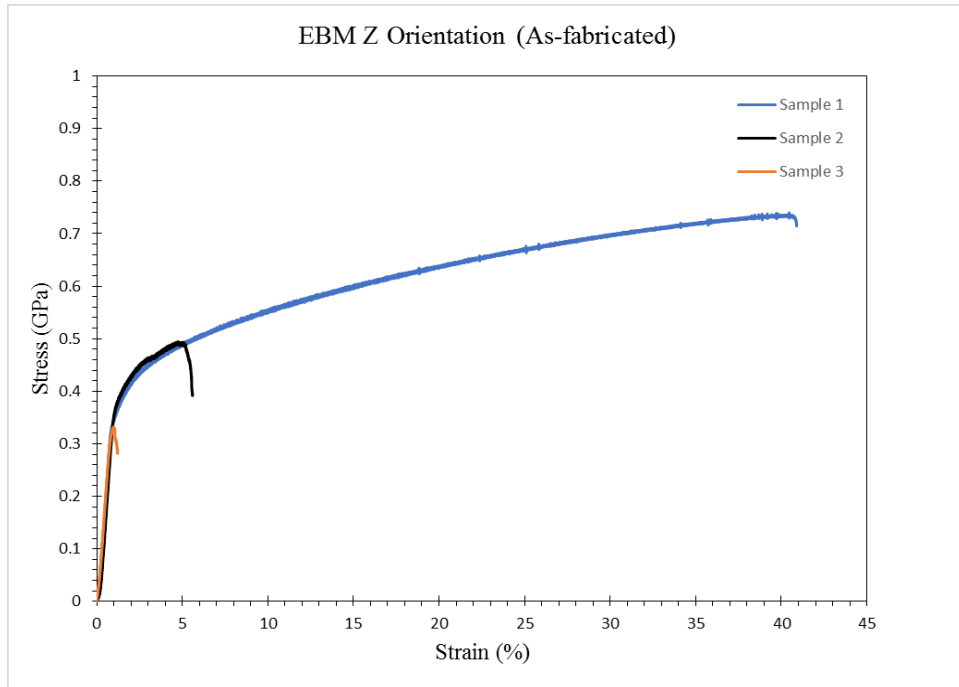


Figure A-9. Stress vs. strain (%) test curves results of as-fabricated EBM samples fabricated in the Z orientation.

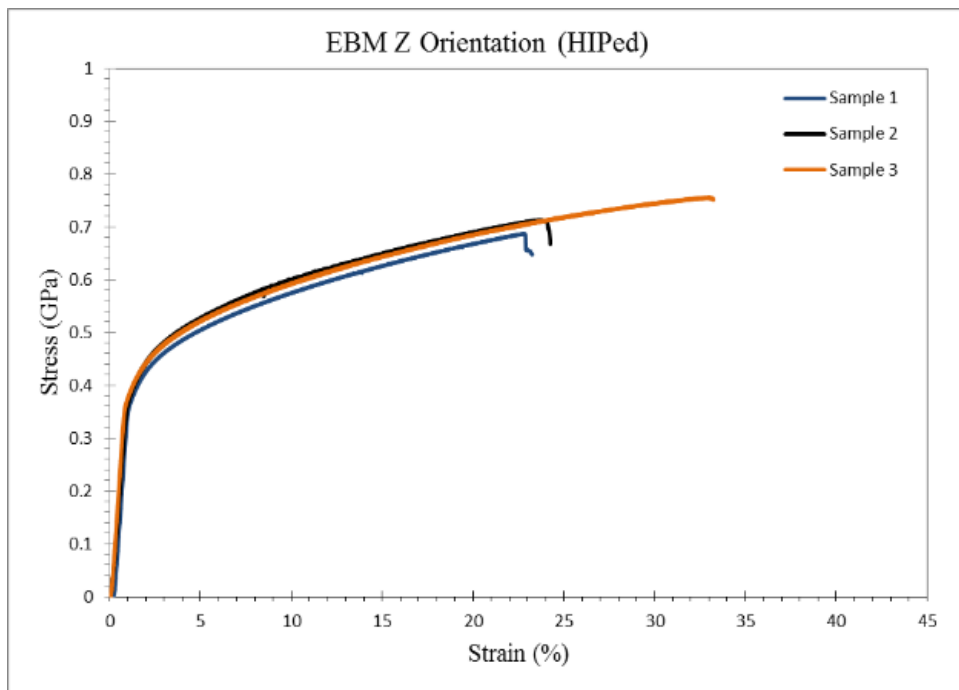


Figure A-10. Stress vs. strain (%) test curves results of HIPed EBM samples fabricated in the Z orientation.

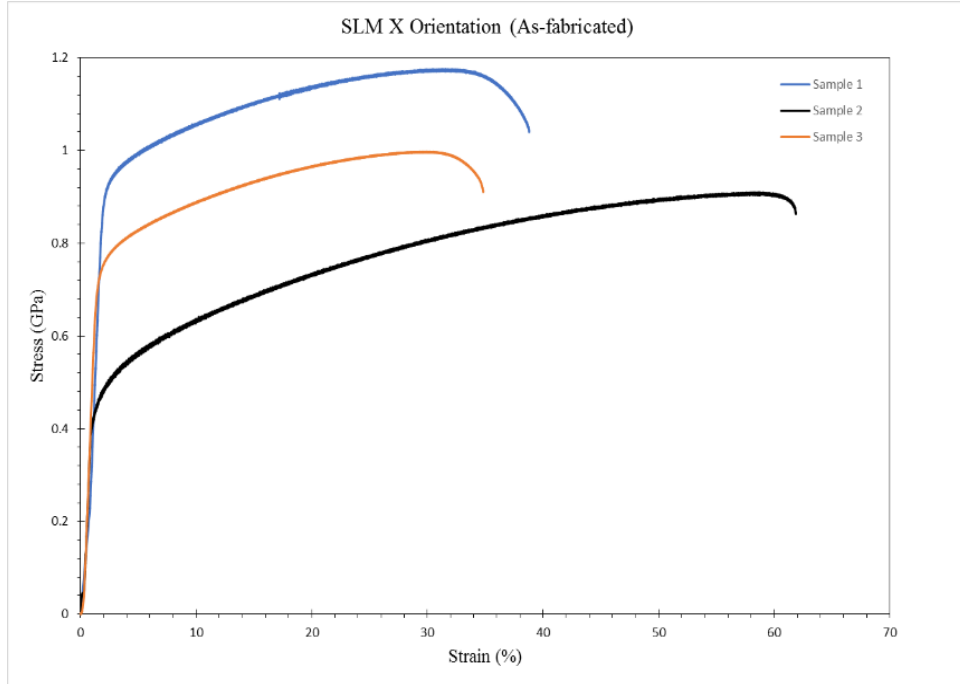


Figure A-11. Stress vs. strain (%) test curves results of as-fabricated SLM samples fabricated in the X orientation.

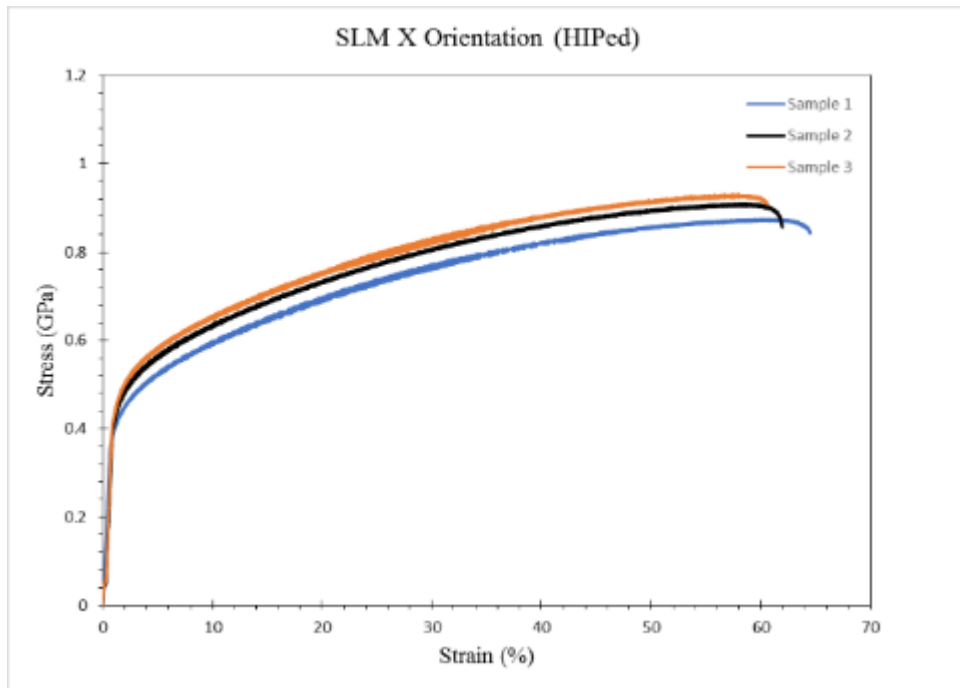


Figure A-12. Stress vs. strain (%) test curves results of HIPed SLM samples fabricated in the X orientation.

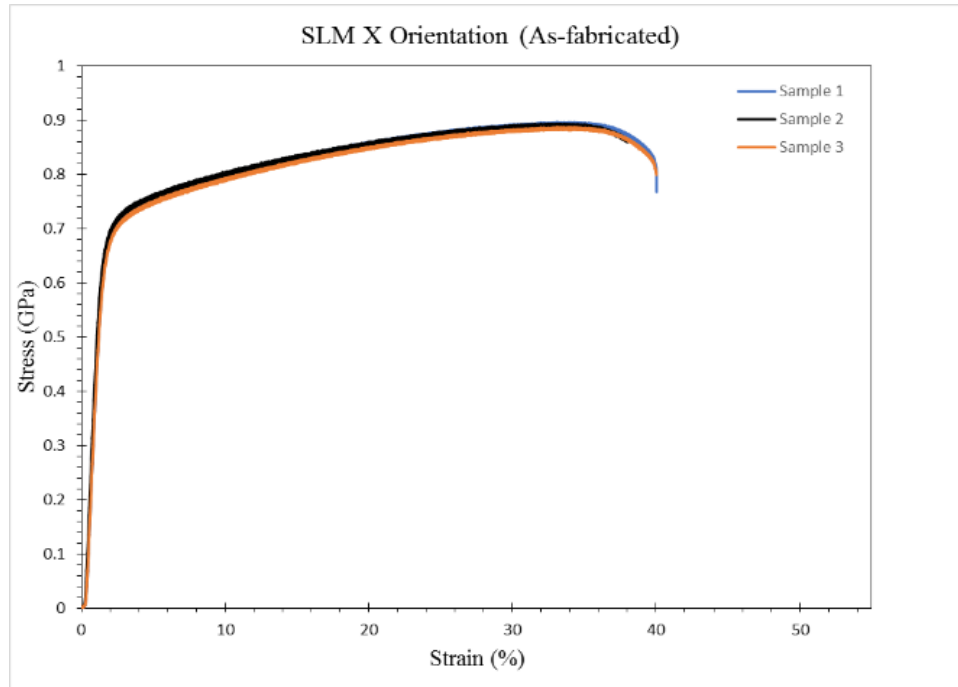


Figure A-13. Stress vs. strain (%) test curves results of as-fabricated SLM samples fabricated in the Z orientation.

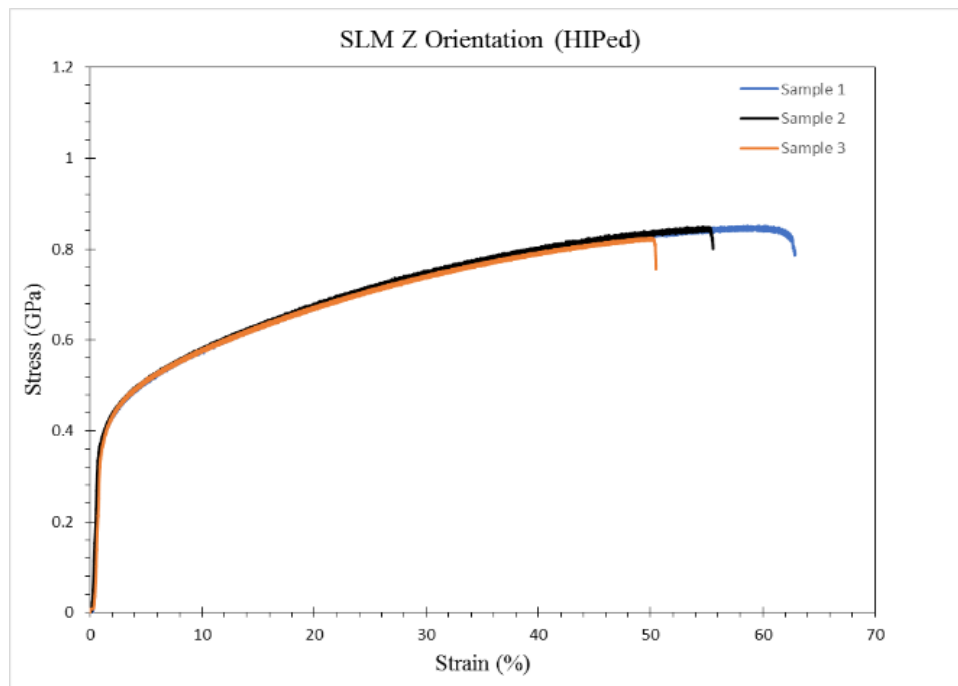


Figure A-14. Stress vs. strain (%) test curves results of HIPed SLM samples fabricated in the Z orientation.

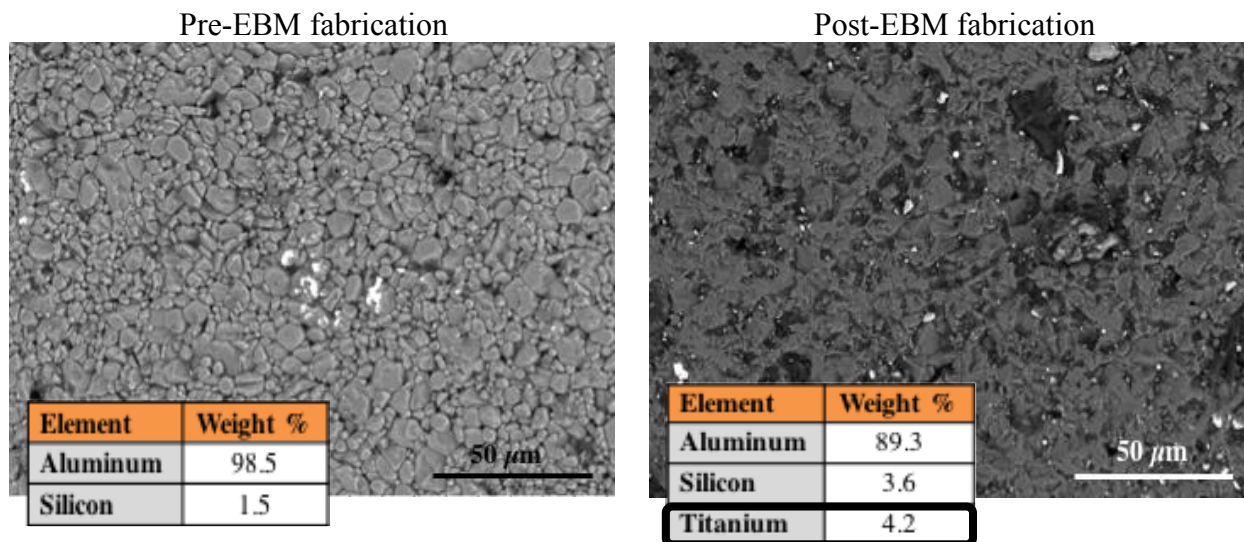


Figure A-9. SEM images and EDS analysis of both pre-and-post EBM PZTs, where newly identified titanium is now present on surface of the PZT.

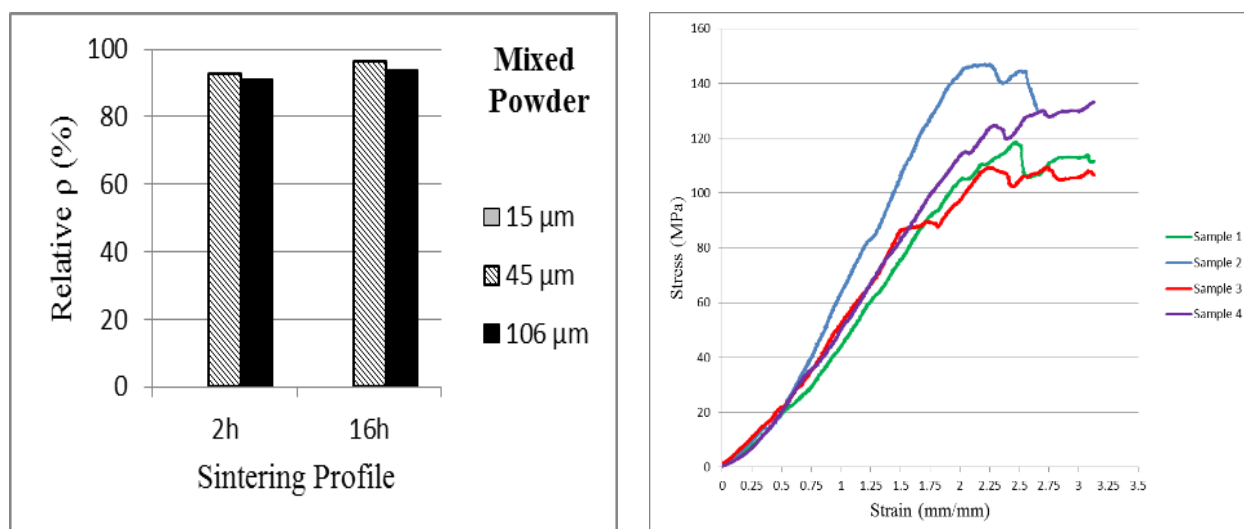


Figure A-9. Density measurements and compressive strength of alumina fabricated using binder jetting AM technology and sintered for 16hrs [23].

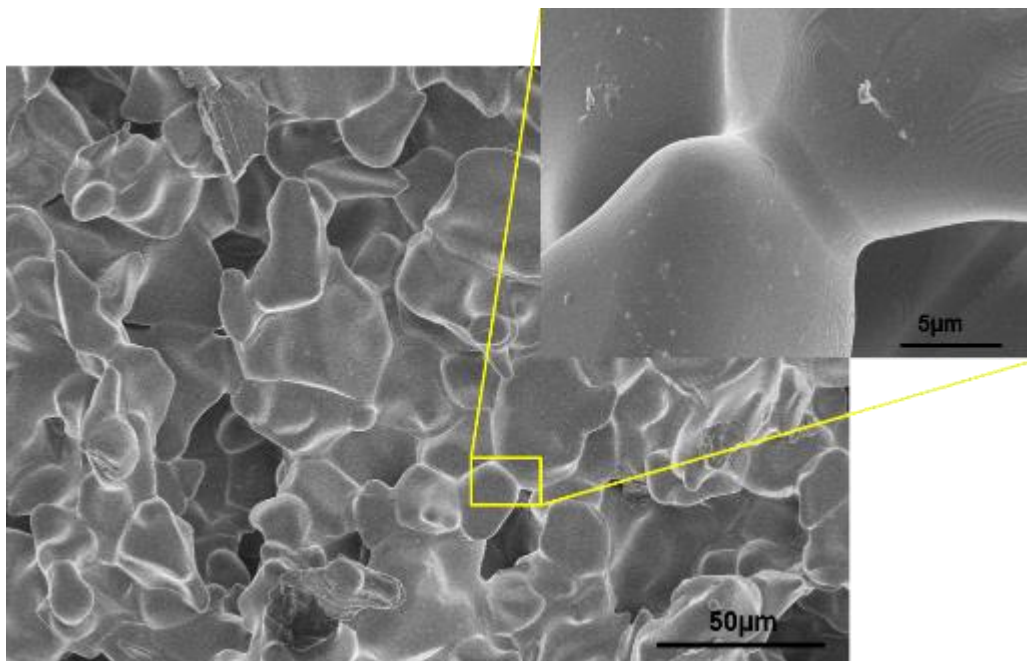


Figure A-10. SEM image of Alumina samples that has been sintered for a total of 16 hours. A higher-magnified image shows the formation of necks between two powder particles [23].

Curriculum Vita

Jose Angel Gonzalez was born on June 9, 1990, to Jose Angel Gonzalez and Luz Yolanda Loya. He attended Montwood High School participating in extracurricular activities such as the varsity football team as well as the national honor society. Jose completed his undergraduate studies from the University of Texas at El Paso (UTEP), earning a Bachelor of Science in Metallurgical and Materials Engineering in December 2012. As an undergraduate student, Jose participated on a various internships, including with the National Aeronautics and Space Administration (NASA), where he applied academic knowledge to projects connected to the International Space Station (ISS). In January 2014, Jose began his graduate studies to pursue a Ph.D. in Materials, Science, and Engineering. Jose joined the W.M. Keck for 3D Innovation (Keck Center) at UTEP soon after, beginning his experience with additive manufacturing technologies. During the time as a doctoral student, Jose become a Ph. D. research associate where he focused his research on the characterization of materials (metallic and ceramic) fabricated by powder bed-based AM technologies (binder jetting, EBM, and SLM). Research performed by Jose at the Keck Center has been presented in multiple academic conferences including the Solid Freeform Fabrication Symposium while also being published in the Ceramics International Journal and Additive Manufacturing Journal.

Jose worked on his dissertation topic: Characterization and Comparison of Metallic and Ceramic Parts Fabricated Using Powder Bed Based Additive Manufacturing Technologies, under the direction of Dr. Ryan B. Wicker and guidance of Dr. Yirong Lin.

Permanent address: 11680 Norman Montion Dr.

El Paso, TX, 79936

This dissertation was typed by Jose Angel Gonzalez.